EXPERIMENTAL AND NUMERICAL STUDIES ON MULTI-SCALED PROGRESSIVE AND COMPOUND FORMING OF BULK PARTS AND SIZE EFFECTS ON PROCESS PERFORMANCE AND PRODUCT QUALITY

ZHENG JUNYUAN

PhD

The Hong Kong Polytechnic University

2021

The Hong Kong Polytechnic University

Department of Mechanical Engineering

Experimental and Numerical Studies on Multi-Scaled Progressive and Compound Forming of Bulk Parts and Size Effects on Process Performance and Product Quality

Zheng Junyuan

A thesis submitted in partial fulfilment of

the requirements for the degree of

Doctor of Philosophy

July 2021

CERTIFICATE OF ORIGINALITY

I hereby declare that this thesis is my own work and that, to the best of my knowledge and belief, it reproduces no material previously published or written, nor material that has been accepted for the award of any other degree or diploma, except where due acknowledgment has been made in the text.

ZHENG Junyuan

Abstract

Progressive and compound meso/microforming by directly using sheet metals is a promising approach to realizing mass production of complex and meso-/micro-scaled bulk parts and structures with high productivity and material utilization. However, due to the size-related extrinsic and intrinsic parameters of materials and forming systems, the emergence of size effect induces different mechanical responses and deformation behaviors in differently size-scaled domains. Investigation of the size-dependent process performance and product quality from the aspects of forming load, material flow, dimensional accuracy, defects, surface quality, and fracture is necessary to promote the application of this technology. In this research, various progressive and compound forming systems for making different meso-/micro-scaled parts were developed and their forming processes and products were comprehensively explored through physical experiments and numerical simulations. The results revealed that the formation mechanism and characteristics of shear bands and dead metal zones are related to velocity gradient and strain accumulation. For the punching/blanking operation, the grain size effect results in the deviation of punch stroke and the variation of part dimensions. When the punch-die clearance equals the grain size, the maximum ultimate shear stress of blanking and the highest burr are obtained. The larger grain size and punch-die clearance increase the material loss and reduce the bulge diameter of the produced parts. Moreover, various surface defects including microcracks, micro pits, uneven surface, longitudinal surface texture, sunken area, and surface damage were found on different features.

To quantitively explore the size-dependent meso-/micro-scaled deformation behaviors in the progressive and compound meso/microforming, constitutive modeling considering grain orientations and the grain boundary-interior difference was

proposed. The orientations and anisotropies of the individual grains become a non-trivial issue in prediction of the mechanical responses and deformation behaviors of the down-scaling materials. Meanwhile, the grain boundary is generally considered to be isotropic and to impede deformation. The feasibility of this modeling was verified through experiments and simulations with different specimens and grain sizes, and geometrical and grain size effects on the flow stress were reflected. The modeling combining GTN criterion revealed that cracks initiate and elongate near grain boundaries. More and slighter cracks appear with the fine-grained material while coarser grains promote larger and serious cracks on the heading-formed parts. Compared with crystal plasticity finite element (CPFE) model in meso-compression tests, the modeling loses a bit of accuracy in flow stress and free-surface formation but has advantages of efficiency. The modeling can also predict a zig-zag distribution of shear bands and similar geometries as the compressed specimens with different grain sizes. This modeling thus considers both precision and efficiency in meso-/micro-scaled deformation and forming problems of polycrystalline metallic materials.

In addition, the quality of defect-free parts and the efficiency of processes are crucial in metal forming, and size effects induce many unknown deformation behaviors in product miniaturization. In this research, a numerical design-based method associated with different tooling designs and processes was employed to investigate the size-dependent mechanism of folding defects and their avoidance to improve material flow. Four designs were proposed with different forming sequences of the part features, and the best of them was selected by the analysis of material flow during each forming process and the comparison of energy consumption, folding avoidance, and geometrical accuracy among different designs. The experiments and morphological observations were conducted with three size scales and the results were consistent with the simulations. It was found that the macro-scaled folding defect was serious and regular but the meso-/micro-scaled one was slight and irregular.

Publications arising from this research

International journal papers

[1] **Zheng, J.Y.**, Yang, H.P., Fu, M.W., et al. (2019). Study on size effect affected progressive microforming of conical flanged parts directly using sheet metals. ***Journal of Materials Processing Technology***, 272, 72-86.

[2] **Zheng, J.Y.**, Shi, S.Q., Fu, M.W. (2020). Progressive microforming of pin-shaped plunger parts and the grain size effect on its forming quality. ***Materials & Design***, 187, 108386.

[3] **Zheng, J.Y.**, Wang, J.L., Fu, M.W. (2021). Experimental and numerical study of the size effect on compound Meso/Microforming behaviors and performances for making bulk parts by directly using sheet metals. ***Journal of Manufacturing Processes***, 66, 506-520.

[4] **Zheng, J.Y.**, Fu, M.W. (2020). Progressive and compound forming for producing plunger-typed microparts by using sheet metal. ***Journal of Micro and Nano-Manufacturing***, 8(2).

Papers to be submitted

[5] **Zheng, J.Y.**, Ran, J.Q., Fu, M.W., Constitutive modeling of meso-/micro-scaled deformation of polycrystalline metallic materials considering grain inhomogeneous distribution and the properties of grain boundaries, ***to be submitted to International Journal of Plasticity.***

[6] **Zheng, J.Y.**, Fang, J.Y.C., Fu, M.W., Numerical and experimental studies of prediction and simulation-based avoidance of folding defects in multi-scaled bulk metal forming of flanged parts, ***to be submitted to The International Journal of Advanced Manufacturing Technology.***

Book chapters

[7] **<u>Zheng, J.Y.</u>**, Fu, M.W., Zeng, F. (2021). Design and Development of Multi-scaled Metallic Parts and Structures, ***Encyclopedia of Materials: Metals and Alloys, Elsevier***.

[8] Fu, M.W., **<u>Zheng, J.Y.</u>** (2020). Progressive and Compound Forming of Metallic Sheets for Making Micro-/Meso-Scaled Parts and Components, ***Encyclopedia of Materials: Metals and Alloys, Elsevier***.

[9] Fu, M.W., **<u>Zheng, J.Y.</u>** (2021). Die casting of metallic parts and structures, ***Encyclopedia of Materials: Metals and Alloys, Elsevier***.

Conference proceedings

[10] **<u>Zheng, J.Y.</u>**, Fu, M.W., (2021). Study of Micro-Upsetting by Finite Element Simulation Based on Crystal Plasticity and Grain Boundary Strengthening Theories, ***12th International Conference on Materials and Manufacturing Technology***

Acknowledgments

Upon completing this thesis, I am very grateful to those who have offered encouragement and support during my three-year Ph.D. study in the Department of Mechanical Engineering, The Hong Kong Polytechnic University.

I would first like to extend my sincere gratitude to my respectable supervisor, Professor Mingwang Fu, who has given me invaluable guidance and suggestions regarding my research and cheerful encouragement and endless patience. He was always able to point out the key problems in my research methods and manuscript writing. With his exceptional insight and abundant knowledge, this thesis was improved significantly.

Second, I would like to thank The Hong Kong Polytechnic University, which provides scholarship to me for my Ph.D. study and the world-class education and experimental platform for my research. I would also like to thank the staff and technicians in the Department of Mechanical Engineering for the facility and support of my daily affairs and experiments.

Third, I would like to sincerely thank my research group members, Dr. Yang Haopeng, Dr. Li Wenting, Dr. Tang Xuefeng, Dr. Wang Jin, Dr. Cai Zhengyang, Dr. Tian Wenlong, Dr. Ma Jun, Miss. Fang Jieyichen, Mr. Fu Jin, Mr. Zhang Rui, Mr. Tong Xu, Mr. Liu Hui, and Mr. Hu Dien, who have selflessly assisted me and have encouraged me with their positive attitudes.

Last but not least, I would like to express my heartfelt gratitude to my parents, Mr. Zheng Mingxu and Mrs. Wang Hong for their great and unselfish love. This dissertation is dedicated to my family.

Table of Contents

List of abbreviations and acronyms

Abbreviations	Explanations
MEMS	Micro-electromechanical system
EDM	Electrical-discharge-machining
AM	Additive manufacturing
FDM	Fused deposition modeling
SLS	Selective laser sintering
SLM	Selective laser melting
LOM	Laminated object manufacturing
RCA	Real contact area
CLP	Closed lubricant pocket
OLP	Open lubricant pocket
SF	Scaling factor
CRSS	Critical resolved shear stress
FEM	Finite elements method
CPFEM	Crystal plasticity finite elements method
GI	Grain interior
GB	Grain boundary
PK2	Second Piola-Kirchhoff
GTN	Gurson-Tvergaard-Needleman
PCB	Printed circuit board
DMZ	Dead metal zone
RVE	Representative volume elements

Chapter 1 Introduction

1.1 Research background

As the tendency toward product miniaturization increases in microelectronics, automotive, biomedicine, and many other industrial clusters, meso/micro-scaled parts and structures are going to be the spotlight [1, 2]. To meet this increasing demand, meso-/micro-manufacturing technologies have emerged and developed over several decades, including meso-/micro-machining [3, 4], laser beam machining [5, 6], meso-/micro-injection molding [7, 8], meso-/micro-mechanical assembly [9], meso/microforming [10, 11], and so on. Some meso-/micro-scaled parts fabricated using meso-/micro-manufacturing are shown in **Fig. 1.1**. Among theses technologies, meso/microforming is a promising method for mass-producing meso/microparts productively with less material waste, net-shape or near-net-shape characteristics, high quality, and advanced mechanical performance [10]. Microforming is defined as the fabrication of metallic microparts or structures for microsystems or microelectromechanical systems (MEMS) with at least two dimensions under 1 mm based on metallic plastic deformation [1], while mesoforming refers to the same types of parts and structures with dimensions ranging from 1 mm to 10 mm. Meso/microforming processes have some inherent disadvantages, such as the difficulty of operating billets and preforms among different operations and ejecting final parts out of die cavity, deviations in dimensional accuracy, and undesirable geometries. So-called progressive and compound meso/microforming has been developed to address problems in the handling, transportation, and ejection of billets, preforms, and final parts of the forming process and to facilitate the application of meso/microforming in mass production [12, 13]. Progressive forming, which is comprised of several forming operations with a given sequence, directly employs sheet metals to fabricate bulk parts using progressive microtools in such a way that one or more specific features of parts to be made are formed in each progressive forming operation, whereupon complex parts with various miniaturized features are eventually produced. The primary advantages of this process include the precise alignment of tooling and workpieces, the easy transport of preforms to the next operation, and the efficient ejection of final parts by blanking operations [14, 15]. Compound forming, however, combines several types of material deformation in one operation, which contrasts with the one deformation in conventional forming. For example, compound forming can simultaneously realize blanking and extrusion [16, 17]. Progressive and compound forming are efficient approaches for solving technical problems emerging in meso/microforming, but the processes of these technologies and their product quality have not been well investigated.

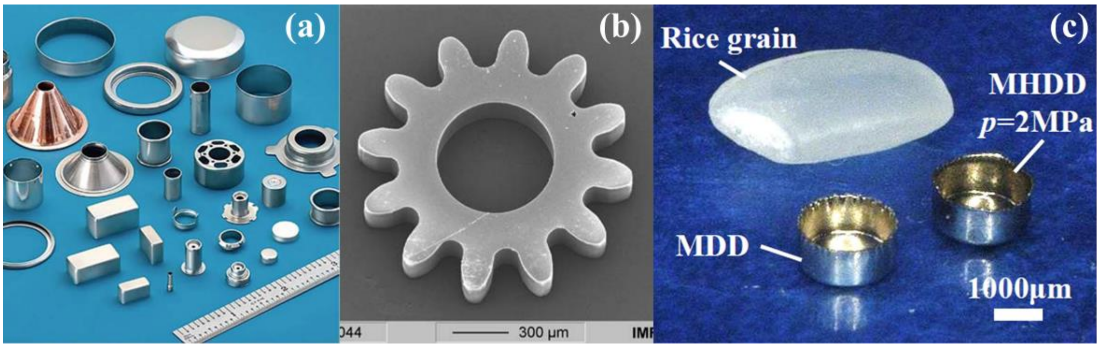

Fig. 1.1 (a) Miniature components produced through microforming [18]. (b) A polymer microgear made by rapid prototyping process [19]. (c) Cups made using titanium foils by micro deep drawing (MDD) and micro hydro deep drawing (MHDD) [20].

In downscaled meso/microforming processes, macroforming knowledge cannot be applied directly due to size effects [21, 22], viz., geometrical, microstructural grain, and tribological size effects. Previous studies of grain size effect on micro-extrusion revealed that the coarse-grained material induces inhomogeneous shape [23], lower hardness and strength [24], and increased friction factor [25]. If meso/microforming processes are to be widely applied in mass production, the size effect induced issues are crucial, such as deformation behaviors in microforming and progressive microforming processes and the surface fractures, undesirable geometries, and dimensional accuracy of microparts [12-15, 17, 26-32].

Prior research has tried to establish constitutive models for quantitatively describing the mechanical deformation behaviors at the meso/microscale. Some empirical stress-strain equations were established to represent the flow stress of experimental results, such as the Ludwik power law [33], the Swift power law [34], the Voce equation [35], and the Ramberg-Osgood equation [36]. However, these empirical models do not reflect size effects. The most well-known empirical model is the Hall-Petch equation, which represents the grain-size-dependent mechanical strength properties [37-39]. Moreover, the surface layer model [40] and the composite model [41] describe size effects of the mechanical strength properties that different portions of a material contribute. One theoretical model that represents the anisotropy of grains, including the orientation, distribution, and shape of grains, is the crystal plasticity theory [42]. The crystal plasticity finite elements method (CPFEM) [43] is one of the popular numerical methods for analyzing the micro-scaled deformation behaviors of crystal based on the slip of lattice that considers the texture and distribution of individual grains. The method’s feasibility and precision to predict the inhomogeneous properties of material have been verified. However, the above theoretical models and empirical equations have their limits, which are discussed in Section 2.5. Thus, developing a comprehensive multi-scaled model for solving engineering problems is still necessary.

Aside from the irregular deformation behaviors affected by size effects, forming defects are common in bulk forming processes and include cracks, surface defects, form defects, shear defects, structural defects, and folding due to severe plastic deformation, the complex material flows of the forming process, and imperfect tooling [44]. Since bulk-formed metallic parts generally require high dimensional precision and defect-free surfaces in order to be assembled with other components directly, the formation and avoidance of flow-induced forming defects related to size effects must be understood.

1.2 Research objectives and scope

In meso-/micro-scaled deformation processes, size-related parameters can greatly affect deformation behaviors, which are different from macro-scaled deformation processes. The objectives of this research are presented as follows:

1) Develop progressive and compound meso/microforming systems with integrated design and analysis methodologies of different products and deeply investigate the deformation behaviors of processes and the quality of final parts related to size effects and the mechanisms of the phenomena.

2) Establish a constitutive model for solving engineering problems that describes the material deformation behaviors in meso/microforming, reflects the inhomogeneous distribution of grains and material textures at the meso/microscale, and has a desirable resource-consumption level.

3) Propose designs for analyzing and eliminating flow-induced folding defects to evaluate their feasibility and generate flow-based design criteria for the development of defect-free parts and processes.

1.3 The organization of the thesis

This thesis consists of seven chapters and a reference list. It is organized into three parts. The first part consists of the research introduction and a literature review, which correspond to Chapters 1 and 2, respectively. The second part consists of four studies, which are presented in Chapters 3 through 6. The third part comprises Chapter 7, which contains the conclusions and proposals for future research. The details of each chapter are as follows.

Chapter 1 provides a brief description of meso/microforming and theories and states the size-effect-related problems in meso-/micro-scaled deformation. The chapter finishes by presenting the research objectives.

Chapter 2 presents a literature review about meso-/micro-manufacturing, size effects in meso/microforming, current microforming technologies, flow-induced folding defects, and size-related modeling and summarizes the prior contributions to addressing these problems.

Chapter 3 introduces a progressive microforming system with blanking and extrusion operations for making two types of pin-shaped plunger parts using brass sheets and investigates the grain size effect according to deformation load, dimensional accuracy, microstructural evolution, and surface quality. The chapter then discusses the grain-size-related deviation of punch stroke and part dimensions, the characteristics of shear bands and dead metal zones, and forming defects.

Chapter 4 develops a compound microforming system for a blanking-heading process used for producing plug-shaped bulk parts by directly using copper sheets. Different punch-die clearances and grain sizes of specimens are employed to study the interactive effects of geometry and grain size from the perspectives of microstructural evolution, geometrical precision, material loss, the surface defects of micro-formed parts, and the load-stroke relationship. Shear bands and dead metal zones are also identified on the cross-section of parts.

Chapter 5 outlines constitutive modeling considering grain orientations and grain boundary-interior differences. The feasibility of this model is verified through experiments and simulations with different specimens and grain sizes, and it predicts the geometrical and grain size effects on the flow stress of material. Compared with the CPFEM in simulation, this model loses a small amount of flow stress and free surface formation accuracy but has efficiency advantages. The proposed model is also applied in predicting ductile fracture using the GTN fracture criterion. This modeling considers both accuracy and efficiency in meso-/micro-scaled deformation and in forming problems of polycrystalline metallic materials.

Chapter 6 presents a quantitative design-based method with different tooling and processes employed to improve material flow. Four designs of the same flanged part are proposed with different forming sequences of various features. The most desirable design is selected by analyzing material flow during each forming process and by comparing energy consumption, the feasibility of folding avoidance, and the geometrical precision of different designs. Its physical experiments and morphological observations were conducted using three size scales.

Chapter 7 provides conclusions resulting from this thesis and suggestions for future research.

Chapter 2 Literature review

2.1 Meso-/micro-manufacturing

Manufacturing is a general term in industry, and refers to the making of products for certain applications. With respect to different scales, meso-/micro-manufacturing applies manufacturing processes to miniature products, including meso-/micro-scaled features or structures and meso-/micro-sized parts or components [45]. Micro-manufacturing is often segmented into micro-electromechanical systems (MEMS) based lithography technologies [46] and mechanical-based micro-manufacturing processes [10], as shown in **Fig. 2.1**. Lithography manufacturing generally includes photolithography, chemical etching, plating lithography, and electroplating, while mechanical-based manufacturing involves micro-mechanical machining, micro-injection molding and powder injection molding, microforming, and non-conventional micromachining including electrical-discharge-machining (EDM), electron beam machining, and ultrasonic machining, etc. In this thesis, meso-/micro-manufacturing refers to the mechanical-based manufacturing of meso-/micro-scaled structures and parts.

According to the product manufacturing method, meso-/micro-manufacturing is generally classified into several categories, including subtractive processes, additive manufacturing, and forming. Some typical manufacturing methods and processes are discussed below.

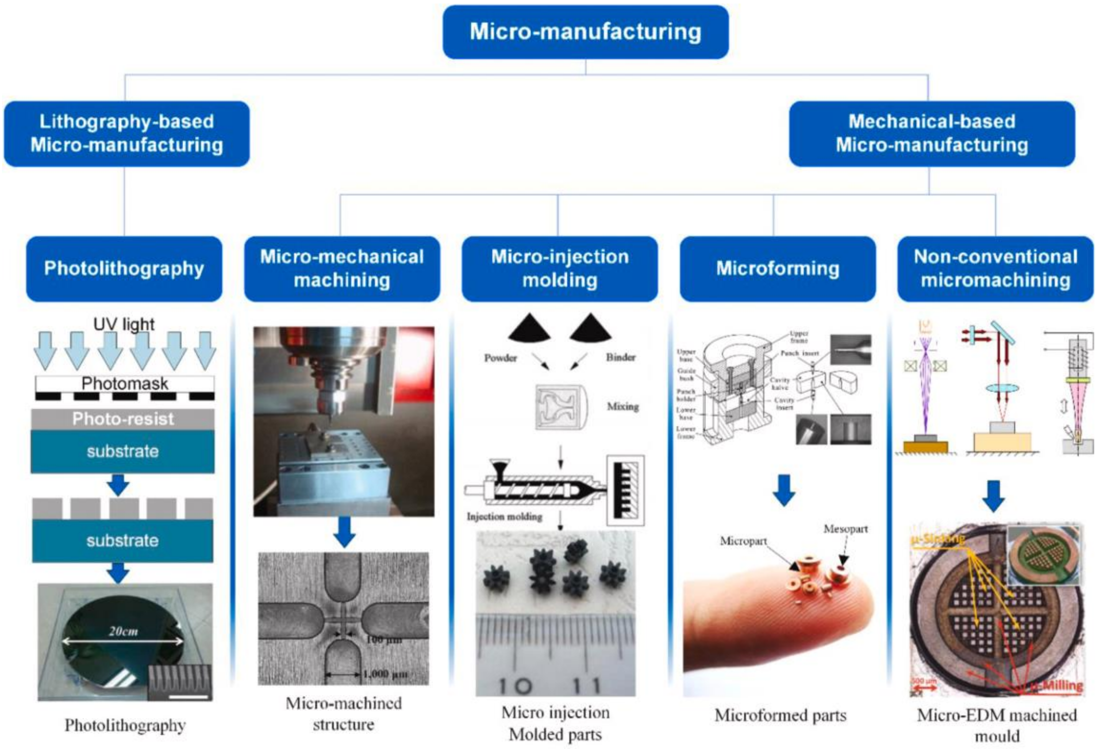

Fig. 2.1 The classification of micro-manufacturing technologies [47].

2.1.1 Subtractive processes

Subtractive processes generally refer to meso-/micro-machining, including conventional meso-/micro-mechanical cutting such as milling, turning, grinding, and polishing. [48], and non-conventional machining such as micro-EDM [49], laser beam machining [50], electron beam machining [51], photochemical machining [52], etc. Meso-/micro-machining is a process for cutting material into a desired shape and size using a controlled material-removal technology at a meso/microscale. One of the principal advantages of meso-/micro-machining is it allows one to machine ultraprecision features and structures [53], but it faces the challenge with productivity, complex geometries, and hard-to-cut materials. Thus, meso-/micro-machining is widely applied in making dies and molds for other processes.

2.1.2 Additive manufacturing

In contrast to subtractive processes, additive manufacturing (AM), also known as 3D printing, is a technique used for fabricating three-dimensional objects through material depositing, joining, or solidifying under computer control, typically layer by layer. It can be differentiated into several subcategories including fused deposition modeling (FDM) for polymer filaments, selective laser sintering (SLS) and selective laser melting (SLM) for powders, liquid binding in 3D printing, and laminated object manufacturing (LOM) [54]. In construction industries, AM has the advantages of less waste, freedom of design, and automation. Micro-AM has been developed and can be divided into three main groups, including scalable AM technologies – which are suitable for all scales – and 3D direct writing – which has been developed for microscale and hybrid processes [55].

2.1.3 Forming

Meso/microforming is defined as the forming process of meso-/micro-scaled features or parts. It has become a promising process for mass production due to its high productivity and efficiency, little material waste, net-shape or near-net-shape characteristics, and economic and environmentally friendly production [56-58]. Considering the tooling and forming process, various meso/microforming configurations are possible, such as forging, extrusion, stamping, bending, deep drawing, embossing, punching, blanking, coining, heading, and rolling [10]. Meso/microforming is achievable by scaling down the process configurations, tooling, and machines from the macroscale, but meso/microforming faces challenges of size effect related to the changing of the deformation mechanism, material properties and material and tooling interfacial conditions. The scale-down process and design must also be optimized in part by considering size effects.

2.2 Size effects in meso/microforming

Size effects refer to the deviation of some characteristics from their expected scaled value when scaling the geometrical dimensions of a part or feature up or down. Size effects comprise three main types based on the physical mechanism interaction and the related phenomena regarding density, shape (geometry), and structure [21], as shown in **Fig. 2.2** (a). In meso/microforming of metallic parts based on plastic deformation, the subcategories of geometrical size effect, grain size effect, and friction effect are focused on. These factors can further affect the meso-/micro-scaled deformation behaviors and then influence the performances of forming processes and the qualities of final parts, as shown in **Fig. 2.2** (b).

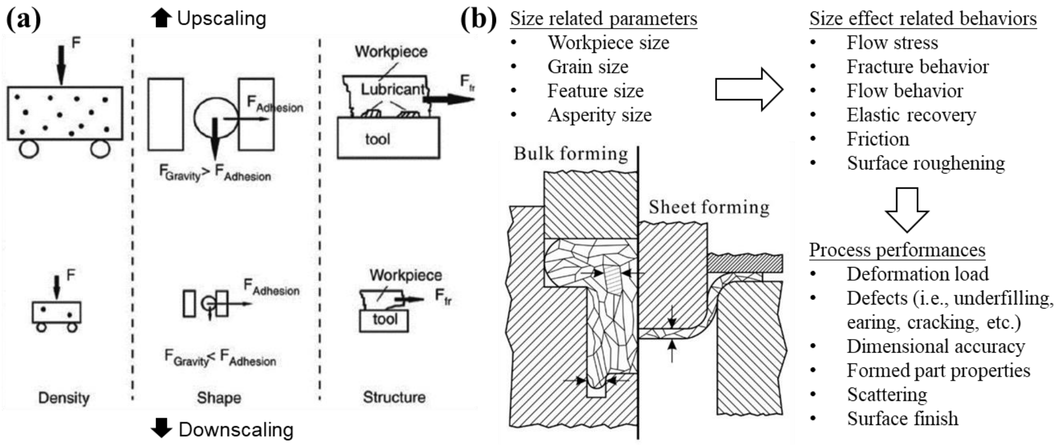

Fig. 2.2 (a) Categories of size effects during miniaturization [22]. (b) Size-effect-related issues in meso/microforming [10].

2.2.1 Size-dependent flow stress

Flow stress refers to the strength of a material during plastic deformation, which determines the deformation load and the formability during meso/microforming processes. Thus, it also affects the process parameter determination and the geometrical accuracy of the formed parts. The size effects on flow stress can be generally differentiated into geometrical size effects and grain size effects.

The geometrical size effect refers to the deviation of the properties or parameters of parts during forming from the scaled value when scaling the geometrical size without changing the forming conditions, material properties, or microstructures. The strength of metallic material can increase or decrease when scaling down. “Smaller is stronger” refers to the interaction of dislocation with obstacles impeding dislocation line length growth in micro- and nano-scaled metal crystals [59, 60], which is an unusual phenomenon within meso-/micro-scaled deformation. The decreasing geometrical size in meso/microforming generally softens the flow stress of a material, as shown in **Fig. 2.3** (a). This figure shows how, for aluminum, material strength decreases as geometrical dimensions diminish. The grain size effect refers to the variation of material properties when changing the grain size of a material. Heat treatment such as annealing under different holding times and temperatures is a common and effective way for obtaining the different grain sizes. The grain size usually grows with a longer holding time and a higher annealing temperature. Generally, a material is softened with an increase in the grain size in meso-/micro-scaled deformation, as shown in **Fig. 2.3** (b). The softening effect of the decreasing geometrical size and increasing grain size can be explained by the strengthening effect of the grain boundary that blocks the dislocation movement. With the fraction of the grain boundary to the material volume decreasing, the flow stress of material is decreased [23, 61].

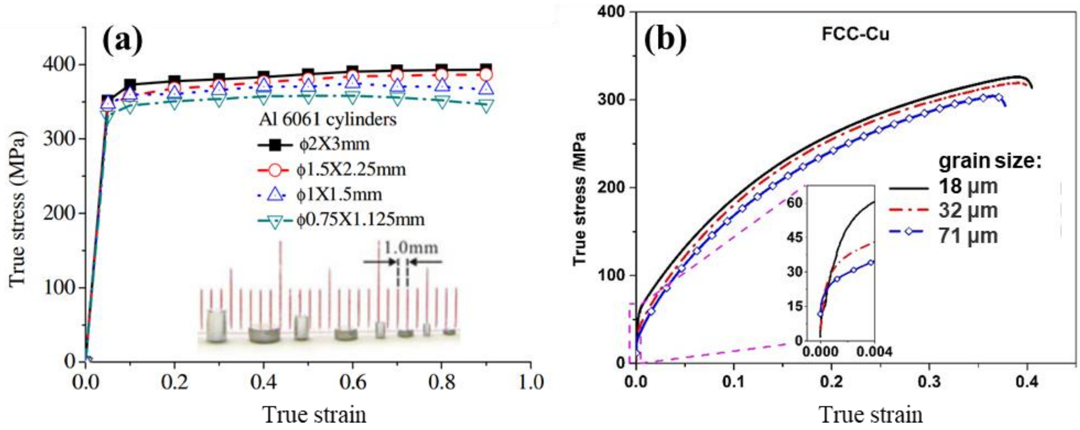

Fig. 2.3 (a) The softening effect of decreasing specimen size in compression tests for aluminum alloy [62]. (b) The hardening effect of the decreasing grain size effect in tensile tests for pure copper [31].

2.2.2 Size effect in tribology

In downscaling forming processes, the interfacial friction between tooling and the workpiece has a significant effect on the forming performance due to the constant surface topography and the high surface-to-volume ratio of meso/microparts [20]. The significantly increased interfacial friction in lubricant meso/microforming caused by size effects can be explained by the well-known open and closed lubricant pocket (OLP&CLP) model. Pawelski et al. [63] first proposed the basic concept of this theory without quantitative description. Engel [25] gave a qualitative description and explanation of this model based on the Wanheim-Bay model. Peng et al. [64] developed this model and established a new friction model that considers the size-scaled factor.

The OLP&CLP model assumes a typical material surface that is not purely smooth but contains many peaks and valleys from a micro-perspective, that is, “roughness.” When the surface of another object is pushed to the lubricated workpiece surface, the peaks start to deform plastically, leading to an increased contact surface area, which forms the real contact area (RCA). Some valleys between peaks, particularly the valleys located inside, can hold the lubricant to form closed lubricant pockets (CLPs), which can offset a portion of the normal pressure. The other roughness valleys that cannot hold lubricant are called open lubricant pockets (OLPs). The RCA, CLPs, and OLPs are illustrated in a 2D sketch in **Fig. 2.4** (a–c). In short, CLPs can reduce friction in contrast to OLPs. The geometrical size effect is reflected by the decreasing number of CLPs in microforming. In the double-cup-extrusion experiment [25], there is a region of constant height (denoted by *s* in **Fig. 2.4** [d]) induced by the scale invariance of topography, where the OLPs take into effect. With decrease in the specimen size, the ratio of OLPs increases, leading to the growth of the friction factor. The occurrence of CLPs and OLPs induces the nonuniform deformation of the surface material, which significantly affects the deformed surface properties. The volume fraction of the affected zone will be much larger when the ratio of the asperity size to specimen size is large. Friction is due to the interlocking of surface asperities. The fraction of RCAs significantly affects the interfacial friction.

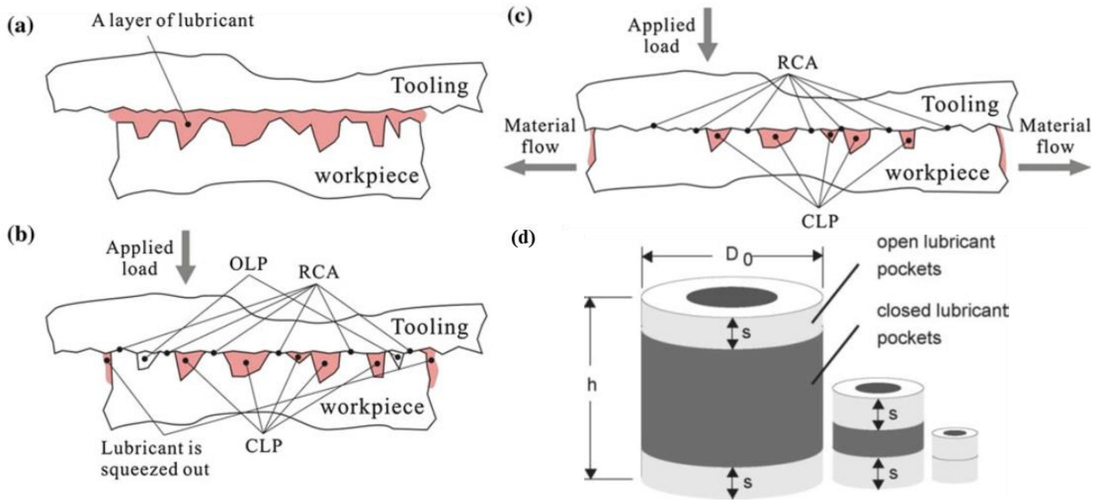

Fig. 2.4 (a) Initial state; (b) Applied force; (c) Material deform; (d) Increasing ratio of OLPs to CLPs with decreasing specimen size [25, 64].

The end surfaces of the compressed specimens with different sizes are shown in **Fig.**

2.5. This figure presents the change of RCAs with specimen size. The fraction of RCAs increases as specimen size decreases. This explains why interfacial friction increases with decreases in specimen size.

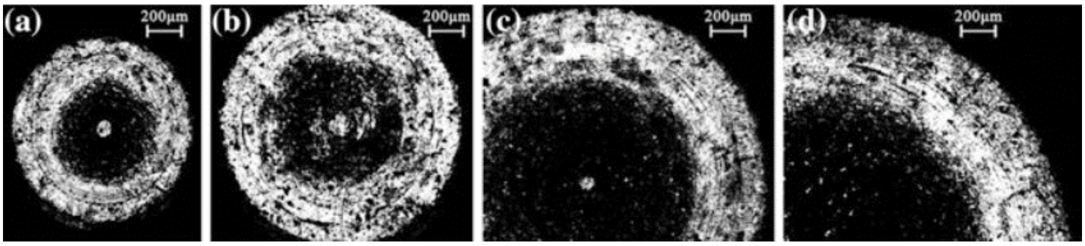

Fig. 2.5 End surface topographies of the compressed specimens [65]. Original specimen dimensions: (a) Ø0.75×1.125 mm, (b) Ø1×1.5 mm, (c) Ø1.5×2.25 mm and (d) Ø2×3 mm.

Moreover, for the size effect on dry friction in meso-/micro-scaled deformation, the OLP&CLP model is not feasible. The interfacial friction is generally due to the specific contact condition, including the contact pressure or the surface properties of the workpiece and tooling [66, 67]. Some studies have also indicated that dry friction is affected by specimen and grain size [68], as shown in **Fig. 2.6**. It has been shown that, in the range from 1 to 9 mm, the friction factor is significantly increased by an increase in the specimen diameter and a decrease in grain size, and the rising tendency diminishes with an increase in the specimen diameter.

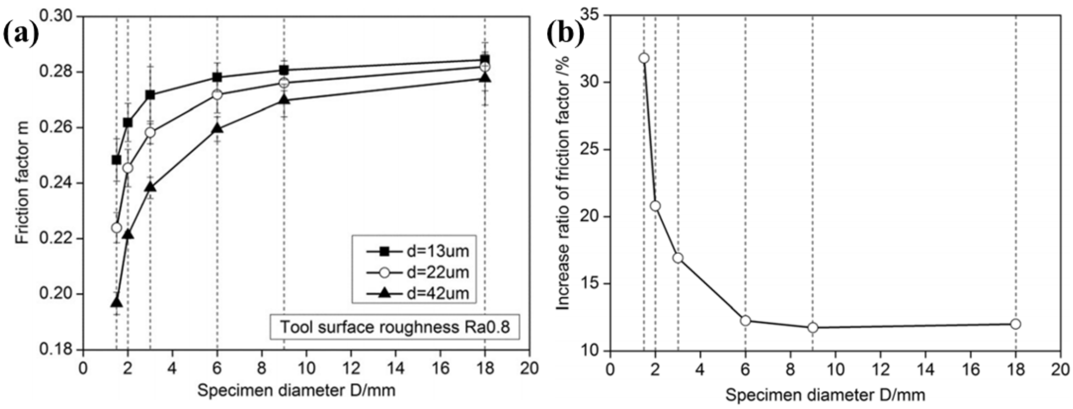

Fig. 2.6 (a) The variation of the friction factor in dry conditions with specimen diameters and grain sizes and (b) its increase ratio with specimen diameters [68].

2.2.3 Size effect on deformation behaviors

Regarding the meso-/micro-scaled deformation of materials used for making meso/microparts, the value change in size-effect factors results in the variation of deformation behaviors and process performances, such as material flow, forming load, surface roughening, scattering, dimensional accuracy, defect formation, and so on. This variation in deformation behaviors is significantly different from those at a macroscale.

Regarding the forming load, Zheng et al. [12] developed a progressive forming system to produce micro-/meso-flanged parts including four forming operations, as shown in **Fig. 2.7** (a). By using this progressive forming process, the scaling factor (SF) is defined as the ratio of the thickness of a workpiece to 1 mm, with the values of 0.5, 1.0, and 1.5, respectively, representing microscale, small mesoscale, and large mesoscale. The conical-shaped extrusion operation with the well-characterized forming curves is shown in **Fig. 2.7** (b–d). The forming pressure is decreased with an increase in grain size, and this effect becomes more obvious with the SF of 0.5, while this effect almost disappears with the SF of 1.5. Regarding the geometrical size effect, the forming pressure with the normalized stroke increases with a decrease in the SF, as shown in **Fig. 2.7** (e). For the SF of 0.5, the forming pressure is more than 20% higher than that for the SFs of 1.0 and 1.5. Therefore, the geometrical and grain size effects have a significant effect on deformation behaviors in multi-scaled forming processes.

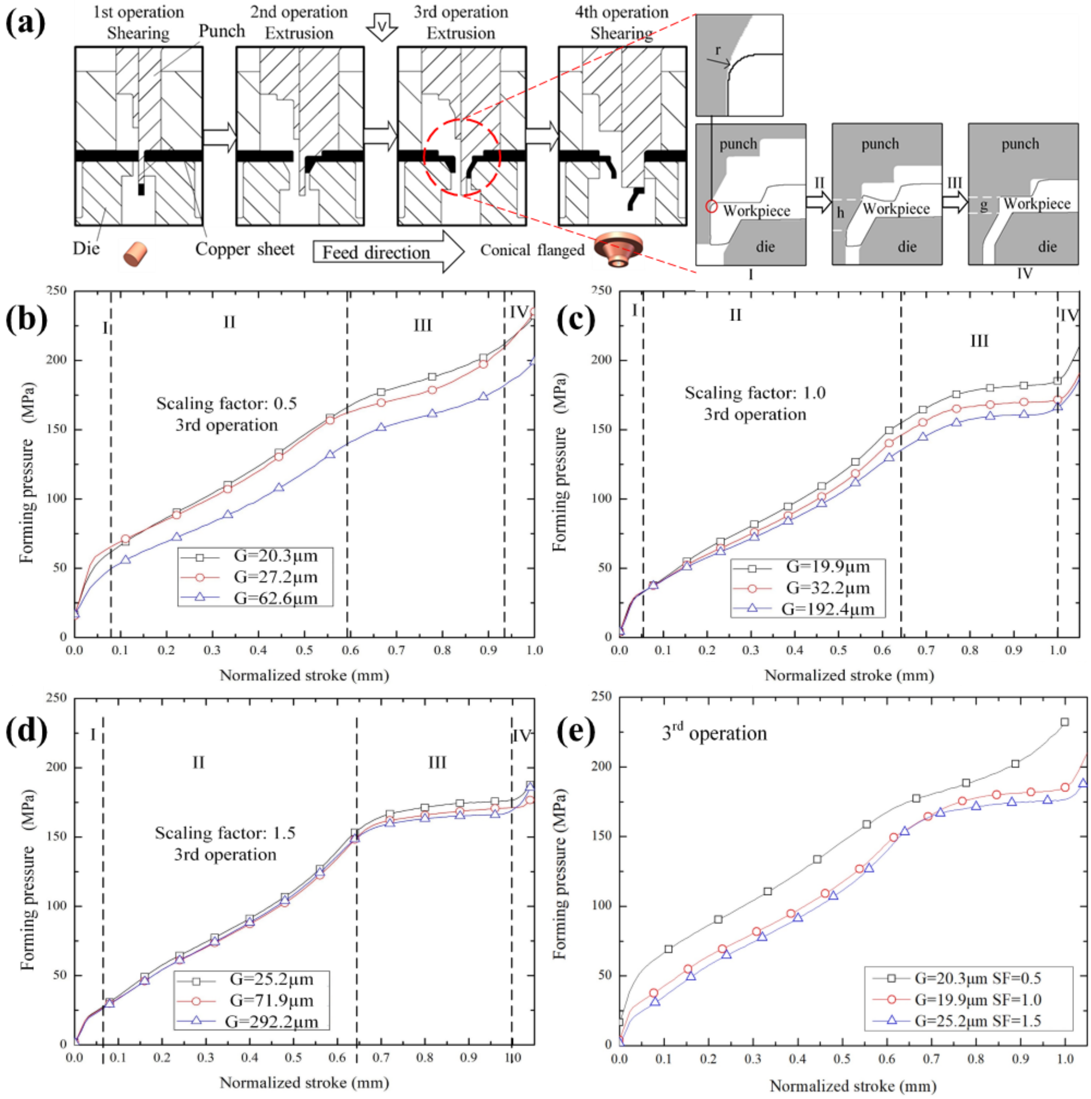

Fig. 2.7 (a) The progressive forming process for making conical flanged parts. The forming pressure curves in the third operation of (b) micro-, (c) small meso-, and (d) large meso-scaled progressive forming with different grain sizes. (e) The forming pressure with the similar grain size in different scales [12].

As for the dimensional accuracy and deformation uncertainty, inhomogeneous deformation arises in the case with coarse grains, as shown in **Fig. 2.8**. The irregular shapes of the compressed copper cylinders are caused by the random characteristics and orientations of individual grains. Each grain is a unique deformation system with a close-packed slip-plane direction, which induces its anisotropic properties. With an increase in grain size, the number of grains comprising the specimen decreases, and the homogeneity of the material is reduced, which results in serious uncertainty of deformation and then an increase in the scattering of the dimensional accuracy of final parts.

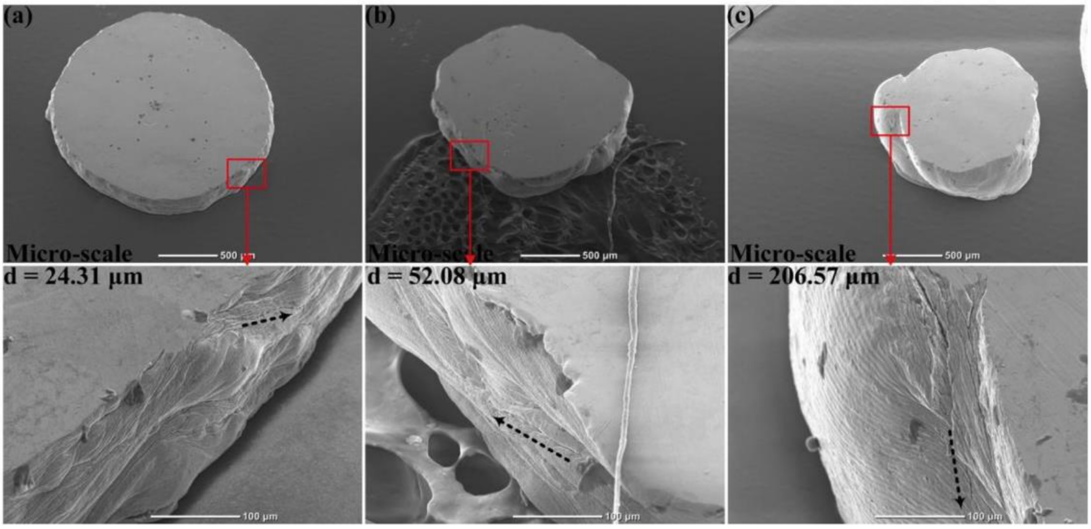

Fig. 2.8 Scanning-electron-microscope morphography of micro-compressed cylinders with different grain sizes of (a) 24 µm, (b) 52 µm, and (c) 207 µm [69].

2.2.4 Size effect on ductile fracture behaviors

Size effects can significantly influence the ductile damage and fracture behaviors in meso-/micro-scaled deformation. There are two damage types on the fracture surface of **Fig. 2.9**, which are “cup and cone”. The “cup” is induced by the dimple fracture, which is attributed to the initiation, growth, and coalescence of microvoids forming at the grain boundaries or inclusions. The “cone” with the shear lip is dominated by the shear fracture. With an increase in grain size, the fracture mode changes from a dimple-dominant fracture to a shear-dominant fracture, which is reflected by the decrease in dimples.

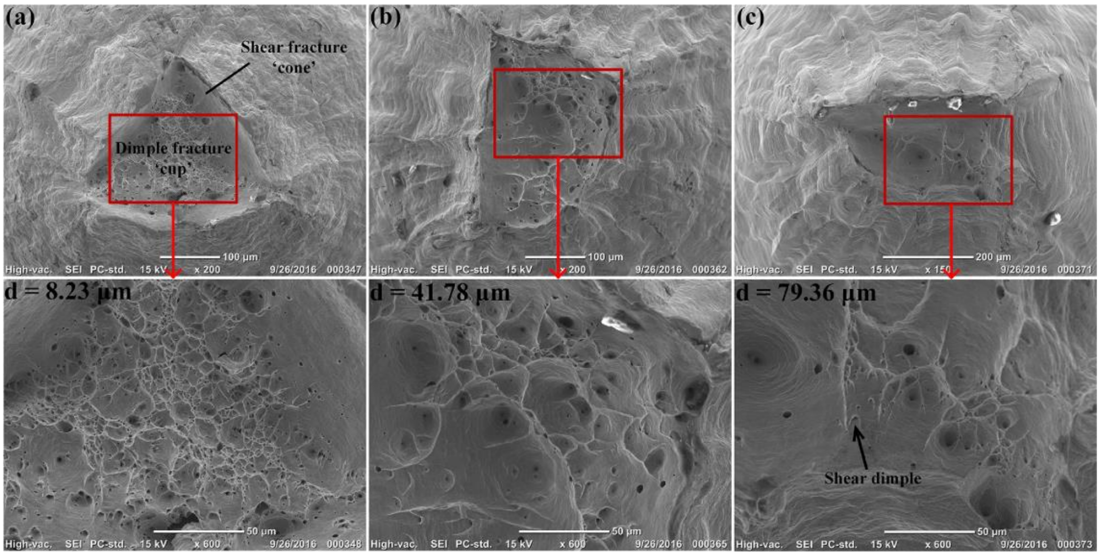

Fig. 2.9 Scanning-electron-microscope fractography of tensioned bar specimens with different grain sizes of (a) 8 µm, (b) 42 µm, and (c) 79 µm [70].

2.3 Microforming processes

Microforming is an economical and promising process for fabricating micro-scaled metallic parts. It is generally employed from macroforming, but the occurrence of size effects requires that many unknowns concerning deformation behaviors be reconsidered. This section lists some of the state-of-the-art of microforming techniques and their characteristics. These techniques include micropunching, microblanking, microextrusion, microheading, and progressive microforming.

2.3.1 Micropunching/microblanking

Micropunching and microblanking processes are both based on shearing deformation. Microblanking focuses on the blanked-out portion of workpieces and its quality, while micropunching focuses on the remaining portion and its desirable profile [58]. Micropunching is a simple but efficient process for fabricating microholes at a low cost compared with micro-machining processes such as microdrilling and microelectro-discharge machining. Microblanking, by contrast, is employed to produce microsheets or to be the last operation in blanking out micro-parts. In traditional macropunching/macroblanking processes, the dimensions of punches and dies and their tolerances are important for the forming qualities. In micropunching and microblanking processes, however, the tolerances and the surface finish of tooling are important, and these must be focused on to improve micropunching/microblanking forming qualities.

2.3.2 Microextrusion

Microextrusion is a process based on the plastic deformation (mainly compressive and shearing) of material, and it can be divided into three types according to the directions of material flows. These types are forward extrusion, backward extrusion, and compound extrusion. With forward extrusion, the material billet is compressed in the die, and material flows in the same direction as the movement of the punch, while with backward extrusion, material flows in the opposite direction of the punch's movement. With compound extrusion, the forward and backward material flows co-occur in a single forming process.

In microextrusion, the interfacial friction between tooling and a workpiece is an important factor affecting the deformation load and the ejection of final parts. In traditional macroextrusion, the friction can be evaluated according to the amount of backward flow of material in compound extrusion [71]. However, the emergence of size effects induces many unknowns and random characteristics in microextrusion that increase the difficulty of predicting and controlling the forming processes.

2.3.3 Microheading

Microheading is a process where micro-scaled billet material in the form of pin or rod deforms locally to form an axisymmetrical bulge-shaped feature. In microheading, the ovality of the bulged feature is enhanced due to the asperity size effect [72]. Due to the linear texture on the tooling surface with grinding finish, the interfacial friction between the material and the tooling in the direction parallel to the linear texture is different from the friction in the direction perpendicular to the linear texture. In microheading, this difference is enhanced, so the fine-polished tooling surface is necessary to avoid the elliptical-shaped feature.

2.3.4 Progressive microforming

The fabrication of microparts generally involves a process chain that contains one or several forming processes used to form different features of final parts, and the design of the process chain determines the productivity and quality of the fabrication. To fabricate a micropart through microforming, the micropart is usually formed from bulk microbillets or sheet metals. The handling, transportation, positioning, and ejection of billets and preforms among different forming processes are problems that must be solved to have a promising process chain. To solve issues in handling, transporting, and ejection in sheet-based forming, the concept of progressive sheet-metal forming has been proposed. This unique process aims at making complex structures or multi-feature parts through the direct use of sheet metals. The term “progressive” means that the process chain involves two or more single forming steps and employs progressive dies. Each step in the process chain has its designed stroke and predefined task. Several steps in the process chain are conducted simultaneously, and then the sheet metal with preforms is moved to the next position so that several forming steps can be conducted progressively with great efficiency. In progressive microforming, the material flows in each forming step and the mechanism of fracture formation are crucial and must be studied.

2.4 Flow-induced folding defects in metal forming

Defects in metal forming processes can be classified into six groups including folding, shear defects, cracks, surface defects, form defects, and structural defects [44]. Folding is defined as defects in the appearance of material contact without fusion between the surface material and the internal or surface material. There are several types of folding, including cold slut, collapse, lap, and suction [44]. Folding defects are some of the most common defects in metal forming induced by undesirable material flow, where some crucial flow-related parameters should be noted, including strain rates that are too high, pressure that is too high, inconvenient material flows, inhomogeneous deformation, and gas inclusions. Gao et al. [73] classified the folding defects into three groups based on their forming mechanism and flow characteristics. These three groups are confluence type, bending type, and local-loading type, as shown in **Fig. 2.10**. Confluence-type folding is characterized by a cavity induced by a local lack of material, which is usually caused by two-side neighboring material flows that fill the cavity. Bending-type folding begins as a V-shape and then undergoes closure to form a folding defect, which usually happens when a long and thin wall or pipe is bent severely during compression. Local-loading-type folding is induced by a preformed bulge or step being pressed in the subsequent forging step to form a folding defect.

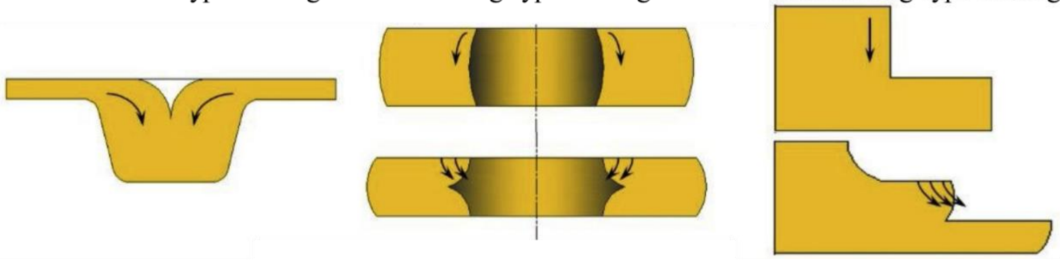

Fig. 2.10 Schematic of three typical material flow characteristics that lead to folding defects, namely, confluence-type folding, bending-type folding, and local-loading-type folding [73].

2.5 Modeling of size effects

Many different empirical and theoretical constitutive models have been proposed and developed to explain how size effects affect meso-/micro-scaled deformation. This section introduces and reviews some well-known empirical equations, namely the Hall-Petch relationship [74, 75], the surface layer model [40, 76], the composite model [77-79], the lattice-based crystal plasticity theory [80], and the porous metal fracture model [81, 82].

2.5.1 Modified Hall-Petch relationship

The most famous empirical model for describing the grain size effect on material yield stress (σ_y) is the Hall–Petch relationship [74, 75], which is expressed in the following:

$$\sigma_y = \sigma_0 + K_y d^{-\frac{1}{2}} \tag{2.1}$$

where σ_y is the yield stress, σ_0 is the starting stress for dislocation movement, K_y is the strengthening coefficient, which is a material constant, and d is the average grain size. Armstrong [83] further developed Eq. (2.1) by incorporating Taylor's theory [38] into the following equation:

$$\sigma(\varepsilon) = m\tau_R(\varepsilon) + K(\varepsilon)d^{-\frac{1}{2}} \tag{2.2}$$

where m is the Taylor orientation factor, τ_R is the critical resolved shear stress (CRSS)，and K is the shear stress intensity for the transmission of plastic flow at grain boundaries.

2.5.2 Surface layer model

Miyazaki et al. [84] revealed that the dislocation tangles only occur near the threefold node of grain boundaries and that a few dislocations are heterogeneously distributed inside the surface-layer grains of material. Thus, the deformation behavior of the surface-layer material is different from the inner material. The surface-layer grains have less constraint from adjacent grains in contrast to the internal grains, and the surface grains have lower flow stress. For the coarse-grained material, the decrease in flow stress could be due to the change in the volume fraction of surface-layer grains. The flow stress can thus be determined by both the surface-layer and internal grains and expressed as follows:

$$\sigma(\varepsilon) = \alpha_s\sigma_s(\varepsilon) + \alpha_i\sigma_i(\varepsilon) \tag{2.3}$$

where $\sigma_s(\varepsilon)$ and $\sigma_i(\varepsilon)$ are the flow stresses of the surface-layer and internal grains, respectively. They represent the function of strain ε. α_s and α_i are the volume fractions of surface-layer and internal grains. At a macroscale with fine-grained material, the quantity of grains in the cross-section of the specimen is large, and the volume fraction of surface-layer grains is small. Regarding a micro-scaled specimen and a large grain size, there are only a few grains constituting the specimen, thus the volume fraction of surface-layer grains is increased tremendously (as shown in **Fig. 2.11**), which leads to the decrease of flow stress.

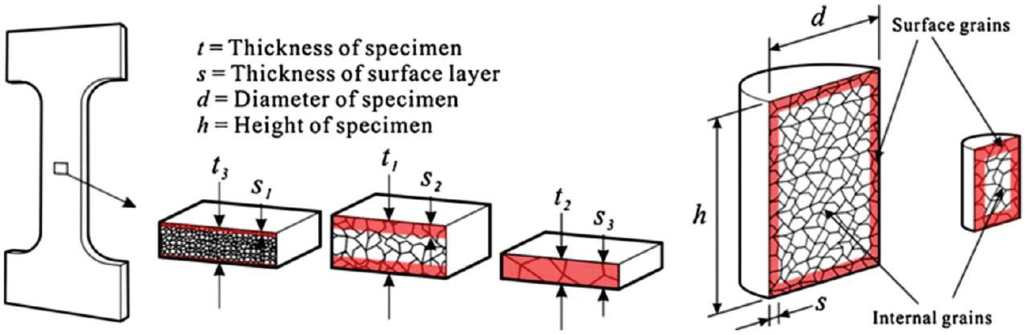

Fig. 2.11 Change in the volume fraction of surface grains following change in specimen and grain sizes [85].

2.5.3 *Composite model*

Meyers [41] proposed a composite model that considers polycrystalline metallic material as a composite material with a continuous framework of work-hardened grain boundaries and discontinuous grain interiors. The flow stress of the composite material is expressed as follows:

$$\sigma(\varepsilon) = f_{GI}\sigma_{GI}(\varepsilon) + f_{GB}\sigma_{GB}(\varepsilon) \tag{2.4}$$

where $\sigma(\varepsilon)$ is the flow stress of the material, σ_{GI} and σ_{GB} represent the flow stress located at the grain interior and grain boundary, respectively, and f_{GI} and f_{GB} represent the volume fractions of the grain interior and grain boundary, respectively.

The thickness of grain boundaries can be expressed in terms of grain size as follows [86]:

$$t_g = kd^n (0 < n < 1) \tag{2.5}$$

where k and n are constants for a given material.

The microstructures divided into grain interiors and a grain boundary framework are shown in **Fig. 2.12**. For the largest grain size of 100 μm, the grain boundary region is hard to distinguish, whereas, for the smallest grain size of 1 μm, the grain boundary region occupies an obvious portion of the entire grain.

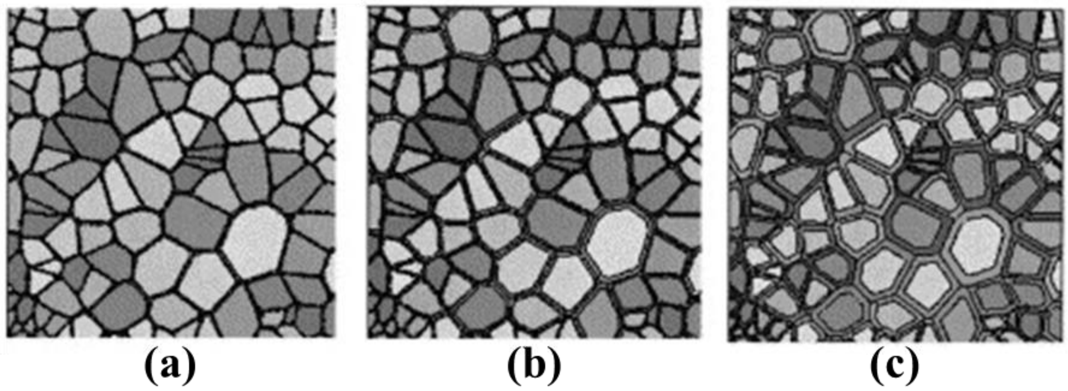

Fig. 2.12 Simulated polycrystalline aggregate based on Eq. (2.5): (a) d = 100 μm, t_g = 3.33 μm; (b) d = 10 μm, t_g = 0.665 μm; and (c) d = 1 μm, t_g = 0.133 μm [78].

2.5.4 Crystal plasticity

A slip system is composed of a set of symmetrically identical slip planes and an associated family of slip directions along the most possible direction where dislocations could occur with plastic deformation. Depending on the type of lattice (face-centered cubic crystals, body-centered cubic crystals, or hexagonal close-packed crystals), different slip systems are present in materials, as shown in **Fig. 2.13**. When force is applied to the crystal material, the crystal lattices glide along a specific slip direction and on a specific slip plane. Slip always occurs on the close-packed planes that have the greatest density of atoms and along the close-packed directions where there are the most atoms in a certain length. A slip plane and a slip direction constitute a slip system, where the critical resolved shear stress τ_R is required to describe the slip system, as shown in the following:

$$\tau_R(\varepsilon) = cos\varphi cos\lambda \cdot \sigma = \beta \cdot \sigma \tag{2.6}$$

where β is the Schmid factor [40, 87] related to the grain orientation, and $0 < \beta \leq \frac{1}{2}$; σ is the applied stress; φ is the angle between the normal stress and the normal direction of the slip plane; and λ is the angle between the slip direction and the normal stress, as shown in **Fig. 2.13 (**d).

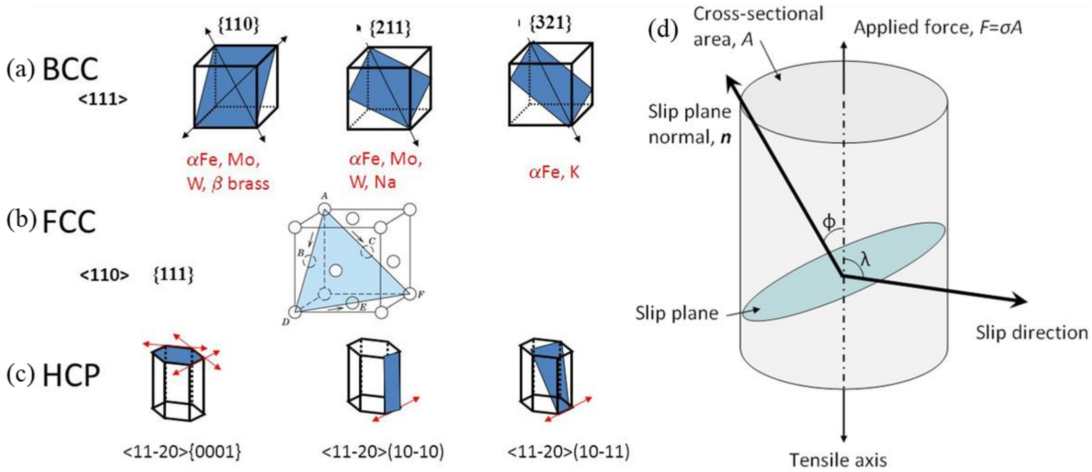

Fig. 2.13 Slip systems of (a) body-centered cubic, (b) face-centered cubic, and (c) hexagonal close-packed lattices, and (d) critical resolved shear stress for a single slip system.

To quantitatively study the inhomogeneous material deformation occurring during the compound microforming process, the CPFEM that considers material texture was employed in simulations. Crystal plasticity is a physical-based plasticity theory that can represent the plastic deformation of metals at the meso/microscale. The dislocation of metallic crystals in slip systems is described by a continuum framework [43]. The plastic deformation is assumed to be solely due to crystallographic dislocation slips. The lattice of a crystalline material undergoes elastic deformation and rotation. The material flows through the crystal lattice via a dislocation motion. The total deformation gradient $\boldsymbol{F}$ is shown as follows:

$$\boldsymbol{F} = \boldsymbol{F}^e \boldsymbol{F}^p \qquad (2.7)$$

where $\boldsymbol{F}^p$ is the plastic shear deformation to an intermediate configuration whose lattice orientation and spacing are the same as the original reference configuration, and $\boldsymbol{F}^e$ denotes the stretching and rotation of the lattice. The decomposition of Eq.(2.7) along with the velocity gradient $\boldsymbol{L}$ is shown as follows:

$$\begin{cases} \boldsymbol{L} = \dot{\boldsymbol{F}}\boldsymbol{F}^{-1} = \boldsymbol{L}^e + \boldsymbol{F}^e\boldsymbol{L}^p\boldsymbol{F}^{e-1} \\ \qquad \boldsymbol{L}^e = \dot{\boldsymbol{F}}^e\boldsymbol{F}^{e-1} \\ \qquad \boldsymbol{L}^p = \dot{\boldsymbol{F}}^p\boldsymbol{F}^{p-1} \end{cases} \tag{2.8}$$

where $\boldsymbol{L}^e$ and $\boldsymbol{L}^p$ are the elastic and plastic distortion rates, respectively.

By introducing the Schmid law [88], the plastic distortion rate is summarized by the shearing rates on each active slip system as follows:

$$\boldsymbol{L}^p = \sum_{\alpha} \dot{\gamma}^{\alpha}(\boldsymbol{s}^{\alpha} \otimes \boldsymbol{m}^{\alpha}) \tag{2.9}$$

where $\boldsymbol{s}^{\alpha}$ and $\boldsymbol{m}^{\alpha}$ are the unit vectors along the slip direction and the normal to the slip plane of the α^{th} slip system in the intermediate configuration, $\boldsymbol{s}^{\alpha} \otimes \boldsymbol{m}^{\alpha}$ is the Schmid factor of the active slip system, and $\dot{\gamma}^{\alpha}$ is the plastic shear strain rate in the α^{th} slip system. The resolved shear stress τ^{α} on the α^{th} slip system can be expressed as follows [42]:

$$\tau^{\alpha} = \boldsymbol{F}^e \cdot \boldsymbol{F}^{e^T} \cdot \boldsymbol{S} : (\boldsymbol{s}^{\alpha} \otimes \boldsymbol{m}^{\alpha}) \tag{2.10}$$

where $\boldsymbol{S}$ is the second Piola-Kirchhoff (PK2) stress tensor. In addition, the rate-dependent kinetic law for face-centered cubic metallic crystals was used in this research, where the shearing rate $\dot{\gamma}^{\alpha}$ of the α^{th} slip system is designated as [89]:

$$\dot{\gamma}^{\alpha} = \dot{\gamma}_0 \left|\frac{\tau^{\alpha}}{g^{\alpha}}\right|^{\frac{1}{m}} sgn(\tau^{\alpha}) \tag{2.11}$$

where $\dot{\gamma}_0$ is the reference strain rate, g^{α} is the current strength of the α^{th} slip system, and m is the rate sensitivity parameter. g^{α} evolves with the accumulation of dislocation in a crystal with work-hardening. Its rate $\dot{g}^{\alpha}$ can be calculated as follows:

$$\dot{g}^{\alpha} = \sum_{\beta} h_{\alpha\beta} \left| \dot{\gamma}^{\beta} \right| \tag{2.12}$$

where $h_{\alpha\alpha}$ $(\alpha = \beta)$ and $h_{\alpha\beta}$ $(\alpha \neq \beta)$ are the self and latent slip hardening moduli, respectively. The latent hardening modulus is obtained via the following equation:

$$h_{\alpha\beta} = q h_{\alpha\alpha} \tag{2.13}$$

where q is a factor representing the relationship between slip systems.

Kalidindi et al.'s hardening formulation [90] for the self-hardening module was selected in this work and is expressed as follows:

$$h_{\alpha\alpha} = h_0 \left(1 - \frac{g^{\alpha}}{\tau_s}\right)^{a} \tag{2.14}$$

where h_0 is the initial hardening modulus, τ_s is the shear stress where large plastic flow initiates, and a is the rate sensitivity of the rate of strain hardening.

2.5.5 Porous material fracture model

Ductile fracturing occurring in metallic materials is induced by the mechanism of nucleation, growth, and coalescence of microvoids. Gurson's porous metal plasticity model [91], later modified by Tvergaard and Needleman [92] (GTN) is one of the most famous models for describing ductile fracture in metallic materials. The yield function of the GTN model is expressed in the following:

$$\Phi = \left(\frac{\bar{\sigma}}{\sigma_y}\right)^2 + 2q_1 f^* \cosh\left(-\frac{3q_2 p}{2\sigma_y}\right) - \left(1 + q_3 {f^*}^2\right) \tag{2.15}$$

where $\bar{\sigma}$ is equivalent stress (von Mises stress), σ_y is the flow stress of material, $p =$

$-\frac{1}{3}\sigma_{kk}$ is hydrostatic pressure, and q_1, q_2, and q_3 are constitutive parameters, which are 1.5, 1.0, 2.25, respectively. f^* was introduced to account for the final material failure for void coalescence, which is a function of the void volume fraction f and is modeled as follows:

$$f^* = \begin{cases} f, \ \ if\ f \le f_c \\ f_c + \dfrac{f_f^* - f_c}{f_f - f_c}(f - f_c), \ \ if\ \ f_c < f < f_f \\ f_f^*, \ \ if\ f \ge f_f \end{cases} \tag{2.16}$$

where f_c is the critical value of the void volume fraction, f_f is the final value of the void volume fraction when the material has completely lost its stress carrying capacity, and $f_f^* = (q_1 + \sqrt{q_1^2 - q_3})/q_3$. The increase in f is defined as the sum of increments due to void nucleation $df_{nucleation}$ and void growth df_{growth}.

$$\begin{cases} df = df_{nucleation} + df_{growth} \\ df_{nucleation} = \dfrac{f_N}{S_N\sqrt{2\pi}} \exp\left[-\dfrac{1}{2}\left(\dfrac{\bar{\varepsilon}^p - \bar{\varepsilon}_N}{S_N}\right)^2\right] \\ df_{growth} = (1 - f)d\varepsilon_{ii}^p \end{cases} \tag{2.17}$$

where f_N, S_N, and $\bar{\varepsilon}_N$ are constants and f_0 is the initial volume of voids.

2.6 Summary

Size-related variations and flow-induced defects are the most critical issues in meso/microforming that hinder the application of this unique technology. The size-dependent characteristics of forming processes and formed parts/structures have been investigated in prior research, and many modeling and theories have been established and developed for the analysis of size-dependent deformation behaviors of metallic materials. Their advantages and disadvantages are summarized in **Table 2.1**. However, progressive and compound meso/microforming has arisen for only a decade, thus extensive investigation on this novel technology is needed. There is also a lack of universal modeling methods to deal with the small-scaled deformation in engineering forming issues. In this research, new progressive and compound microforming systems were developed and the size-related performances of processes and parts were explored, and the mechanisms and avoidances of folding defects in microforming were investigated. In addition, appropriate modeling for forming issues was proposed and verified for its feasibility.

Table 2.1 Pros and cons of size effect modeling

Modeling	Pros	Cons
Hall-Petch	Easy-to-use	Empirical model
Surface layer model	Easily data fitting; reflect the difference between surface and internal grains	Do not consider the material inhomogeneity
Composite model	Easily data fitting; reflect the strengthening of grain boundaries	Do not consider the material inhomogeneity
Crystal plasticity	Physical-structure-based model; accurate	Consume too much calculation resource
Porous fracture (GTN)	Predict ductile fracture	Do not consider size effect

Chapter 3 Progressive microforming of pin-shaped plunger parts

3.1 Introduction

The increasing trend of product micromation promotes the demand for more and more microparts used in electronics, automotive, and many other industrial clusters [1, 2]. To meet this demand, micro-manufacturing technologies thus emerged in different forms such as micro-machining, micro-injection, microforming, and micro-assembly [93]. As one of the miniaturized products and a type of micro-connector with good durability and sturdiness, pogo-pin, usually assembled in a plastic housing, is a sort of device widely used in electronics to realize a nonpermanent and flexible electrical connection between two printed circuit boards (PCBs), which is comprised by a plunger (has different designs on the market), a barrel and a spring in between, as illustrated in **Fig. 3.1**. Each part in the assembly of pogo-pin is micropart which has at least two dimensions less than 1 mm. Nowadays, the plunger and barrel parts of pogo-pin are conventionally fabricated by micro-machining, which needs a few time-consuming steps for making different features. Additional machining steps are employed to fabricate multi-structures (for example, flat compared to tail, anti-drilling, and so on), and to meet the required tolerance and qualities, many factors should be considered, viz., cutting speed, feed rate, surface finish, and tooling defection, etc. [94]. On the other hand, in microforming, no extra forming step but only improved tooling with suitable geometry is required for complex structures, which is more controllable with the same set of tooling. It thus has been proven to be promising for its higher efficiency and material utilization and good mechanical properties of the final parts

[11]. To deal with the problems in handling, transporting, and ejection of billet/preform/final part in forming process and facilitate the feasible application of microforming in industries, the so-called progressive microforming has been developed and matured, which is a potential method to realize the industrial wide application of microforming for mass production [13]. Progressive microforming is to directly employ sheet metals to fabricate bulk microparts by progressive microtools comprised of several forming operations with a given sequence, in such a way one or more specific features of microparts to be made are formed in each progressive forming operation and the complex microparts with various complex miniaturized features are eventually produced. The primary advantages of this process include precise alignment of tooling and workpiece, easy transport of preform to next operation, and efficient ejection of final parts by blanking operation [57]. In this research, the probability of fabrication of pin-shaped parts by using progressive microforming technology was explored and a microforming system aiming at efficiently producing pogo-pin was developed. By addressing the obstacles in terms of deformation and grain size effect, the in-depth understanding and the scientific insight into the process was developed.

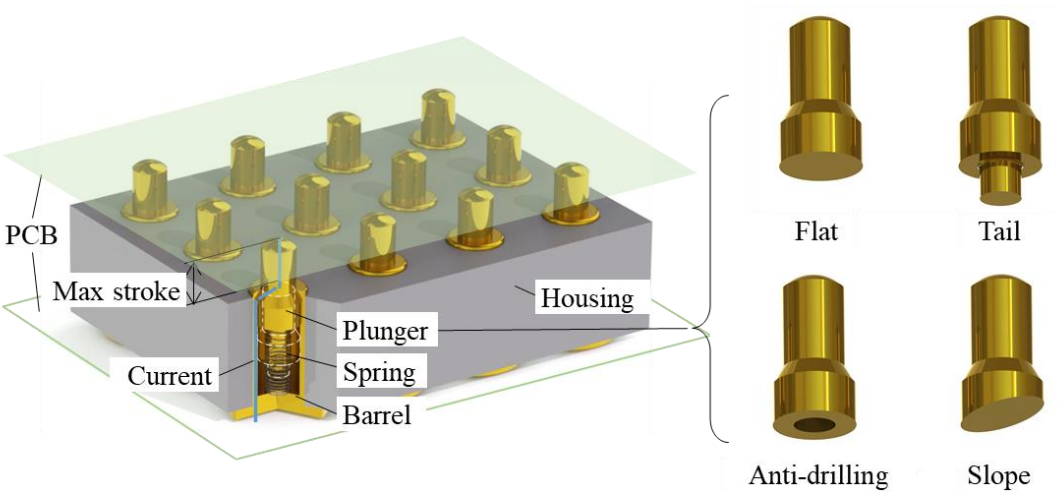

Fig. 3.1 Work situation and the structure of pogo-pins.

Although prior studies on the microforming process and the fabricated microparts were conducted, there is still a lack of a thorough investigation of the progressive microforming of complex pin-shaped microparts. Pin-shaped parts are not only employed as the plunger of connectors, but also applied in other electronic components. In this research, a progressive microforming system with two operations of blanking and extrusion by directly using sheet metals was developed and two types of pin-shaped microparts with and without tail features under different grain size conditions were fabricated. The load-stroke curves of the forming processes with three deformation stages of various microstructure were presented. The grain size effect affected microstructural evolution and the dimensional deviation of the microformed microparts were systemically investigated. The finite element method considering grain size effect was also performed to investigate the forming mechanism of the shear band. The typical forming defects and fractures on micropart surfaces were observed and their formation was discussed. The findings of this research thus enrich the knowledge and understanding of the process to support the design of complex pin-shaped microparts and progressive microforming tooling and promote the wide application of this efficient microforming process as an efficient alternative to replacing the conventional micro-machining.

3.2 Theoretical model in simulation

To get the mechanical response and performance of the experimental material and applied in numerical analysis, the coupled constitutive model of surface layer model and Hall-Petch relation was developed and detailed formulated by fitting of the experimental data to represent the flow stress of the materials with different grain sizes. The uniaxial tensile tests for brass CuZn35 were conducted to obtain the experimental data for model generation with five repeated tests with the thickness of 1.5 mm and the grain size of 11, 25, 133 μm. The whole experiment followed the standard of ASTM: E8/E8M. In prior studies, the surface layer model was used which assumes the specimen is comprised of two parts, viz., surface grains, whose properties are rather similar to single crystal, and inner grains, which is polycrystal and the grain boundary strengthening theory takes effect [95]. The Hall-Petch relation combined with the surface layer model for the flow stress is illustrated by the following equation:

$$\begin{cases} \sigma_s(\varepsilon_p) = m\tau_R(\varepsilon_p) \\ \sigma_i(\varepsilon_p) = M\tau_R(\varepsilon_p) + k(\varepsilon_p)d^{-\frac{1}{2}} \\ \sigma(\varepsilon_p) = \eta\sigma_s(\varepsilon_p) + (1-\eta)\sigma_i(\varepsilon_p) \end{cases} \tag{3.1}$$

where σ is the flow stress. σ_s and σ_i are the flow stress contributed by surface grains and inner grains. k is a constant with a given strain related to material properties. ε_p is the plastic strain. τ_R is the critical resolved shear stress. m and M are the orientation factor with the value of 2 for single crystal and 3.06 for FCC polycrystal, respectively. η is the fraction of surface grains, and d is the grain size. To determine the coefficients in the above equations, the curve fitting based on the experimental data is conducted. Firstly, the grains on the surface layer are ignored. According to the Hall-Petch equation, the flow stress has a linear correlation with the inverse of the square root of grain size when the plastic strain is fixed. As shown in **Fig. 3.2**, $M\tau_R$ is established based on the increments of the fitted linear functions, and k can be obtained based on the slopes. These two coefficients can be fitted in the power-law function with plastic strain $y=a+bx^c$.

$$\begin{cases} \tau_R(\varepsilon_p) = 388.7{\varepsilon_p}^{1.705} \\ k = 0.903 - 2.162{\varepsilon_p}^{1.705} \end{cases} \tag{3.2}$$

Secondary, the surface grains are considered to modify the existing model. According to the grain localization model proposed by Lai et al. [40], the fraction of surface grains in the sheet material is determined by $\eta = 2d/t$, where t is the thickness of the specimen. Put the Eq.2 into Eq.1, the final fitted equation for brass CuZn35 is:

$$\sigma(\varepsilon_p) = \left(0.903d^{-\frac{1}{2}} + 1189{\varepsilon_p}^{1.043} - 2.162d^{-\frac{1}{2}}{\varepsilon_p}^{1.705}\right) + \eta\left(-0.903d^{-\frac{1}{2}} - 412{\varepsilon_p}^{1.043} + 2.162d^{-\frac{1}{2}}{\varepsilon_p}^{1.705}\right) \quad (3.3)$$

The function curves of Eq.(3.3) and the experimental data are illustrated in **Fig. 3.3**.

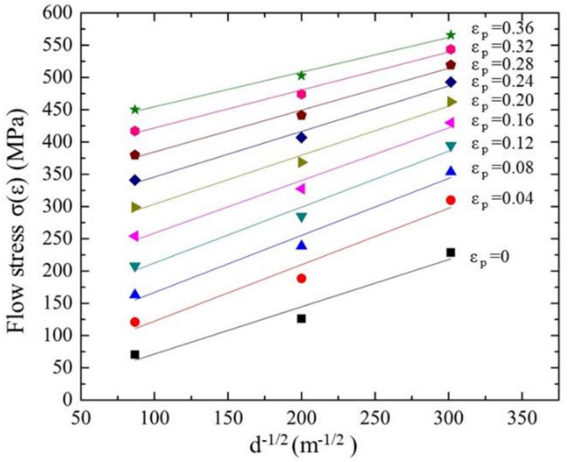

Fig. 3.2 Flow stress and grain sizes in the form of the Hall-Petch relationship of brass CuZn35.

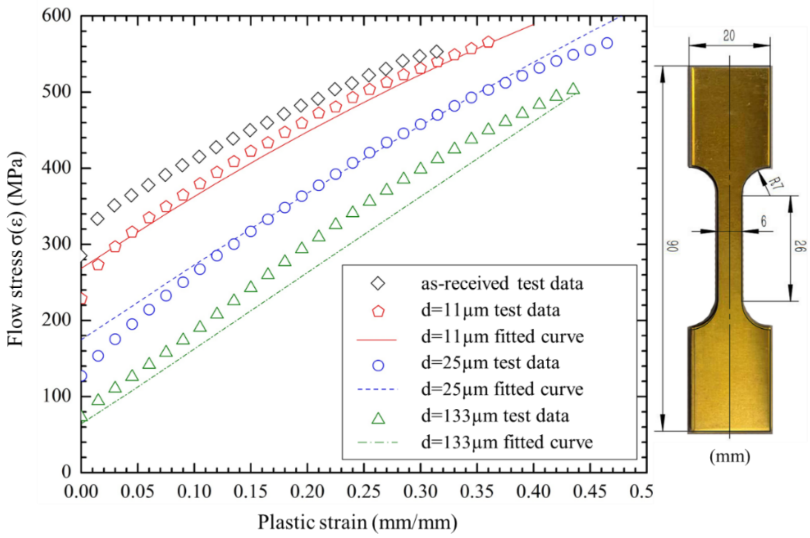

Fig. 3.3 The fitted and experimental flow stress with various grain sizes of brass CuZn35.

3.3 Materials and experiment

3.3.1 Experimental materials

Brass CuZn35 was selected as the test material due to its wide application in manufacturing pogo-pins and other electronic components for its excellent conductivity and good formability. The brass sheets with a width of 20 mm and a thickness of 2.0 mm were annealed in different temperatures and holding times under an argon-filled furnace to obtain different grain sizes and microstructures, viz. 450℃ for 1 hour, 550℃ for 1 hour, 600℃ for 1 hour, and 750℃ for 1 hour, respectively. The solution of 5g $FeCl_3$, 85ml H_2O, and 15ml HCl was used as etchant after polishing for etching the cross-section of specimens. The material microstructures along the thickness direction of the specimen under different heat treatment conditions are illustrated in **Fig. 3.4** (a). The grain sizes were measured based on the lineal intercept procedure of ASTM E112 standard as shown in **Table 3.1**. The design tolerance and final measurement of progressive tooling are illustrated in **Table 3.2**. The punches and dies are aligned by four guider pins crossing the punch holder, blank holder, and die holder. The punches and dies are positioned on the holders by transition fit.

Table 3.1 Annealing condition and the corresponding grain sizes.

Temperature (℃)	450	550	600	750
Grain size (μm)	22±4	39±1	71±11	107±15

Table 3.2 Dimension and tolerance specification of progressive tooling.

Dimensions (mm)		Tail-designed		Flat-designed	
		Step 1	Step 2	Step 1	Step 2
Punch	Design tolerance	2±0.1	$1.2^{-0.01}_{-0.1}$	2±0.1	$1.2^{-0.01}_{-0.1}$
	Measurement	2.052	1.188	2.145	1.194

Die	Design tolerance	\	$1.2^{+0.1}_{+0}$	\	$1.2^{+0.1}_{+0}$
	Measurement	\	1.230	\	1.230

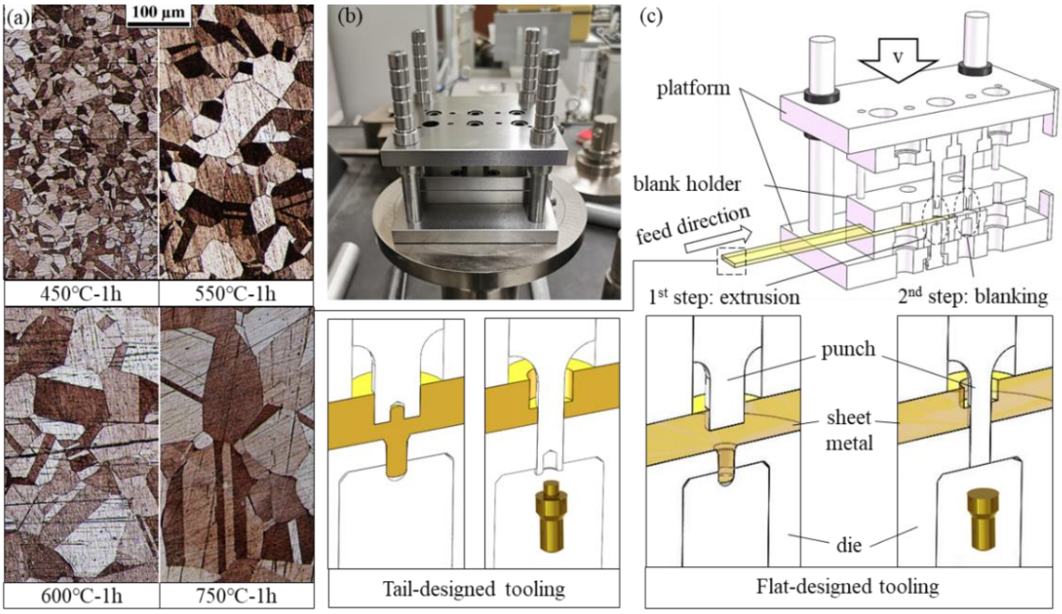

Fig. 3.4 (a) Initial microstructures of brass sheets with different grain sizes; (b) The photo of progressive forming system; (c) The progressive forming system and steps for two designs.

3.3.2 Development of progressive microforming process

Two structures of plunger parts are prepared to be formed and the dimensions of these two designs are shown in **Fig. 3.5**. The flat-designed plunger part is the basic design with a simple shape and formability, but it may shake in the lateral direction. The tail-designed plunger part is one of the improved designs to deal with this problem with good stability. Referring to the commercial product (Mill-Max Mfg. Corp.), the tolerances of assembly are ±0.15 mm on lengths in total and ±0.051 mm on diameters. Thus, for the individual part, the lengthwise tolerance of the head feature is set as ±0.075 mm, and it of the others are not required since they do not affect the total length of assemblies. The diametral tolerance of head and body features is ±0.051 mm. In addition, the surface finish on the plunger part requires 0.5 μm gold over nicker coating. In the related study [96], the electrodeposited coating thickness is decreased with the increase of surface roughness of the substrate, and to obtain a desirable coating quality, substrate R_a below 0.4 μm should be employed. The progressive forming system for producing the two plunger parts is illustrated in **Fig. 3.4** (c). The difference of tooling in design is that the punch for the tail-designed plunger is with an anti-drilled hole on the tip. This progressive microforming system includes two forming steps, viz., extrusion and blanking. In the first step, the material was extruded into the cavity of punch and die. In the next step, the preformed corner connected to the sheet was used for positioning, and the blank holder was employed to avoid the vertical motion of the sheet. After a shearing operation, the plunger part was ejected from the brass sheet. A plunger part was formed and blanked out with a single stroke, and then followed by the release of the blanking holder. The brass sheet was moved forward along the feed direction by one step length. After that, the blank holder was screwed, and the next progressive forming process started. The whole progressive forming process was conducted on an MTS testing machine with a maximum load capacity of 50 kN. Machine oil was used as the lubricant on each interface among punch, die, and specimen in both forming steps. The slow punch velocity of 0.01 mm/s was applied so the strain rate effect could be neglected. The brass sheet after forming and the fabricated microparts are shown in **Fig. 3.6**.

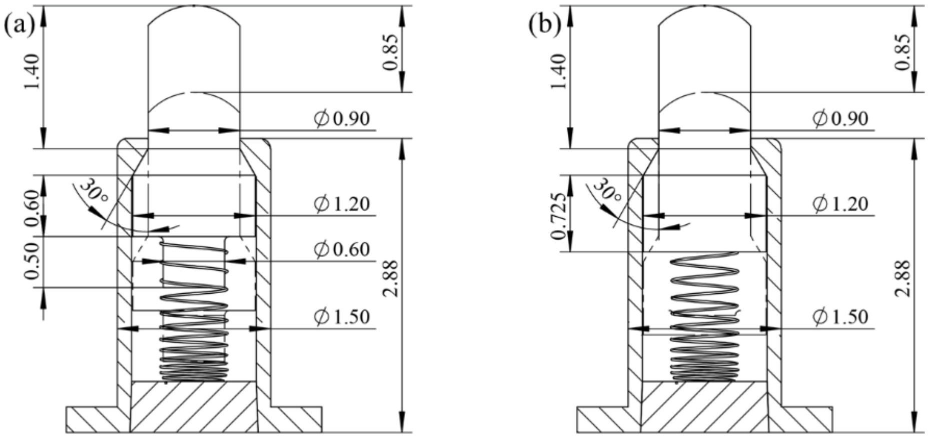

Fig. 3.5 The dimensions (in mm) of (a) tail-designed and (b) flat-designed pogo-pin assembly.

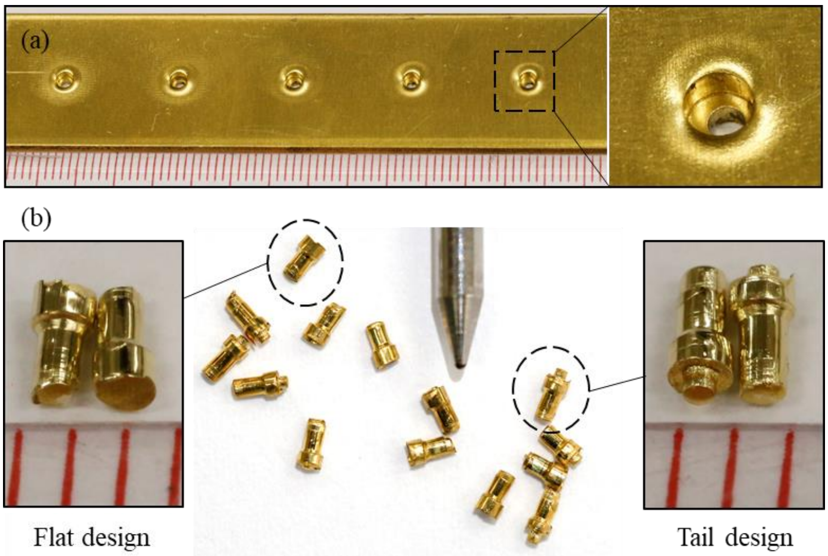

Fig. 3.6 (a) Sheet metal after forming; (b) The fabricated plunger parts.

3.4 Results and discussion

3.4.1 Load-stroke relationship

In microforming process, grain size is one key parameter that influences forming load and stroke, and further affects dimensional accuracy and morphologies of the final parts. The load-stroke relationships with various grain sizes in the forming process of tail-designed plunger scenario and flat-designed plunger scenario are shown in **Figs.**

3.7 and **3.8**. The entire forming process in each single stroke of punch is divided into three stages based on the individual progressive microforming operations of blanking and extrusion. Stage I starts from the blanking punch contacting material and ends by fracture, as the illustration of stage I inserted in figures. The material is subjected to shearing deformation and the preformed plunger part is then rejected from the brass sheet. It is shown that the ultimate shearing load is decreased with the increasing grain size, which is induced by the reduction of grain boundaries strengthening effects. In the next stage, the forming load shows a stable stage until the extrusion punch contact material. The load in this stage is mainly caused by interfacial friction between tooling and material. Stage III reflects the procedure of extrusion operation, where the material is extruded to preform the head and shoulder features by forward extrusion and the tail feature by backward extrusion. as the illustration of stage III inserted in figures. From the load-stroke curves, there is no obvious difference found between these two scenarios. A maximum force limit of the testing machine was settled to control the stroke of the upper die in the extrusion operation. When the load exceeds the maximum limit, the vertical stroke is stopped, and one progressive forming process is finished. The maximum limit values were calculated by finite element simulation so that the maximum force of 8000N was set as the upper limit of the tail-designed scenario while the load of 9500N was applied for the flat-designed scenario. The diagrams show that the maximum stroke is increased with grain size, which is contributed to the decreasing material strength. The grain size effect on the load-stroke behaviors is related to the characteristic of grain boundary, which acts as a barrier to slip transition. Therefore, when the specimen size keeps steady and the grain size increases, the fraction of grain boundary is reduced, which means the forming load is decreased.

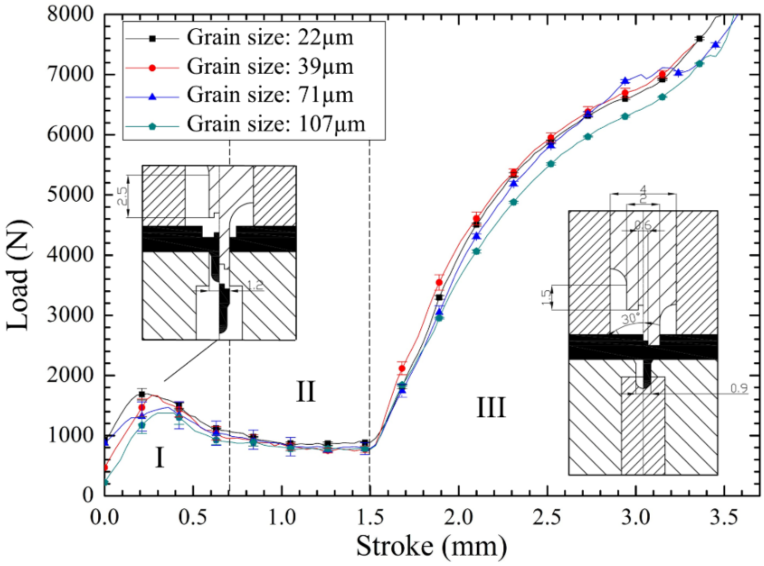

Fig. 3.7 Load-stroke curves with various grain sizes and tail-designed tooling.

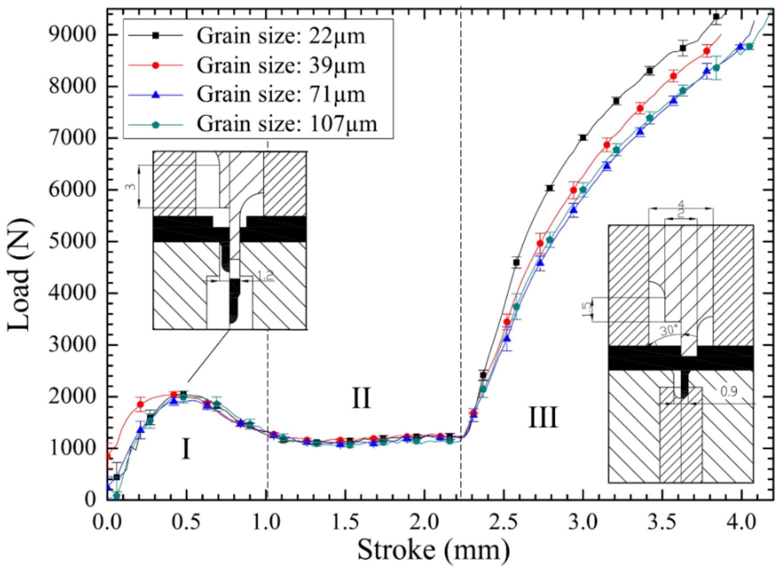

Fig. 3.8 Load-stroke curves with various grain sizes and flat-designed tooling.

3.4.2 Dimensional accuracy

Dimensional accuracy of the final parts is one of the key factors to be considered in progressive microforming as it can fully represent the outcome of part design, tooling development, and process variable configuration. It is generally affected by tooling manufacturing accuracy, forming operation design, material properties, and the variation of process variables. Compared to macroforming, microforming shows more and severely undesirable phenomena due to its small size scale, worse friction condition, and inhomogeneous deformation. To determine the grain size effect on the dimensional accuracy of micro-pin shaped parts, the progressive formed plunger part is characterized by four distinct features, viz. head, shoulder, body, and tail, and their lengths are represented by parameters H_1 to H_4, respectively, to clearly elucidate the change of the feature dimensions. The diameters of each feature are also represented by D_1 as body, D_2 as head, and D_3 as tail. However, microforming is a near-net-shape technology, so the subsequent processing is necessary to further improve the dimensional accuracy. Investigation of the dimensional variation of micro-formed parts guides the design of subsequent processing and the estimation of machining allowances.

The lengths and diameters of each feature with tail-designed and flat-designed parts with various grain sizes are summarized in **Figs. 3.9** and **3.10.** It is shown that the length of the head feature is slightly diminished in tail-designed parts, varying from 1.478 to 1.397 mm, and almost meet the tolerance requirement (±0.075 mm). But it is decreased from approximate 1.4 mm to 1.2 mm for flat-designed parts and slightly increased with grain size, which means the flat-designed parts hardly meet the desirable tolerance. In contrast to the length, the diameters of each feature in two designs do not change a lot and all of them meet the designed diametral tolerance (±0.051 mm), since it is well constrained by tooling dimensions. Moreover, the length of body feature drops obviously with the increase of grain size for both two designs, which is attributed to the coarse grain induced the increase of lateral material flow and the reduction of length of extrudate in sheet forming. The length of body feature is easier to meet the designed dimension since it is directly related to the punch stroke.

When there are only several grains in the sheet in the thickness direction, the inhomogeneity of grains is increased and thus more materials flow in the unfavorable direction out of the punching direction, so that less material remains in the original metal sheet after extrusion operation. In addition, the length of the shoulder feature keeps almost constant since this feature is formed in the middle and is fully constrained by the die. Conversely, for the tail-designed parts, the length of the tail feature is increased with the growth of grain size, which is the result of the decreasing grain boundary strengthening effect. In prior studies [97], the grain boundary blocks the slip transferring so that the grain boundary has higher dislocation density and hardness. Thus, the coarse-grained material with fewer grain boundaries is softer and easier to be extruded backward. Another factor to be considered is interfacial friction. Geiger et al. [2] and Engel et al. [25] reported that in forward-rod-backward extrusion, the macro-sized coarse-grained specimen tends to flow backward rather than forward compared to fine-grained material due to the friction, but the grain size effect disappears when the billet is scaled down to micro size since the backward flow is limited when the clearance between punch and die is in the order of grain size. In this study, the grain size related friction remains but not significantly since the diameter of tail feature is 600μm much bigger than the coarse grain size of 107μm.

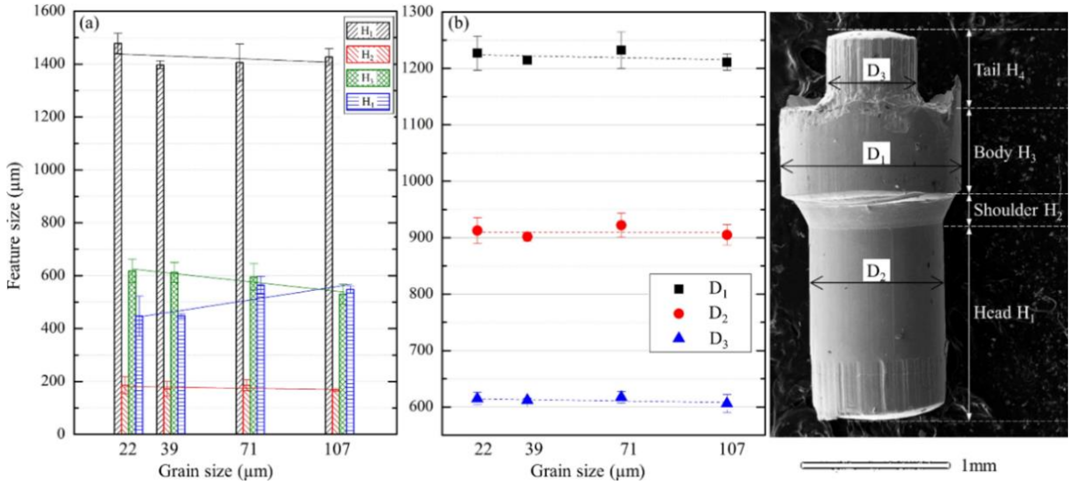

Fig. 3.9 Lengths and diameters of features for tail-designed part with different grain sizes.

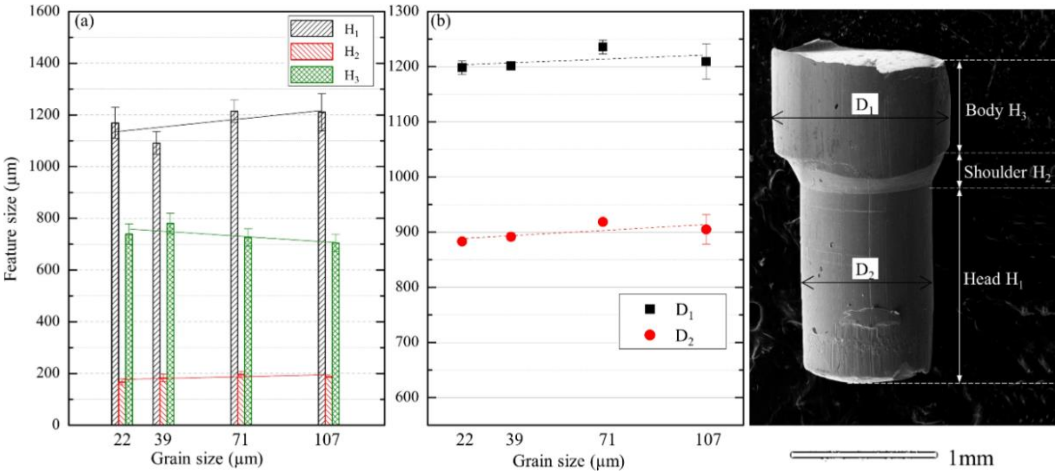

Fig. 3.10 Lengths and diameters of features for flat-designed part with different grain sizes.

3.4.3 Material flow behaviors

The material flow pattern in progressive microforming is related to the formation of dead metal zones and shear bands. Understanding the material flow behaviors is important for the optimization of the progressive forming process and the properties of the microformed parts. Numerical simulation combined with experiments was employed to study the mechanism of shear band formation. The friction factor was 0.12 for the interface of mateiral and tooling. Quad-dominated mesh was used. The blank holder and die were fixed, and the punch moved down with 0.01 mm/s as the physical experiments. To investigate the mechanism of the formation of shear bands, the contour and vector maps of material flow with the grain size of 22 and 71 μm in extrusion operation are illustrated in **Fig. 3.11**. When the punch stroke is equal to 1.38 mm, there are three zones in sheet metal based on the gradient of velocity showing the change of material flow velocity. Zone I appears near the inner hole profile of punch; Zone II is from the lower edge of the conical surface of die to the middle; Zone III appears on the area connected outer profile of punch to the upper edge of the conical surface of die. The velocity gradient in Zone I is lower than that in the other two zones. However, when stroke=0.74mm, which is the initial stage of the extrusion operation, Zones II and III can still be observed but Zone I is not clear and even disappear for the fine-grained material. It is revealed that the shear band on Zone I is formed later than Zones I and III during the extrusion. Focusing on the flow vectors, there is a critical Zone IV that appears on Zone III, where the stream of material flow is divided into two directions, viz. longitudinal and lateral. With the movement of punch, the variations of the direction and magnitude of flow velocity in the critical Zone IV is significant and a new critical Zone V is formed near Zone II, where the velocity shows an obvious increase and only longitudinal flow remains, which is induced by the reduction of the diameter of die orifice.

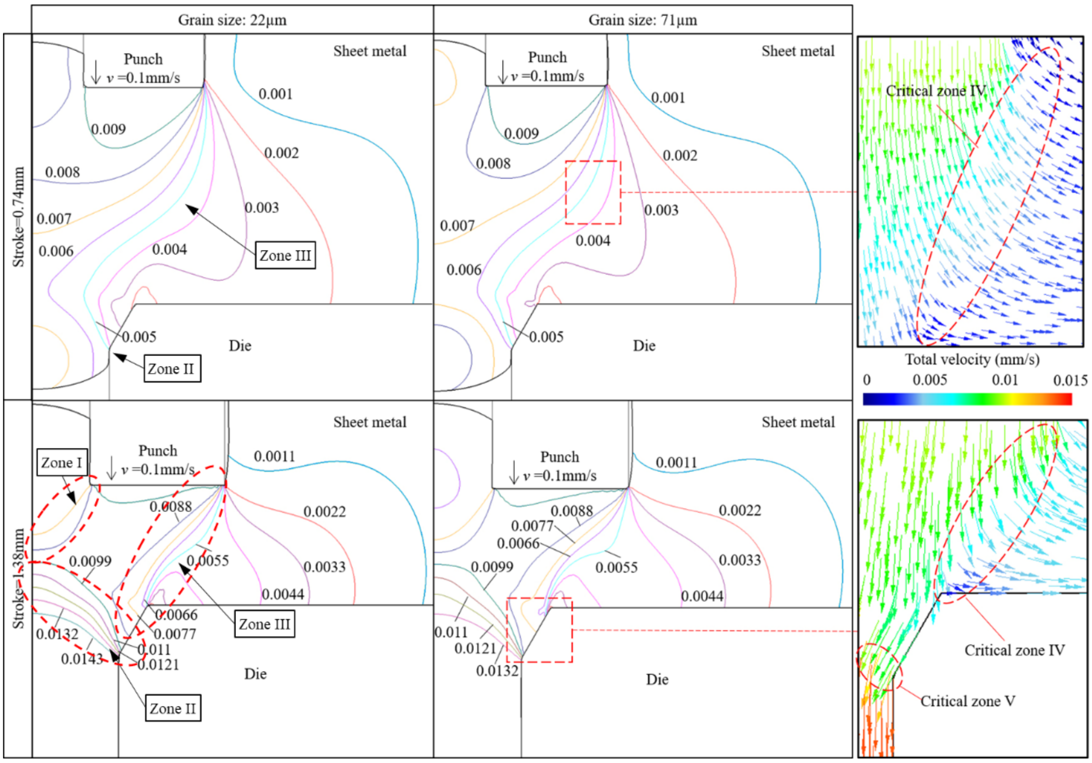

Fig. 3.11 Material flows (contour and vector) under different strokes and grain sizes.

Compared to **Fig. 3.13**, the microstructures on cross-sections along the symmetric axis of the final tail-designed microparts using the fine-grained material (grain size=22μm) and coarse-grained one (grain size=71μm) observed by metallographic microscopes, it is revealed that the shear bands are located in Zones I and II. The effective strain distribution shows the formation of shear band I clearly but it of shear band II is not. According to **Fig. 3.12**, the shear band III induced by Zone III can be found along the corners of punch and die, which is coherent with the effective strain distribution. It is concluded that the shear band prefers to be formed in the area with a large gradient of flow velocity and area with effective strain accumulation. The shear band I in **Fig. 3.13** shows a decreasing width than shear band II. Therefore, it can be inferred that the higher gradient of velocity results in a wider shear band. But the variation is not coherent with effective strain distribution. Moreover, the friction-induced shear band in **Fig. 3.13** was not illustrated by velocity change, but it is precisely calculated by effective strain distribution. In addition, on both sides of the body feature, two shearing zones are formed due to the blanking operation, which in numerical result shows the highest strain accumulation. The grains in the shear band are significantly elongated and distorted along the direction of material flow. From the comparison of different grain-sized material, it is shown that the width of shear band increases with the growth of grain size since a large number of grains are involved in material deformation to share the rotation and elongation at a specific strain, so coarser grains contribute to the larger area of shear band.

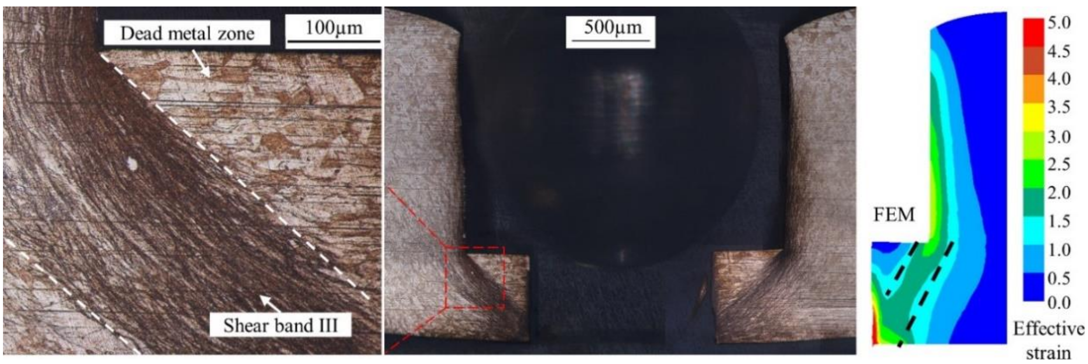

Fig. 3.12 Microstructures of the cross-section of sheet metal after progressive forming and the FEM result.

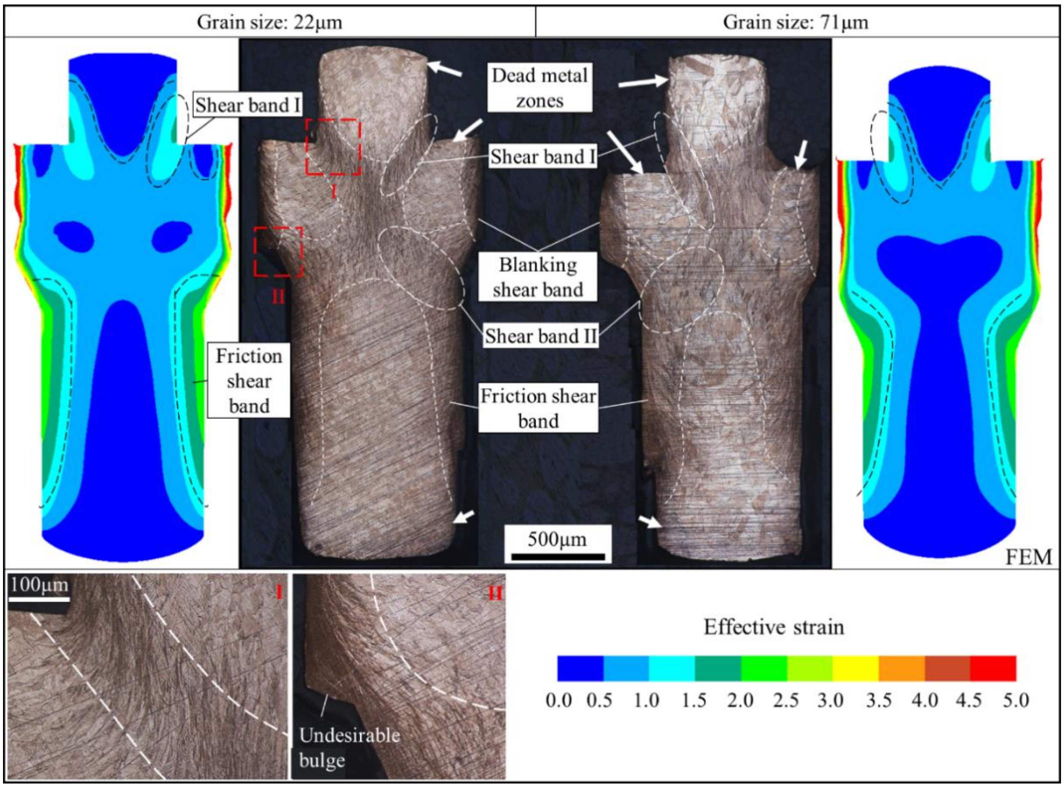

Fig. 3.13 Microstructures of the cross-section and FEM results of the tail-designed parts with grain sizes of 22 and 71 μm. (I) Grains in shear band I; and (II) an undesirable bulge.

Dead metal zone (DMZ) is defined as the place where no or almost no material flow. Preliminary studies [98-101] of DMZ based on hardness measurement and flow lines distribution in the etched micrographs showed that the deformation zone morphology is dependent on die geometry, friction, workpiece material, extrusion ratio and loading rate. As shown in **Fig. 3.13**, three DMZs are recognized with clear boundaries based on the deformation degree of grains and flow lines. One dead metal zone appears on the top of the tail feature with the shape of half-round. Two other dead metal zones occur near the top profile of the body feature and they are symmetric with a central line. The formation of DMZ is consistent with the fact that DMZ is easily formed underneath the flat indentor in punching, and influenced by the backward extrusion and friction in this scenario, of which the material near the edge of hole is largely deformed and the shear bands are then formed in between the DMZs. In addition, a less deformed zone is formed in the head feature, which is similar to DMZ with negligible straining. In **Fig. 3.12**, the microstructure of brass sheet after blanking, two DMZs near the vertical surface of punch and die are shown. **Fig. 3.14** presents the microstructural evolution of the flat-designed plunger part. The shear band I disappears and the DMZs are connected. For the coarse-grained material, the shear bands are elongated to the central area. It is verified that the area of the shear band is increased with grain size. The formation of the shear band is coherent with effective strain distribution.

In summary, shear bands prefer to be formed in the area with a high gradient of material flow velocity or with effective strain accumulation. In addition, the wider shear band is reflected by a higher gradient of flow velocity but not obviously in the effective strain distribution.

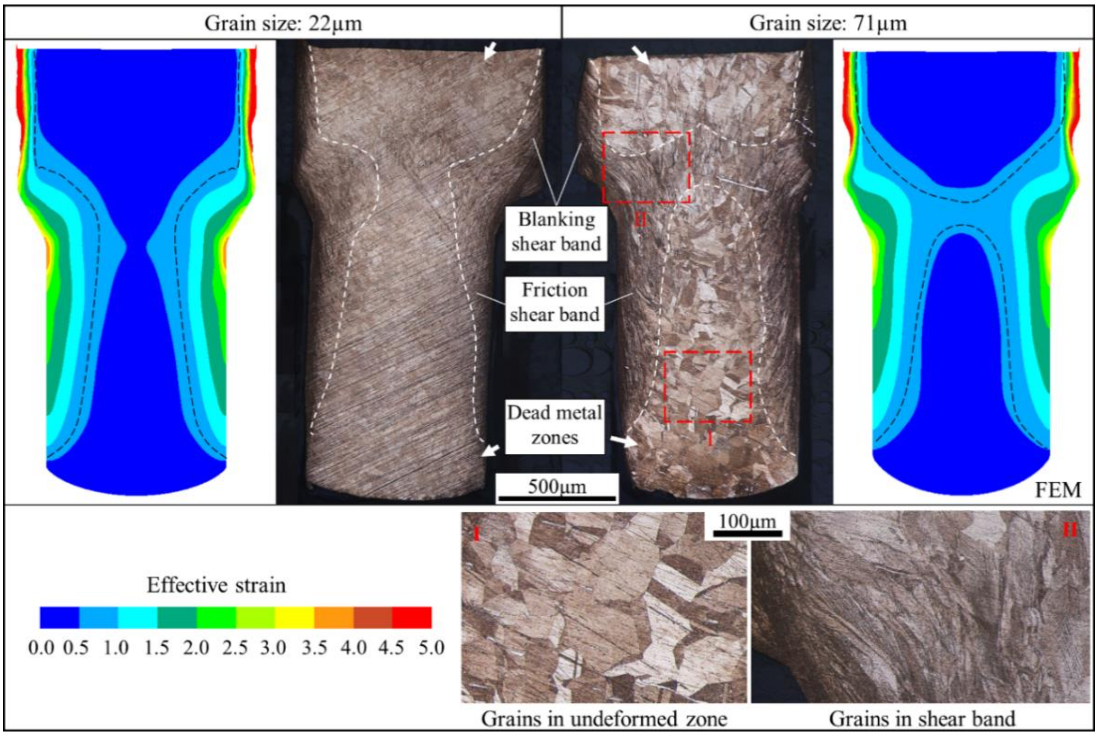

Fig. 3.14 Microstructures of the cross-section and FEM results of the tail-designed plunger part with the grain size of 22 and 71 μm. The grains in (I) the shear band, and (II) the undeformed zone.

3.4.4 Undesirable geometries

The major undesirable geometry in this progressively microformed part is the deviation of concentricity between the head feature and body feature. As the microstructural images shown in **Figs. 3.13** and **3.14**, an undesirable bulge on the side profile appears due to this reason, and the opposite side is thicker. The factor attributing these undesirable geometries is the assembling precision of tooling, interfacial friction, material unfilling, and the springback of material after extrusion. For the design aspect, the corner is designed for positioning but could cause a deviation in the next blanking operation for positioning. Compared with prior researches [12], the corner-based positioning method is not as accurate as of the hole-based positioning method. The outer cylindrical surface could be considered for positions in future research.

3.4.5 Surface fracture

The ductile fracture induced by plastic deformation reaching a certain limit is easier to happen in progressive forming. The morphologies of micro plunger parts in the tail-designed scenario with different grain sizes were observed by Scanning Electron Microscope (SEM) and symmetrically studied. **Figs. 3.15–3.17** illustrate the geometrical shape and defects of the microparts with different grain sizes observed by SEM. As shown in **Fig. 3.15** (a), **Fig. 3.16** (a), and **Fig. 3.17** (f), microcracks appear on the edge between tail feature and body feature in all grain sizes, which could be induced by sharp deformation angle and die corner. As prior studies revealed, the sharp corner of die easily causes damage accumulation [102]. Secondary, the top surface of body feature shows an uneven morphology, and some micro pits are found on the top surface in **Fig. 3.15** (g, h), **Fig. 3.16** (c), and **Fig. 3.17** (f), which is similar to the phenomena on the large deformed conical surface of the progressively microformed part [12].

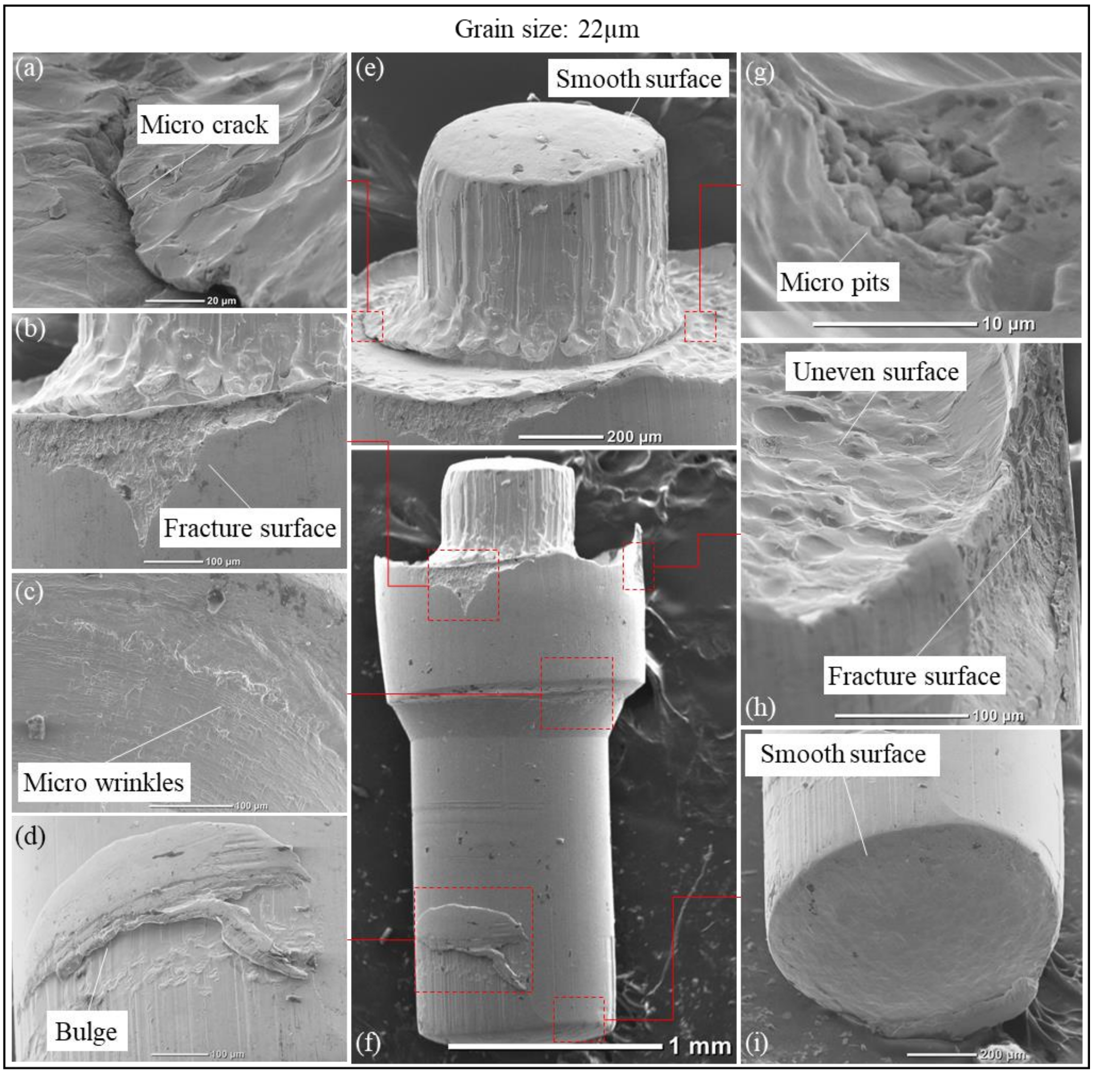

Fig. 3.15 SEM pictures of the tail-designed plunger part with the grain size of 22μm.

Moreover, wrinkles occur on the conical surface of shoulder feature, as shown in **Fig. 3.15** (c), where the material flow direction is thirty degrees to the stroke direction. However, micro pits are formed on the largely deformed surface in the prior study [12], but on the surface of DMZ in this study. Thus, the forming mechanism of micro pits maybe not so related to the material strain but related to the material flow direction along punch stroke. When the material flow differs from punch stroke, the fluctuation away from the desirable material flow direction is easy to occur, which leads to the formation of wrinkles, micro pits and uneven surfaces, and the coarse-grained material causes more undesirable geometries. On the other hand, fracture surface and burr appear at the area near the upper edge of body feature and shows randomness, as shown in **Fig. 3.15** (b, h) and **Fig. 3.16** (b), which is a common undesirable geometry appearing after blanking operation [12, 28]. The initiating, growing, and coalescing of microvoids result in the rough surface and bad surface finish. In addition, as shown in **Fig. 3.15** (e), **Fig. 3.16** (c) and **Fig. 3.17** (c), the lateral surface of tail feature shows the conspicuous longitudinal surface texture since this surface is backward extruded against the stroke direction. Compared with the micropart with fine grains, the longitudinal textures on the extrusion surface show a slight decrease, which could be caused by the decrease of hardness with the larger grains.

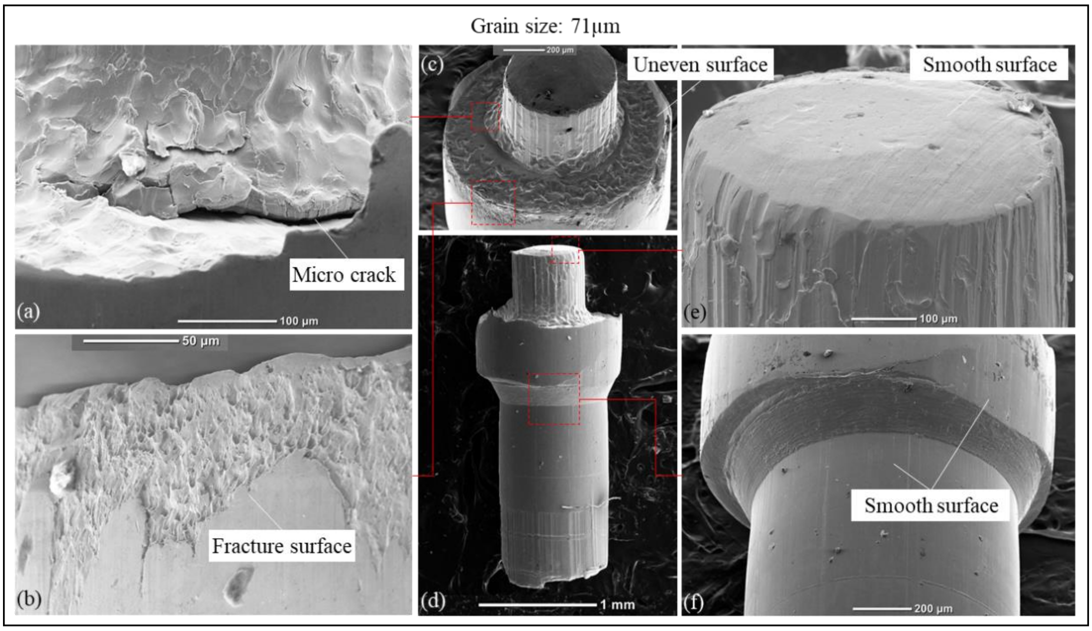

Fig. 3.16 SEM pictures of the tail-designed plunger part with the grain size of 71μm.

Conversely, a smooth surface appears on the profile of head feature as illustrated in **Fig. 3.15** (e, f, i) and **Fig. 3.16** (e, f) since this surface is forwardly extruded to form in parallel to the stroke direction. The surface of body feature is also smooth except for the fracture surface. The desirable smooth surface of head feature facilitates the function of the contact with the barrel of pogo-pins. In addition, the end surface of tail and head features are also smooth since no lateral material flow happens on these two surfaces. The wrinkle or bulge appears near the boundary of two parts of die due to the unperfect contact, as shown in **Fig. 3.15** (d) and **Fig. 3.17** (b).

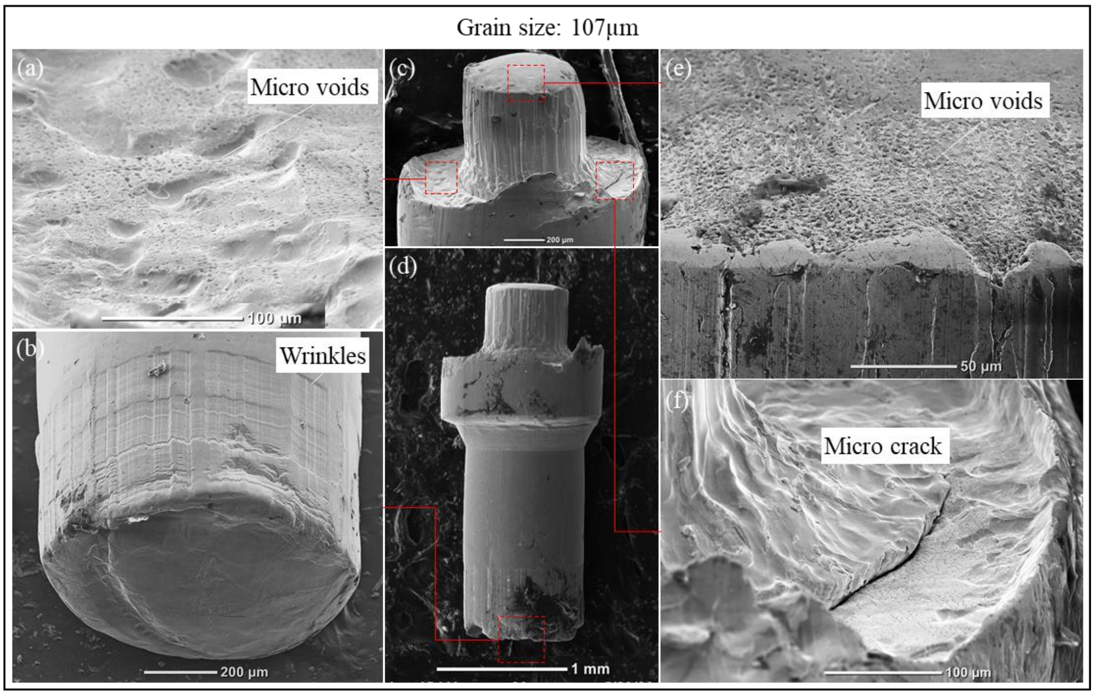

Fig. 3.17 SEM pictures of the tail-designed plunger part with the grain size of 107μm.

On the other hand, microvoids are observed on the top surface of body feature and the end surface of the tail feature with the coarse-grained material, as shown in **Fig. 3.17** (a, e), but there are no such voids with fine grains. The occurrence of the voids could be caused by the fact of increasing inhomogeneous deformation in the inherited grains with the larger grain size. This undesirable defect could significantly worsen the performance and durability of the contact surface. It can be predicted that the critical value of grain size that promotes the formation of microvoids falls between 71 to 107 μm.

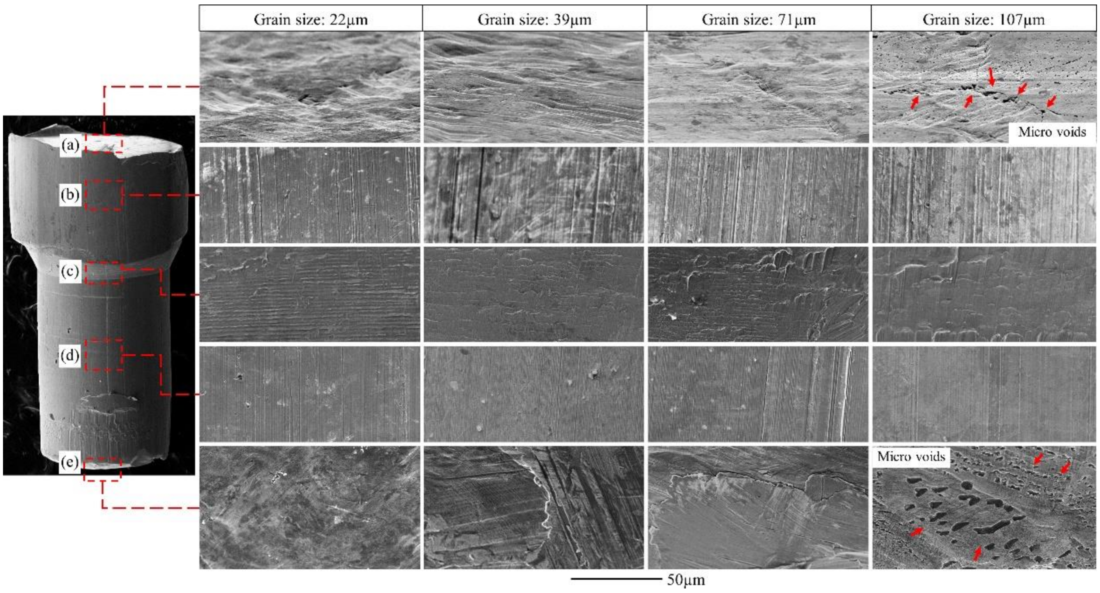

Fig. 3.18 Morphologies of the surfaces with different grain sizes of the flat-designed part. (a) top-body, (b) side-body, (c) shoulder, (d) side-head and (e) end of head surface.

Fig. 3.18 illustrates the variation of surface quality of the top-body, side-body, shoulder, side-head, and the end of the head surface with grain size from 22 to 107 μm of the flat-designed parts. The side-body, shoulder, and side-head surfaces show a desirable quality, which is not changed a lot with grain size, especially for the side-head surface, which is contacted by the barrel for current flow and requires high wear resistance. However, the top-body surface and the end of the head surface are uneven and get worse with the increase of grain size, and with the grain size of 107 μm, voids and crack appear, as illustrated in **Fig. 3.18** (a, e). The qualities of these two surfaces do not meet the required surface finish, and the subsequent processing such as grinding or polishing process is thus needed to improve the surface quality for the subsequent coating.

In summary, for both two designs, the important side-head surface shows a desirable surface quality, and the wrinkle and bulge can be avoided by a modified die. The end surface of head contact with PCBs in the service environment, so it requires a smooth quality for the coating to resist abrasion, therefore, the fine-grained material with a subsequent grinding is preferred. The side-body and shoulder surface show an acceptable quality, but the blanking-induced fracture surface should be avoided. Although the side-tail, top-tail, and top-body surfaces show undesirable unevenness and texture, they are not the contacted surface, so the forming quality is acceptable. The crack on the edge between the tail and body feature of the tail-designed parts should be eliminated, which may cause breakage.

3.4.6 Surface finish

The surface roughness *Ra* is an important factor that can influence the subsequent coating process for the electronic and wear-resistance requirements of the plunger parts. To quantitively study the qualities of side surfaces, the surface roughness *Ra* at the side surface of tail, body and head features of the tail-designed plunger parts are illustrated in **Fig. 3.19** measured by 3D laser scanning microscope (Keyence VK-X200). As shown in the diagram, the roughness at the side surface of tail is around 1.0 to 1.4 μm, which is over the roughness requirement, and it shows a rising trend with the increase of grain size. On the other hand, the roughness at the side-head and the side-body surface displays a smoother surface where the roughness is about 0.7 μm of the body and 0.58 μm of the head, and it keeps steady with the change of grain size. Since the same surface on flat-designed plunger parts is formed by the same process, the surface roughness is still referable for the other design. As discussed in the above section, the important side surface of the head almost reaches the roughness requirement (*Ra*=0.4 μm). Therefore, an improved die with a high-quality surface finish is required. Moreover, the roughness at the side surface of the body and tail is acceptable, and the fine-grained material should be preferred.

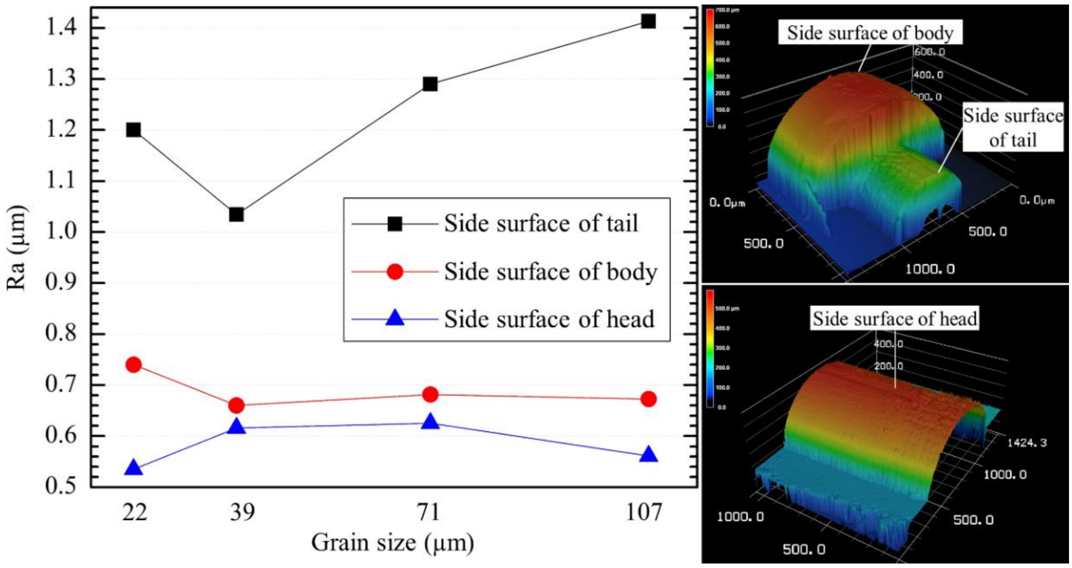

Fig. 3.19 The surface roughness at the side surfaces of tail-designed plunger parts.

3.5 Summary

A progressive forming system was developed for the fabrication of pin-shaped plunger parts with two design scenarios by directly using sheet metal to replace the traditional micro-machining process. The micro-formed parts were symmetrically investigated from the aspects of microstructural evolution, dimensional accuracy, surface fractures, and the deformation load in forming process considering grain size effect. The following conclusions are thus drawn from this research:

1) The progressive microforming system directly using sheet metals was developed with extrusion and blanking operation, and two types of punch design were employed for different designs of pogo-pin. The forming system can fabricate the plunger part with a single punch stroke, which is an efficient process to produce complex pin-shaped microparts with the potential for mass production.

2) With the increase of grain size, the deformation load is decreased, and the punch stroke moves forward. In addition, the height of body feature is decreased, the height of head feature is slightly decreased for the tail-designed part and increased

for the flat-designed part, the height of tail feature is increased, and the height of shoulder feature keeps steady with the increase of material grain size. The diameters of each feature are not changed much and meet the design well. The feature lengths are within the tolerance except for the head length of the flat-designed plunger part.

3) The shear band prefers to be formed in the area with a higher gradient of material flow velocity and effective strain accumulation. In addition, the higher gradient of flow velocity and coarse grains result in a wider shear band formed. DMZs are formed underneath the punch and become small with the coarse-grained material.

4) Strain accumulation induced microcracks, inhomogeneous deformation-induced micro pits, uneven surface, and micro wrinkles, backward material flow-induced longitudinal surface texture, and unperfect tooling assembling induced bulges and wrinkles are observed as the undesirable defects on the surfaces of microparts. For the grain size of 107 μm, microvoids appear on all the flat surfaces. The side-body, shoulder, and tail surfaces show acceptable quality. The roughness of the side-head surface almost meets the requirement.

5) To realize the desirable progressive microforming of the plunger part of pogo-pins, the corner radius of punch and fine-grained material should be considered. Attention should be much paid to assembly precision in such a way as to reduce undesirable defects.

For the progressively formed tail-designed pin-shaped microparts with fine-grained brass, their dimensions meet the required accuracy. The side surface of head is close to the ideal roughness. The forming qualities on other surfaces are acceptable except for the end surface of head feature, which requires subsequent grinding or polishing. However, the length of head of flat-designed microparts does not meet the tolerance requirement. Therefore, the tail-designed plunger micropart is suggested to be formed by progressive microforming with fine-grained materials.

Chapter 4 Compound microforming of bulk parts by directly using sheet metals

4.1 Introduction

Meso-/micro-manufacturing technologies for making various meso-/micro-parts and structures have been extensively developed and advanced in the last few decades to meet the increasing demands of product miniaturization in different industrial fields [45]. The traditional meso-/micro-manufacturing technologies including meso-/micro-machining [4, 94], meso-/micro-EDM [103], photolithography [104], and laser machining have capabilities to fabricate meso-/micro-parts or structures with high precision and desirable qualities, but they have different limitations and application niches. Meso/microforming has become a promising process for mass production due to its high productivity and efficiency, less material waste, net-shape or near-net-shape characteristics, and economic and environmentally friendly production [56-58]. Therein sheet-based bulk or sheet forming shows high efficiency in material feeding and positioning. To solve the troubles in handling, transporting, and ejection in different forming processes, the concept of progressive and compound forming of sheet metals was proposed. This unique process aims at making complex-structures or multi-feature parts by directly using sheet metals. The term “progressive” means that the process chain with two or more single forming steps involved and progressive dies are employed. Each step in the process chain has its designed stroke and predefined task, so that several forming steps can be conducted progressively with an excellent efficiency [12]. The term “compound”, however, is to combine several types of deformations into one single stroke rather than one deformation in conventional forming, such as the realization of blanking and extrusion together in one stroke.

Although numerous studies on meso/microforming and size effects were conducted, there is a lack of an in-depth investigation on size effects in the compound meso/microforming and the sheet-based bulk meso/microforming. Since the plug-shaped part is a typical shape of bulk parts and a common and popular shape in complex meso-/micro-products, it was thus selected as a case study. In this study, a compound microforming system including micro-blanking and micro-heading operations was developed to fabricate micro-plug parts using sheet metals, and the influence of grain size and blanking clearance on the micro blanking-heading process and the quality of the formed parts were comprehensively studied in terms of deformation load, burr formation, dimensional precision, material flow behavior, hardness distribution, surface defects formation, and geometrical profile variation. The crystal plasticity simulation was conducted to compare with the homogeneous-property-based simulation to evaluate the surface radius variation. The results show that the higher grain size and thicker punch-die clearance reduce the deformation load, worsen the material loss, and decrease the bulge diameter. The material flow behavior was discussed based on the hardness test and the microstructural evolution with numerical results. The radius variation of the heading feature was predicted well by the crystal plasticity model. Surface defects including sunken area, crack, surface damage, and pits were observed, and their formation and elimination are discussed. All these findings in this study thus enrich the understanding of blanking-heading compound meso/microforming and sheet-based bulk meso/microforming and enhance the knowledge in this area to support and promote the application of this efficient micro-manufacturing process.

4.2 Experimental details and simulation setup

4.2.1 Testing materials and mechanical properties

T1 pure copper (Cu≥99.95%) was selected as the testing material in this study due to its excellent formability and other good mechanical properties. Pure copper sheets (20×90 mm) with a thickness of 2 mm were annealed under different heat treatment conditions and then cooled down to room temperature gradually in an argon-filled furnace to obtain diverse grain sizes. The microstructures of pure copper along the thickness direction after annealing are illustrated in **Fig. 4.1**, and their annealing conditions and corresponding grain sizes are shown in **Table 4.1**. The cross-section of the specimen was cut, ground, polished, and then etched by a solution of 5 g $FeCl_3$, 85 ml H_2O, and 15 ml HCl. The grain sizes were measured based on the linear intercept method of the ASTM E112 standard.

Table 4.1 Annealing conditions and the related grain sizes of pure copper.

Temperature (°C)	500	750	800	950
Holding time (hrs)	2	2	3	3
Grain size (μm)	17 ± 2	67 ± 3	90 ± 8	303 ± 7

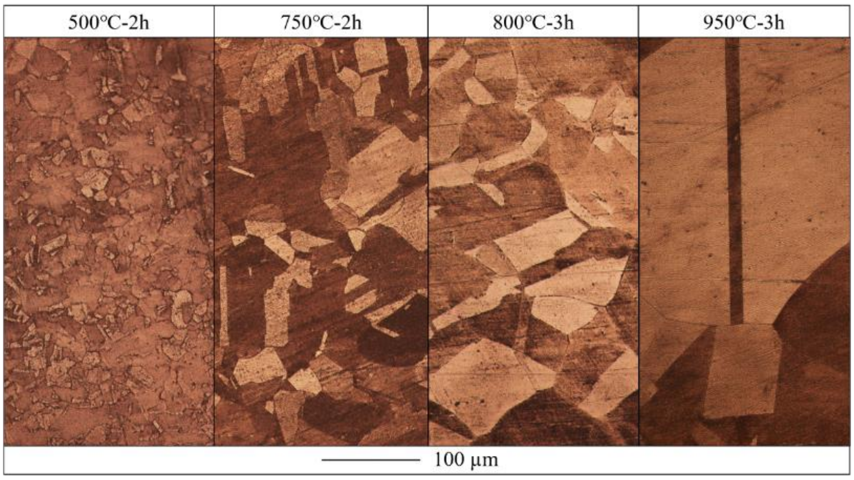

Fig. 4.1 Microstructures of pure copper under different annealing conditions.

To quantitatively analyze the mechanical response of the test material, micro-cylindrical specimens were cut from the pure copper sheets by EDM to conduct uniaxial compression tests. The specimens were 1.2 mm in diameter and 2 mm in height. Lubricant grease was used to reduce friction. A strain rate of 0.002 s^{-1} was employed for quasi-static deformation. Each group of the experiment was repeated four times. The generated true stress versus true strain curves are illustrated in **Fig. 4.2** (a). It is revealed that the flow stress is decreased with the increase of grain size. As shown in **Fig. 4.2** (b), the flow stress of the test material follows the Hall-Petch relation well at the strain less than 0.4, indicating the linear relation between stress and the inverse square root of grain size [37]. For the polycrystal model, the extended Hall-Petch relation [105] is widely applied to describe the flow stress in the following:

$$\bar{\sigma}(\bar{\varepsilon}) = \sigma_0(\bar{\varepsilon}) + k(\bar{\varepsilon}) \cdot d^{-\frac{1}{2}} \tag{4.1}$$

where $\bar{\sigma}$ is flow stress, $\bar{\varepsilon}$ is effective strain, σ_0 and k are constants for a given $\bar{\varepsilon}$, and d is grain size. The experimental data was used in the homogeneous-property-based simulation.

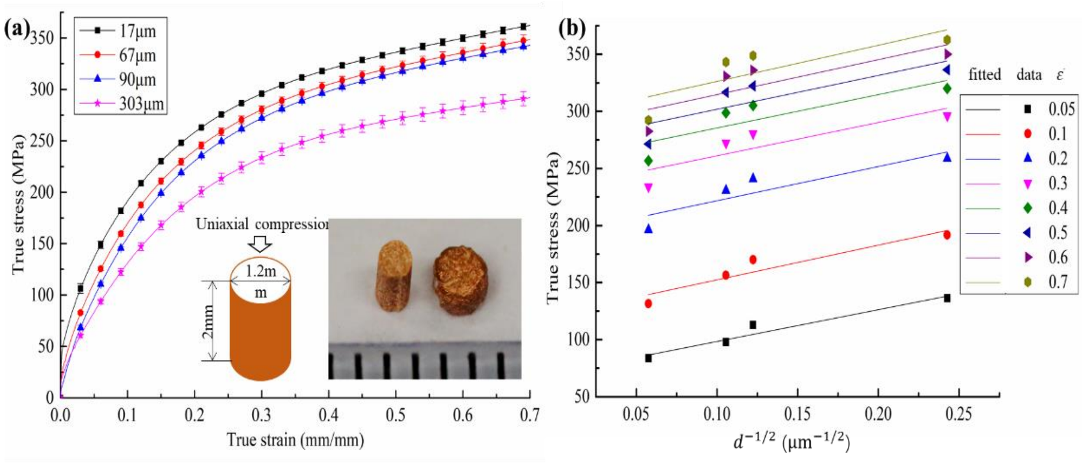

Fig. 4.2 (a) Stress-strain curves of the pure copper with different grain sizes; (b) Hall-Petch relation.

4.2.2 CPFEM Simulation

The heading-formed feature is a freeform geometry, and the homogeneity-based conventional model cannot predict the cylindricity of the physical parts. Thus, the grain-based CPFEM is selected for simulation. The constitutive model of CPFEM is illustrated in *Section 2.5.4*. The parameters of pure copper in this study are presented in **Table 4.2**. In addition, the elastic tensor constants for pure copper are C_{11} = 168.4 GPa, C_{12} = 121.4 GPa, and C_{44} = 75.4 GPa, respectively [106].

Table 4.2 Parameters for pure copper [90] in this study.

$\boldsymbol{\tau_0}$(MPa)	$\boldsymbol{\tau_s}$(MPa)	$\boldsymbol{h_0}$(MPa)	$\boldsymbol{\dot{\gamma}_0(s^{-1})}$	$\boldsymbol{m}$	$\boldsymbol{a}$	$\boldsymbol{q}$
16	148	180	0.001	0.012	2.25	1.4

In the CPFEM simulation, the quarter-cylindrical parts with the height of 2 mm and the radius of 0.6 mm were fixed on X and Y directions with symmetrical constraints and then compressed by 60% in the Z direction in Abaqus/Explicit environment. C3D4 elements were employed in the meshing process and a modified VUMAT subroutine [107, 108] was employed. It was assumed that the grain size and shape of the geometrical model were similar to a quarter of the experimental sample and the torsion and the normal displacement on the symmetrical planes of grains were zero. This approach is slightly different from the actual situation, but the difference is reflected by the individual crystals on symmetrical planes. The entire mechanical responses are neutralized to some extent. The polycrystal model was randomly generated by software Neper [109] using the controlled Voronoi method with various grain shapes and the average grain size of 303 μm so there were 38 grains in one model. Three repeated simulations with different initial grain orientations were conducted. The stress-strain curve for the grain size of 303 μm obtained from the simulation was compared with the relative experimental data and it is illustrated in **Fig. 4.3**. The true stress was measured from the applied force divided by the immediate area, and the true strain was calculated from the total accumulative shear strain. The error bars reflected the deviation among different repeated simulations, where the maximum standard error was 13.4 MPa. The flow stress in CPFEM simulation meets well with the experimental data obtained from uniaxial compression tests when the strain is less than 0.35. The difference over 0.35 was induced by the formation of the non-circular shape of specimen at large strain and the interfacial friction in uniaxial compression. It may also be deviated by the properties of material obtained from references, which may have a slight difference from the real ones of the material used in this research.

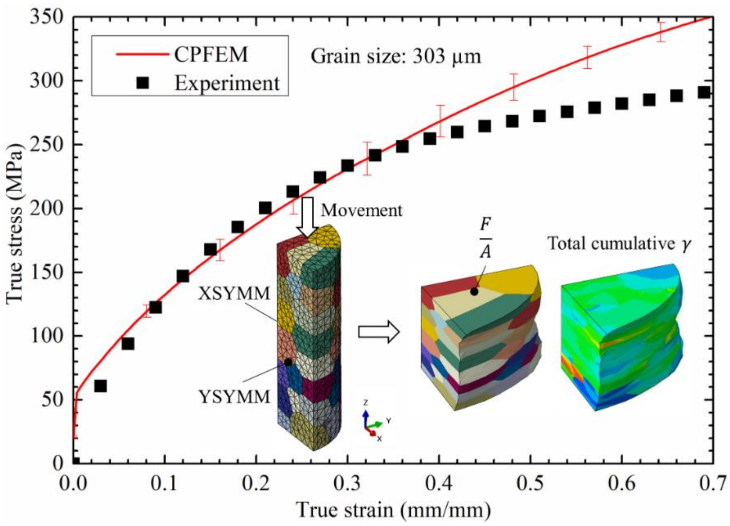

Fig. 4.3 Stress-strain curves of CPFEM and experimental data with the grain size of 303 μm.

4.2.3 Micro plug part and compound microforming system

The design of the micro plug part and the compound microforming system is shown in **Fig. 4.4**. The compound microforming system was installed between the upper and lower platforms equipped on an MTS testing machine with a 50kN maximum capacity load cell. Punches of different diameters were employed in the compound forming process to study the geometrical size effect of punch-die clearance. The punch-die clearances in each case are presented in **Table 4.3**, which are measured by the diameters of punch and die. They are average values since the concentricity is unperfect. Thus, all the experiments are repeated 4 times to eliminate the effect of concentricity. Pure copper sheets with different initial grain sizes were used as specimen to study the grain size effect in the compound forming process. In the beginning, the specimen was inserted into the slot between the blank holder and die holder, and the blank holder was tightened to avoid shaking during the forming process. Then the compound forming process started. The material underwent shearing deformation during the blanking stage, and a micro-cylindrical part was cut from the specimen at the end of this stage. With the continuous movement of punch, the heading stage began. The trimmed cylindrical part was compressed to fill the die cavity, where the extrusion deformation occurred. The desirable geometry was formed at the end of this stage. Then the insert die was released, and the formed part was ejected. The specimen was fed forward, and a new forming process began. Machine oil was used as lubricant on the interface between material and tooling to minimize friction. The punching speed was 0.01 mm/s, so the effect of strain rate could be neglected.

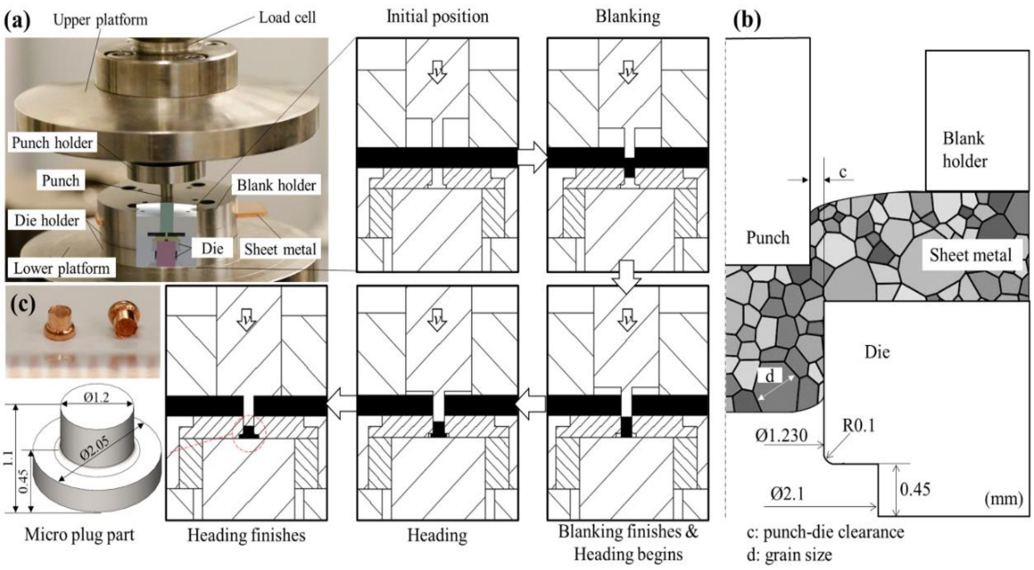

Fig. 4.4 (a) The compound microforming system and the forming steps; (b) The dimensions of dies; (c) The micro plug parts.

Table 4.3 Punch-die clearances of different punches.

	Case 1	Case 2	Case 3
Punch diameter (mm)	1.192	1.140	1.090
Die diameter (mm)		1.230	
Clearance on each side (μm)	19	45	70

4.3 Results and discussion

4.3.1 Load-stroke relationship

Punching and blanking are both shearing operations, which are different in producing cylindrical parts or holes. The shearing operation is divided into three stages, viz., the rising elastoplastic stage, the static shearing deformation stage, and the dropping fracture stage [13]. The results in **Fig. 4.5** (a–c) are consistent with the prior studies on the grain size effect in meso-/micro-punching or blanking [12-14, 110], in which the punching load/pressure is decreased with the increase of grain size, since the barrier-like characteristic of grain boundaries during shearing deformation is weakened with the increase of grain size. **Fig. 4.5** (d) shows the effect of punch-die clearance (c) on the forming load in micropunching/blanking process. The forming load is increased with the decrease of clearance, which agrees with the prior arts [111, 112].

In addition, the ultimate shear stress (σ_s) is introduced as $\sigma_s = F_{max}/\pi dl$, where F_{max}, d, l are the maximum blanking load, the punch diameter, and the length of the blanked surface, respectively. Xu et al. [110] indicated the clearance/grain size ratio (c/d) and clearance/thickness ratio (c/t) are two main factors influencing the deformation behaviors in micro-punching/blanking. When c/d = 1, the ultimate sharing strength reaches a maximum value. In this study, as shown in **Fig. 4.6**, the ultimate shear stress is still mainly affected by the punch-die clearance, and it is increased with the latter. This is because the material involved in the shearing deformation has a dominative effect on shearing stress. On the other hand, the ratio of punch-die clearance to grain size is shown in **Table 4.4**. When the punch-die clearance is 19 μm, the ultimate shear stress reaches the maximum value with $c/d \approx 1$; while for the other two clearances, the increasing slope gets mild when $c/d > 1$. It is thus speculated a maximum value appears at $c/d = 1$, but it is influenced by the complicated force and friction conditions. When $c/d > 1$, grains are evenly distributed in the lateral and thickness directions and their main deformation behavior in shearing is the coordinating deformation of grains. With the increase of grain size, the coordinating deformation of grains becomes difficult. The grain boundary sliding and the rotation of individual grains show obvious effects, which facilitates the increase of the ultimate shear stress. Conversely, when $c/d < 1$, which means the grain size is larger than the punch-die clearance so that the grain distributions in the lateral direction at the clearance region generally change within a single crystalline structure, but the grain size still has an effect along the thickness direction. Thus, the number of grains along the thickness direction is important. The more grains involved in deformation, the higher c/d ratio, the more grain boundaries hinder the deformation along the thickness direction, thereby enhancing the ultimate shear stress. Therefore, when $c/d = 1$, the ultimate shear stress should reach the maximum value according to these two deformation mechanisms.

In addition to the blanking operation, transition and heading stages are determined based on the load-stroke curves presented in **Fig. 4.5**. The transition stage starts after the blanking operation and ends before the heading begins. The load in this stage is mainly caused by the friction of the micro-cylindrical part sliding in the die central hole and the punch sliding in the pierced hold of specimen. Moreover, the curves in heading start with a small peak (the first heading stage), then rise quickly in a parabolic shape (the second heading stage), and they then roar rapidly when the punch reaches the designed stroke limitation. In the first heading stage, the material is subjected to an elastic-plastic deformation and slightly bulged. In the second heading stage, plastic deformation is facilitated effectively. Grain size effect is not significant in this stage. However, as shown in **Fig. 4.5** (d), punch-die clearance (c) greatly affects the load and stroke in this stage, where the forming load in the second heading stage is increased with smaller punch-die clearance. The geometrical size effect is induced by the different volumes of cylindrical parts after blanking, where the larger punch-die clearance results in a shorter and thinner blanked cylinder. Its deformation in the heading stage is thus decreased relatively, and a lower forming load is generated.

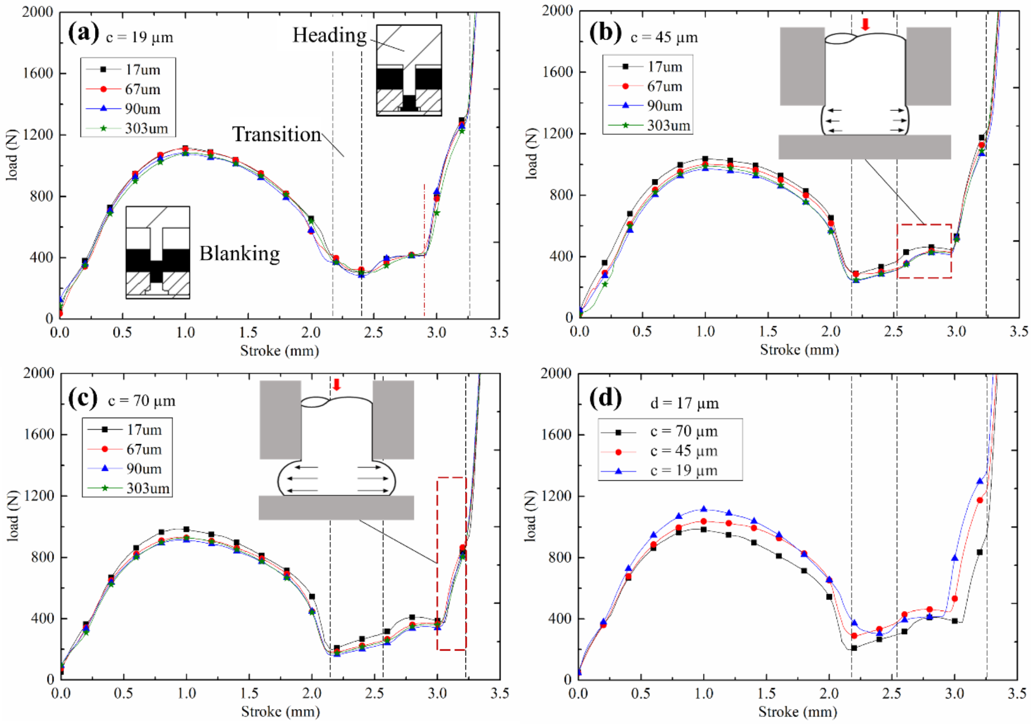

Fig. 4.5 Load-stroke curves with different punch-die clearances of (a) 19 μm, (b) 45 μm and (c) 70 μm, and (d) load-stroke curves with the specific grain size of 17 μm.

Table 4.4 Clearance to grain size ratio (c/d) of each case

c/d (μm/μm)		Punch-die clearance (c)		
		19	45	70
Grain size (d)	17	1.118	2.647	4.118
	67	0.284	0.672	1.045
	90	0.211	0.500	0.778
	303	0.063	0.149	0.231

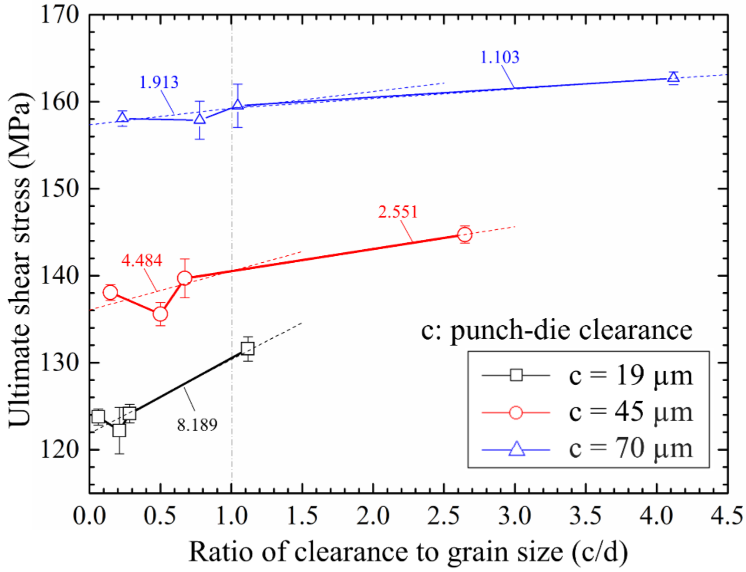

Fig. 4.6 Ultimate shear stress in blanking stage with different c/d ratios. The slopes of curves are shown in different colors.

4.3.2 *Microstructural evolution*

The microstructural evolution of microparts includes the formation of shear bands and the remaining dead metal zone (DMZ). DMZ is defined as a zone that has no or almost no material flow, and its formation is related to the geometry of die, interfacial properties and loading rate [14, 99, 101, 102]. Understanding the microstructural evolution is important to predict the mechanical properties of the final parts and the material flow behavior during the forming process. The DMZs are identified based on hardness measurements and the flowline distribution of the cross-section of the etched micrographs. In this work, the microstructural evolution is studied in detail from experimental hardness tests and the numerical simulation of strain distribution. The results from two aspects are discussed to reveal the material flow behavior in this compound microforming.

Hardness distribution

The material strengthening phenomenon results from the generation and movement of dislocations within the crystal structure and grain boundary sliding of materials. The Vickers hardness test on the cross-section of the formed parts was conducted to evaluate the work hardening accumulation during the compound microforming process. The test results are shown in **Fig. 4.7**. As given in **Fig. 4.7** (a), the original hardness of the fine-grained materials (17 μm) is slightly higher than that of other materials. From the variation of hardness on cross-section in **Fig. 4.7** (b–e), it is found that the higher hardness appears near the lateral profile of the cylindrical feature and it is induced by the shearing deformation in the blanking operation. The hardness near the corner of the heading-formed feature drops slightly and reduces obviously at the widest tip. Conversely, the central area at the top of parts has the lowest hardness and this value drops as grain size increases. Along the symmetrical line downward, there are two peaks of hardness, which indicates two separate shear bands. The first one is on the mid-upper area elongating from the center to the lateral profile; while the other is located on the center of the bottom surface extending to the corner on profiles. For the very coarse-grained material (303 μm), however, the mid-upper shear band disappears, which is believed to be caused by less strain accumulation on the large grains. By the comparison among different grain sizes, it is revealed that the hardness in the undeformed area drops significantly and the hardness of the shear band is slightly decreased with the coarser grains, since the increasing number of grain boundaries enhances the work hardening effect. But the hardness on the cylindrical profile does not change much.

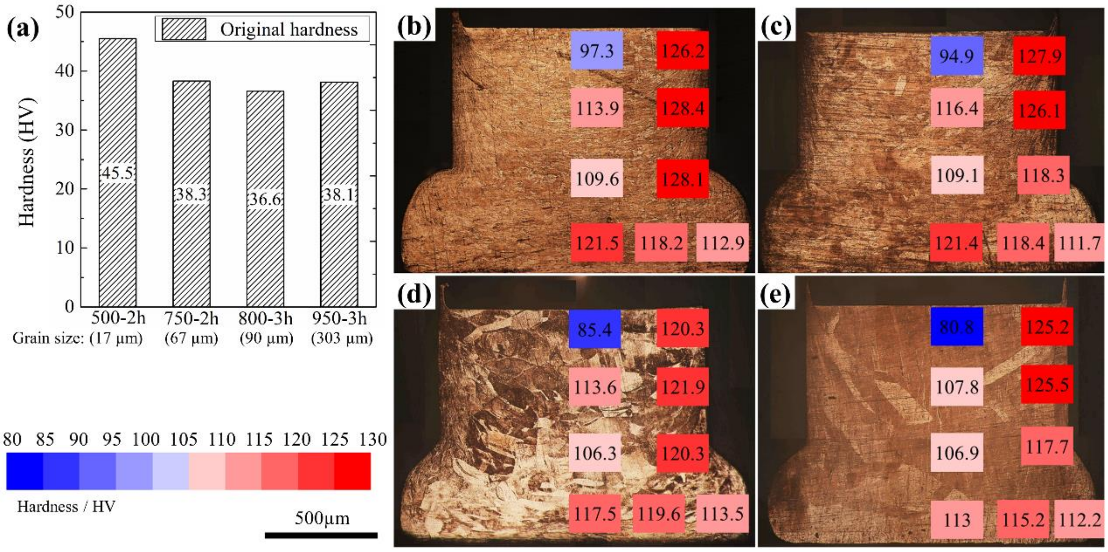

Fig. 4.7 (a) Initial hardness (HV) of the specimen, and the hardness on different areas of the cross-section of the formed parts with grain sizes of (b) 17 μm, (c) 67 μm, (d) 90 μm, and (e) 303 μm.

Strain distribution

Numerical simulations were conducted based on the flow stress model $\bar{\sigma} = f(\bar{\varepsilon}, d)$ using the uniaxial compressive test data in **Fig. 4.2** to study the formation of shear bands and DMZs. The conventional finite element simulation using DEFORM was applied considering its efficiency and applicability in the simulation of compound forming processes, and the boundary conditions based on the physical experiments were applied directly in simulation. The constant shear friction model ($f_s = mk$) with the friction factor of 0.12 on the lubricated tooling-workpiece interface was employed. The results are compared with the micrographs on the cross-section of the formed parts to study the influence of punch-die clearance, as illustrated in **Fig. 4.8**. As shown in **Fig. 4.8** (a–c), three shear bands, A, B, C, and three DMZs, X, Y, Z, are determined based on the microstructure analysis and the numerical simulations of the final parts with the grain size of 17 μm. When the punch-die clearance is the smallest (19 μm), as shown in **Fig. 4.8** (a), the boundary between adjacent zones is clearly determined. The grains in Zones X and Y are nearly undeformed. Zone X is formed just below the flat punch because there is little material flow underneath the flat punch. Grains in Zone Y are barely deformed during the micro-blanking operation, and the horizontal elongating in heading does not affect them. Zone Y is thus maintained after micro-heading. The arc-shaped shear band A is formed during the micro-blanking operation between Zones X and Y and extends to the shearing area. The material in shear band A is subjected to tensile stress in the horizontal direction. This stress transmits the punching loading to the punch-die edge to make the shearing deformation happen. The shape and height of Zone Y mainly depend on the shear bands A and B. In addition, shear band B is formed during the micro-heading operation, where the bottom material is compressed and protruded in the horizontal direction but hindered by the punching hole. The material deformation is thus concentrated near the corner and extends to the central bottom surface with a compressive force. The grains in shear bands A and B are severely elongated along the horizontal direction and extend to shear band C. Shear band C is formed due to the severe shearing deformation during the micro-blanking operation. Moreover, the simulation results indicate a small dead metal zone Z near the bottom edge of the final parts, attributed to the gradually decreasing horizontal strain along the X-direction from the central bottom surface to the edge during micro-heading. But this zone is not clearly shown on the microstructural graph.

With different punch-die clearances, the microstructural evolution and strain distribution are changed. In **Fig. 4.8** (b), the punch-die clearance is 45 μm and the area of Zone X is slightly increased. The grains in Zones A and C rotate and extend severely, as shown in the partial diagram in **Fig. 4.8** (i). In addition, the boundary on the micrograph between dead metal zone Y and shear band B is not clear. It can be seen that the horizontal elongation of grains gradually increases in the downward direction. The partial diagrams to present the grains in this region are shown in **Fig. 4.8** (ii) and (iii).

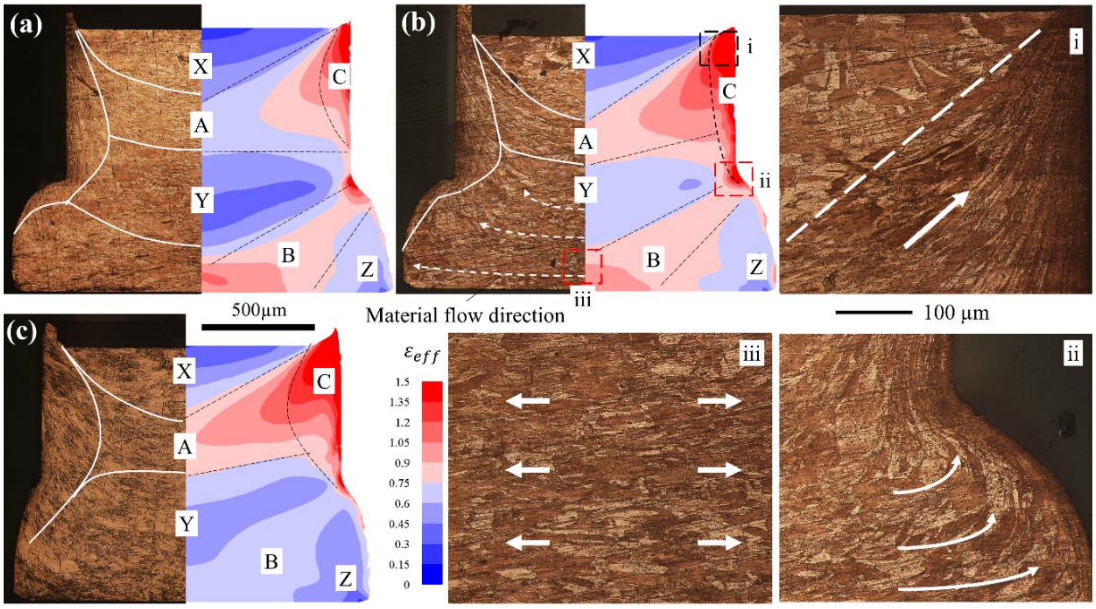

Fig. 4.8 Microstructures and effective strain on the cross-section with grain sizes of 17 μm and punch-die clearances of (a) 19 μm, (b) 45 μm and (c) 70 μm; partial view on (i) top edge, (ii) corner and (iii) central bottom.

Through applying the quarter-cylinder model, the distributions of effective stress and effective plastic strain determined by FEM and CPFEM simulations are shown in **Fig. 4.9**. As seen in **Fig. 4.9** (b), the stress and strain distributions of CPFEM are considering grain orientations, which are nonuniformly distributed. Conversely, FEM does not consider grain orientations. Therefore, the CPFEM results, which reflect the microstructure of the material and grain orientations, are more accurate than the simulations provided by the traditional FEM. Furthermore, since the material in CPFEM is assumed to be inhomogeneous, the maximum stress and strain at a certain area are determined.

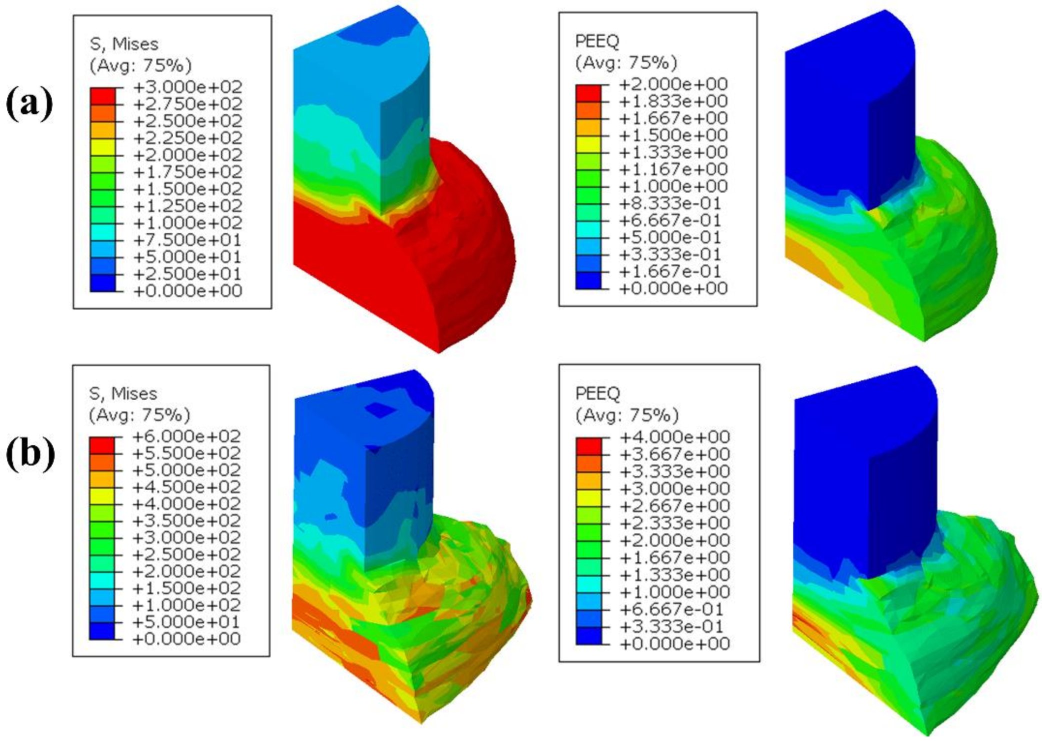

Fig. 4.9 Distribution of the effective stress and the effective plastic strain predicted by (a) FEM, and (b) CPFEM.

4.3.3 Geometrical precision

The geometrical precision of the final parts is important for evaluating the characteristics of microforming process. In this work, the burr formation and dimensional accuracy of micro-formed parts, and the material loss and radius variation during the compound microforming process are investigated.

Burr formation

Burr formation is generally induced by the punch-die clearance during punching/blanking process. To quantitatively study the variation of burr with different grain sizes and punch-die clearances, the comparison of burr height and burr width is shown in **Fig. 4.10**. In **Fig. 4.10** (b–d), the punch-die clearance is fixed, and the width of burr approximately equals the punch-die clearance. The grain size has no obvious influence on the burr width. In the diagrams presented in **Fig. 4.10** (e–h), the effect of punch-die clearance on burr formation for a given grain size is presented. The triangular areas in the diagram represent the volume of burr. It can be seen that the volume of burr is increased significantly with the punch-die clearance.

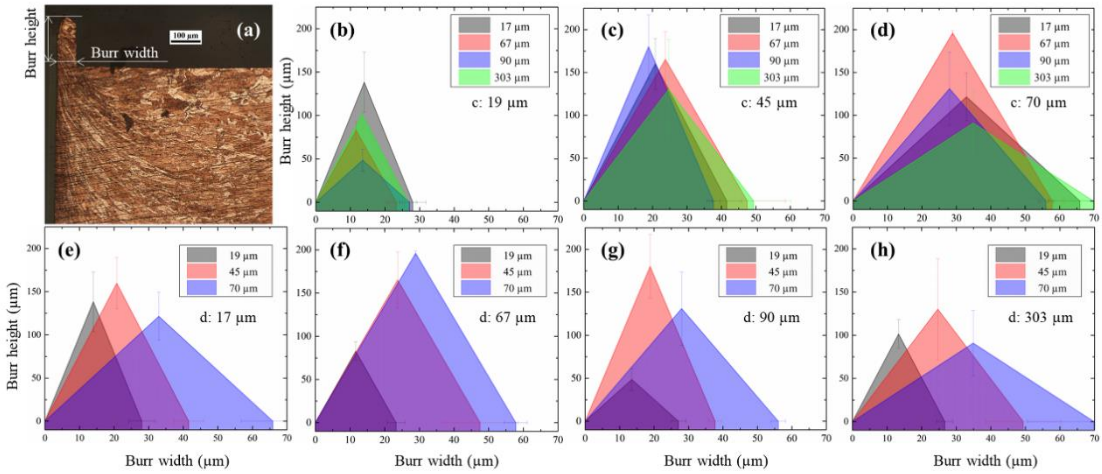

Fig. 4.10 (a) Burr illustration; the height and width of burrs at a specific punch-die clearance (b–d) and grain size (e–h).

In addition, to directly investigate the regularity of burr height, the relationship between the clearance to grain size ratio (c/d) and the burr height is illustrated in **Fig. 4.11**. It is revealed that when c/d ratio is around one with a given punch-die clearance, the longest burr is obtained. Meanwhile, the smaller punch-die clearance can slightly decrease the height of burr. With the smallest punch-die clearance (19 µm), the height of burr is greatly decreased. The burr formation mechanism is related to the occurrence of material ductile fracture. In macroscale, the ductile fracture happens via the mechanism of microvoids initiation, growth along stress direction, coalescence, and finally fracture. Since the microvoids are more possible to appear at grain boundaries, the number of grains in the deformed zone is important for fracture behavior. When $c/d > 1$, grains have a uniform distribution on the thickness and clearance directions, and the fracture mechanism is related to the quantities of grain boundaries and microvoids. Thus, the larger c/d ratio, the more grains involved in deformation, and the more microvoids initiate and grow. Therefore, ductile fracture happens earlier and results in shorter burrs. Conversely, when c/d < 1, a single grain occupies the clearance direction, and the fracture mechanism changes from the microvoid evolution to the dislocation within a single grain. With the growth of grain size, the number of grains and grain boundaries on the thickness direction is less. Thus, the dislocation is easier to extend since the grain boundary acts as a barrier to obstruct dislocation. All this leads to an earlier happening of ductile fracture. Therefore, when c/d = 1, the longest burr is obtained. However, due to the complicated interfacial conditions for burr formation including friction, surface roughness, etc, the regularity of burr height is generally not applicable among different sets of punch and die.

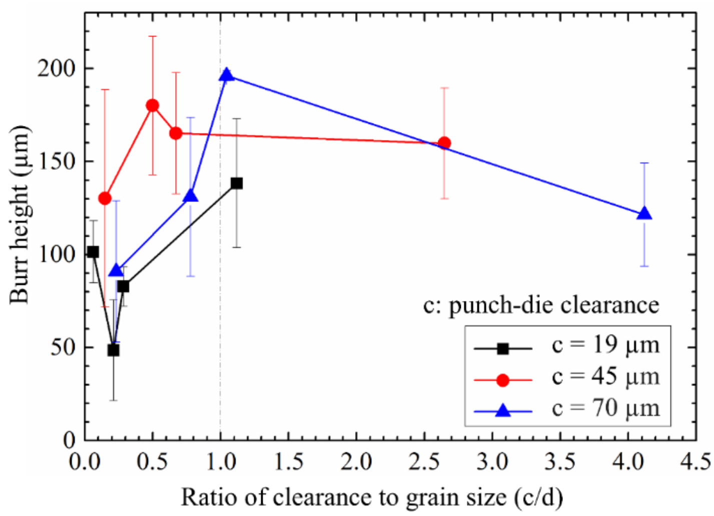

Fig. 4.11 Variation of burr height of the formed parts with different c/d ratios.

Undesirable material loss

In meso/microforming process, the material cannot always flow along the desired direction to form the designed geometries. The material flow always follows the principle of least resistance force, thus lateral flow always happens in punching/blanking process. It generally gets worse with the coarser grains. The material lateral flow and undesirable geometries formed in blanking such as burr, rollover and height shortage result in material loss. To quantitatively study and compare the material loss among different punch-die clearances and grain sizes in the compound forming, the shortage fraction is introduced, which is:

$$Shortage\ fraction = 1 - \frac{Effective\ volume}{Design\ volume} \tag{4.2}$$

where “effective volume” is the volume of the effective geometry, and “design volume” is the volume of the designed part. The variation of shortage fraction with different grain sizes and punch-die clearances is shown in **Fig. 4.12**. Due to the unavoidable height shortage, rollover, and burr formation after micro-blanking, the minimum value of the shortage fraction is 33%. It shows an increasing trend with the larger grain size since the lateral deformation is increased with the coarse-grained material. There is an obvious increase of the shortage fraction with a larger punch-die clearance since a larger punch-die clearance enhances the volume of burr and further reduces the effective volume.

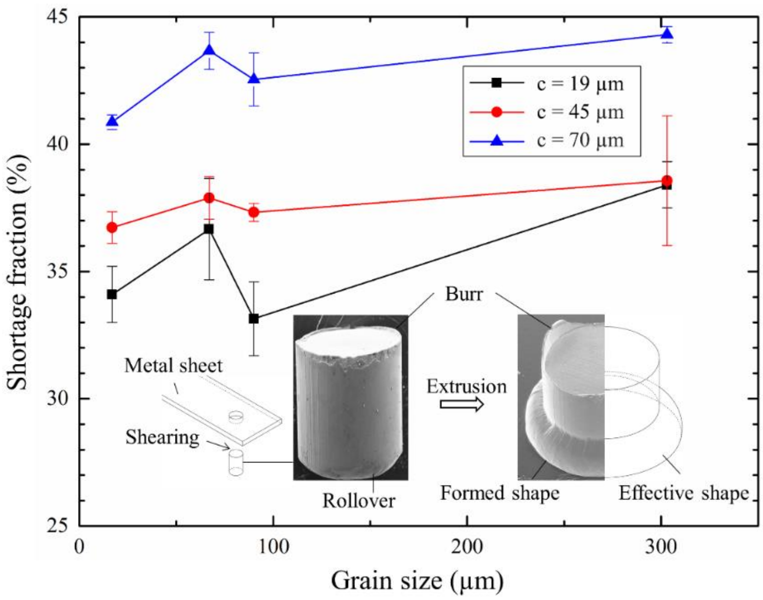

Fig. 4.12 Shortage fraction of the formed parts with different grain sizes and punch-die clearances after the compound forming process.

Dimensional accuracy

Investigation of dimensional accuracy of meso-/micro-formed parts helps improve metal-formed part design, tooling development, process, and process factor determination. Dimensional accuracy in meso/microforming is more serious than that in macroforming since there are severe undesirable geometries generated in a small scale. To quantitatively determine the grain and geometrical size effect, three critical dimensions of the micro plug parts are selected to represent the variation of dimensional accuracy with grain size and punch-die clearance, viz., the height of parts (H), the average diameter of the cylindrical feature (D1), and the largest diameter of the bulge feature (D2), as shown in **Fig. 4.13** (a). The measured results are illustrated in **Fig. 4.13** (c–e) and grouped by different punch-die clearances. From these figures, it can be seen that the punch-die clearance and grain size show little effect on H and D1 (vary less than 50 um). D2 shows a decreasing tendency with the increase of both grain size and punch-die clearance. **Fig. 4.13** (b) presents the variation of D2 with grain size and punch-die clearance. It can be seen that D2 is linearly decreased with the increasing grain size, and the intercept is also decreased with the increase of punch-die clearance. Since the orientation of individual grain significantly affects the material properties with the large grain size, the material is hard to flow along the desirable direction, resulting in the height shortage of the blanked cylinder [12] and the asymmetrical extrusion in the micro-heading process. In addition, the decrease of the effective volume of the blanked cylinder due to the large punch-die clearance is another reason for the reduction of D2.

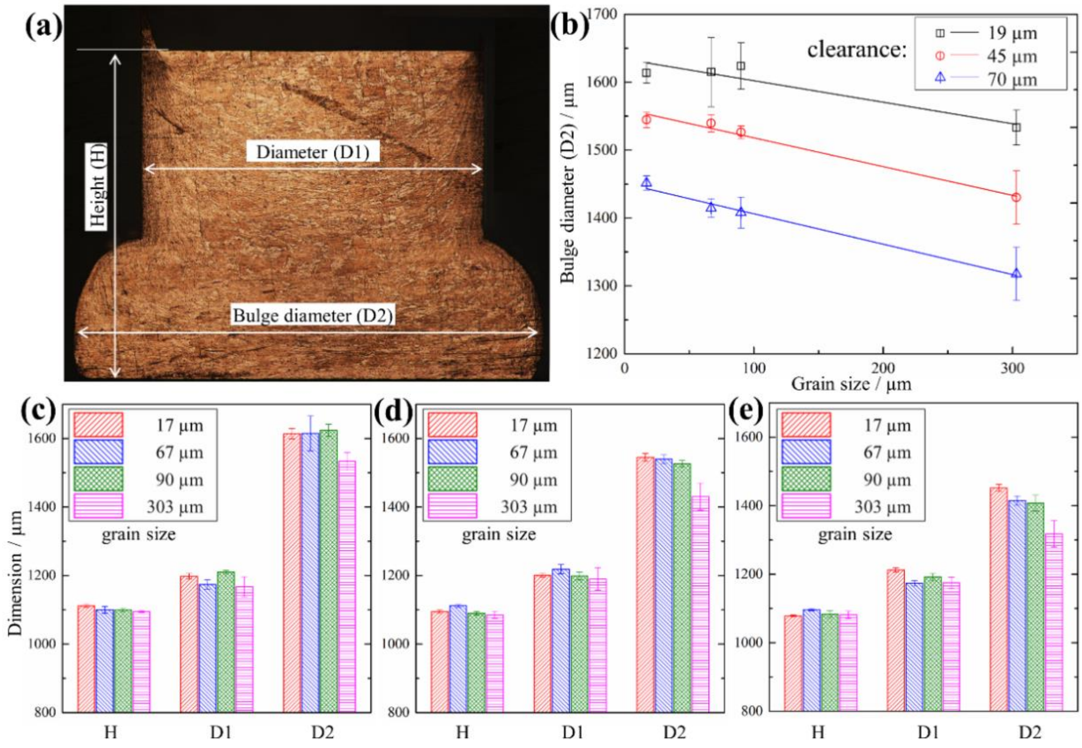

Fig. 4.13 (a) Dimension illustration; (b) variation of bulge diameter; dimension of each feature under different grain sizes and punch-die clearances of (c) 19 μm, (d) 45 μm, and (e) 70 μm.

Radius variation during heading operation

In meso/microforming, the roundness or cylindricity of the freeform surface is an important factor for the evaluation of the formability of the forming process of axisymmetric parts. The traditional FEM, however, cannot accurately predict roundness or cylindricity due to the homogeneous-property assumption of material. CPFEM, considering grain orientations, is a good approach to evaluating these factors in meso/microforming. In this study, the roundness was studied by investigating the radius change of the heading feature in micro-heading operation through FEM and CPFEM simulations. Due to the difficulty of re-meshing in CPFEM simulation of shearing, only the simulations of micro-heading were conducted. CPFEM simulation was conducted and implemented through scripts and subroutines in software

ABAQUS/Explicit. Symmetrical constraints were applied on the x and y planes of the quarter model. These boundary conditions constrained the torsion and normal displacement of grains on the symmetrical planes, so the radius change of the whole model was affected less. The traditional FEM based on the homogeneous theory was also done for comparison. The material properties in FEM were obtained from the experimental data in Section 2.1. Displacement boundary conditions were applied, and all the interfaces were frictionless.

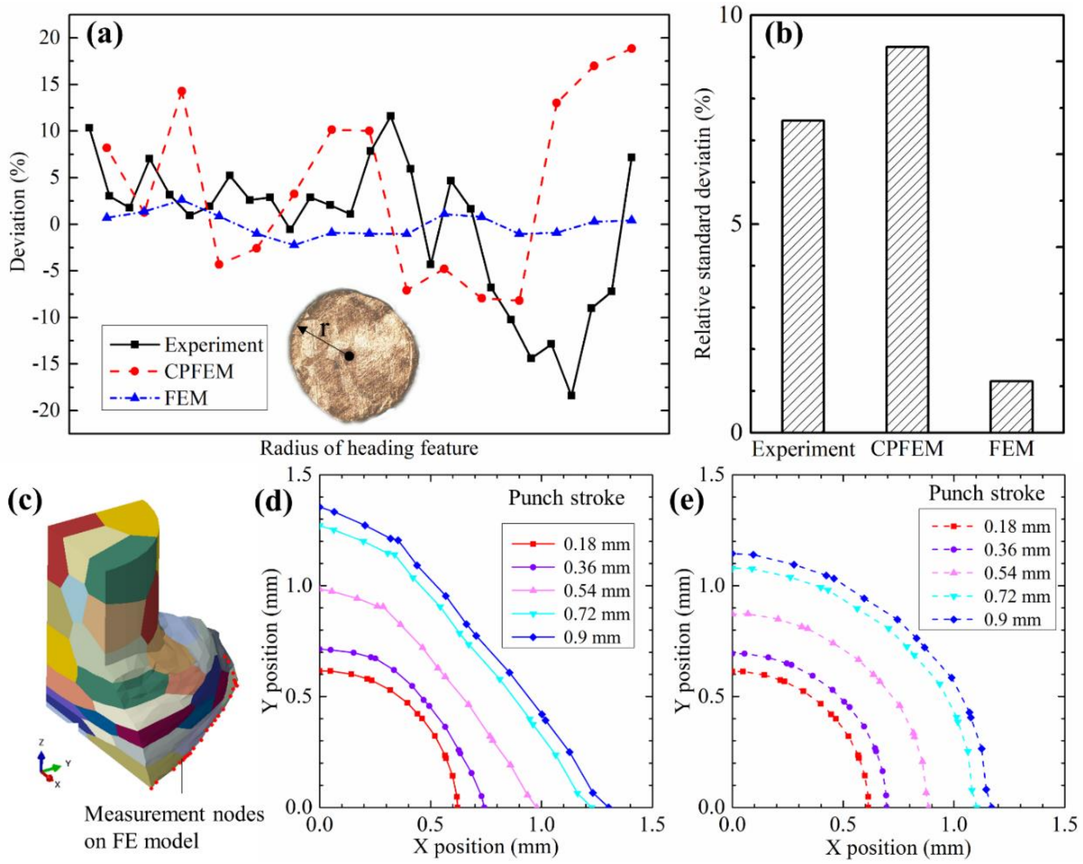

Fig. 4.14 (a) Radius change of the heading feature; (b) the relative standard deviation of radius; (c) the illustration of measurement nodes on simulation model; and the variation with punch stroke of X and Y position of the measurement nodes predicted by (d) CPFEM model and (e) FEM model.

The results of the experiment, CPFEM and FEM are illustrated in **Fig. 4.14**. **Fig. 4.14** (a, b) gives the deviation of the cylindrical radius of the heading feature around the perimeter and their relative standard deviation. The radius changes in CPFEM and experimental results have huge fluctuations, while the result in FEM is smooth. It is revealed the CPFEM predicts the unevenness of the cylindrical radius reasonably compared with the FEM, and the CPFEM's relative standard deviation is close to the experimental result. In the down scaling microforming, the effect of inhomogeneous properties of individual grains are pronounced, especially on the freeform geometry without tooling constraint. Thus, the grain-structure-based CPFEM is more accurate in this scenario. In addition, **Fig. 4.14** (d, e) present the X and Y position of the measurement nodes in **Fig. 4.14** (c) with different punch strokes to show the roundness variation of the heading feature in the forming process. It can be seen that at about half of the total stroke, the cylindricity predicted by the CPFEM model is apparently reduced, while the cylindricity predicted by the FEM model is always good.

4.3.4 Surface defects

The morphologies of the final parts were observed by scanning electron microscope (SEM). **Fig. 4.15** shows the fine-grained parts with different punch-die clearances. The decrease of the diameter of heading feature and the increase of burr volume are more apparent with the larger punch-die clearance.

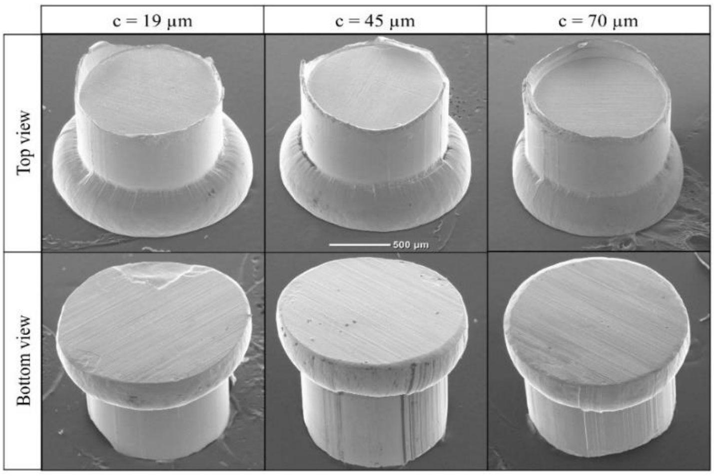

Fig. 4.15 Micro plug parts with grain size of 17 μm by using different punch-die clearances.

The blanked surfaces of the final parts with different grain sizes after micro-blanking operation are given in **Fig. 4.16**. The fracture surfaces were observed. Through the initiation, growth, and coalescence of microvoids, fracture and rough surface were formed on the blanked regions. The parabolic dimples on the fracture region reflect the position and shape of microvoids. From this diagram, it can be seen that the number of dimples on the fracture surface decreases with the increase of grain size, but the large-sized dimples appear on the fracture surface with the coarse-grained material. This phenomenon was not observed in the prior studies [13, 28, 113].

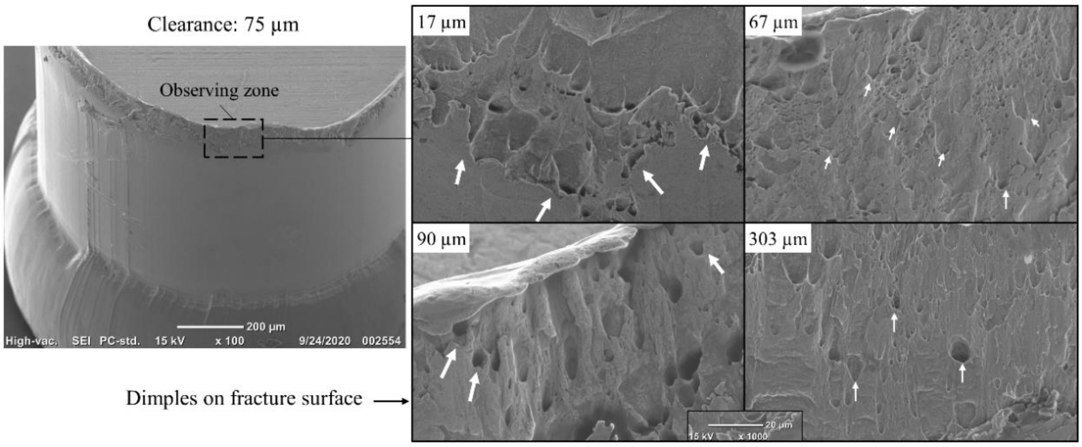

Fig. 4.16 Fracture surfaces generated in shearing deformation with different grain sizes.

Moreover, the morphologies of the bottom surfaces of the final parts with different grain sizes are shown in **Fig. 4.17**. The micro plug parts with the grain size of 17 and 67 μm have a more circular geometry, but the parts with the grain sizes of 90 and 303 μm show more unevenness on the free-form surface. Among the defects on the bottom surface, the sunken area is likely to occur on the bottom surface near the edge because of the rollover and the uneven hardening distribution at the bottom surface after micro-blanking. During the extrusion deformation, the bottom surface could not be fully in contact with the die surface resulting in the occurrence of a sunken area. With the increase of grain size, more undesirable defects are found on the bottom surface, such as pits, cracks and surface damage. The formation mechanism of pits could be related to external factors, such as dirt or impurities on the surface of specimen or die. During material extrusion process, the material is pushed to the die surface and extruded, the dirt or impurities on the interface between the specimen and the die will damage the part surface and pits are then formed. On the other hand, the formation of crack is affected by internal factors, including strain accumulation and work hardening. When the material deformation reaches a critical value, cracks may occur along the grain boundaries at the strain-accumulated region. It is noticed that cracks are more likely to appear with coarse-grained material, since the coarse-grained material has a lower threshold to accumulate deformation energy during the extrusion deformation. Similarly, the appearance of surface damage is induced by external forces or articles crushing the work hardening area where the region of surface reaches the ductile fracture limit due to strain accumulation. It is revealed that fine-grained material has a better surface morphology due to its better ductility than coarse-grained material.

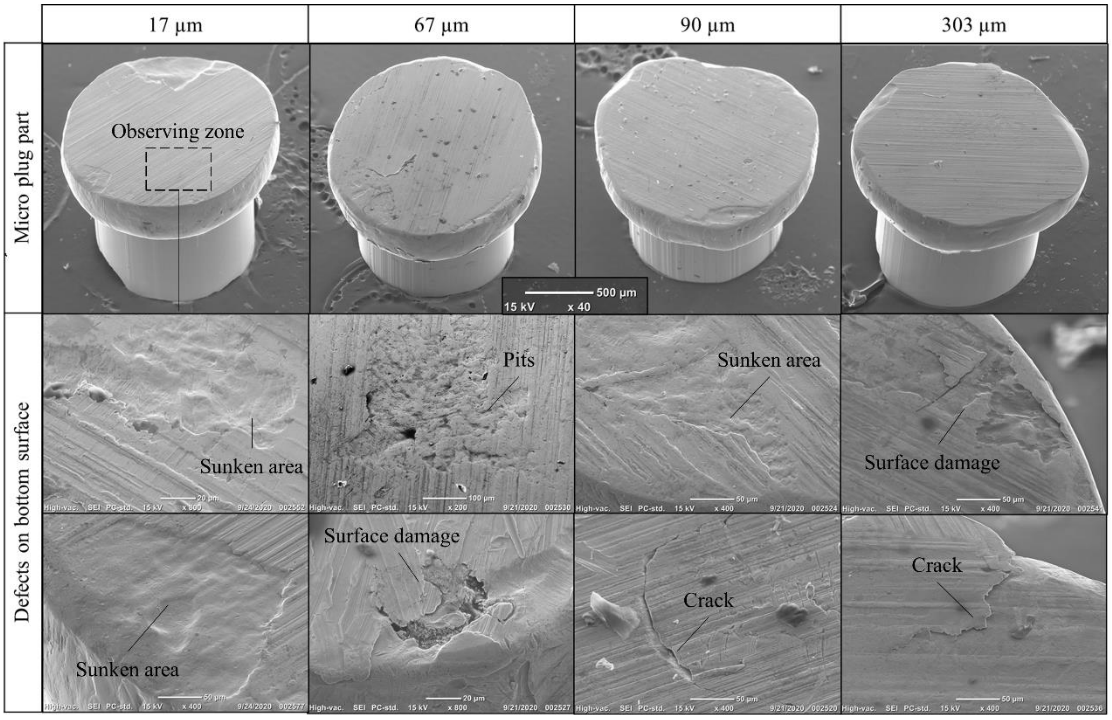

Fig. 4.17 Defects on the bottom surface of the formed parts with different grain sizes.

In addition, **Fig. 4.18** shows the surface defects on the bulge surface with different grain sizes. The crack on the bulge surface appears in each case since the heading feature undergoes severe deformation in shearing and extrusion deformation, causing large strain accumulation and work hardening. If a crack initiates on the shearing surface after the micro-blanking operation, it will extend in the width direction during the micro-heading operation due to the lateral stress. Compared with the thin and regular heading-formed cracks, the heading-extended cracks are wider and warped.

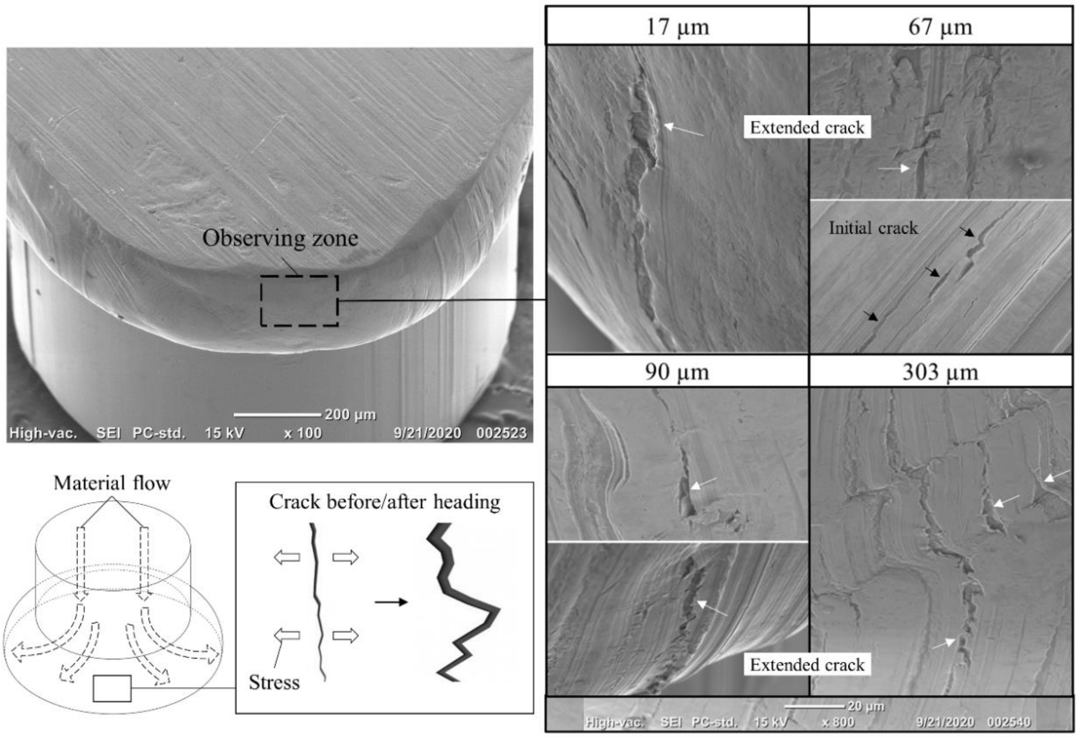

Fig. 4.18 Crack formation on the bulge surface of the formed parts with different grain sizes.

The causes of these defects and the improving methods are summarized in **Table 4.5**. In summary, to achieve better forming quality, clean forming conditions could be considered to reduce the externality-induced surface defects, and warm forming (heated under the re-crystallization temperature of material) could be another feasible way to improve the uniform deformation of the process.

Table 4.5 Causes of surface defects and improvement approaches

Defect	Cause	Improvement
Dimple	Evolution of microvoids in ductile metal	Subsequent processing
Crack	Strain concentration; get worse with lateral stress states	Avoid large deformation; improve formability
Sunken area	Undesirable surface contact in extrusion	Good lubrication

Pits and surface damage	Impurities or dirt on the interface	Clean forming condition

4.4 Summary

In this study, a compound microforming system was designed and established for the fabrication of micro-plug parts by directly using sheet metals. The experimental and numerical investigations were conducted from the aspects of forming load, microstructural evolution, geometrical precision, surface defects and radius variation of the formed parts considering grain size effect and the geometrical size effect of punch-die clearance. The following conclusions can be drawn from this study:

1) The compound microforming system combines micro-blanking and micro-heading operations, which makes it possible to fabricate plug-shaped parts from sheet metals within one single punch stroke. Sheet-based bulk meso/microforming also facilitates the positioning, transporting and ejection operations to promote efficiency and potential for mass production.

2) The load-stroke curves are divided into blanking, transition and two heading stages. The finer grains and thicker punch-die clearance increase the needed forming load. It is also speculated that when the ratio of clearance to grain size (c/d) equals one, the maximum ultimate shear stress in the blanking stage is identified, and it can be strictly validated in future research.

3) Three shear bands and three dead metal zones are identified on the cross-section of the final part based on the microstructure observation, hardness and simulated strain distribution. With the variation of grain size and punch-die clearance, the area of the characteristic zone changes. It is found that the material at the middle centre flows to the shearing area during blanking operation; while the material in the bottom centre is then extruded along the lateral direction to die edge during

heading operation.

4) The width of burr is directly related to the punch-die clearance, and grain size does not significantly affect the width of burr. The height of burr generally reaches the maximum when c/d equals one. The volume of burr is usually increased with the punch-die clearance. The increase of both the volume of burr and grain size will lead to increased material loss of the formed part.

5) The height and the cylindrical diameter of the final parts change little with grain size or punch-die clearance, but the bulge diameter is decreased with the larger grain size and clearance. The variation of the bulge diameter in the peripheral direction is predicted well with the CPFEM simulation.

6) Surface defects of the final parts, including the fracture surface with dimples near the top edge, the sunken area, pits, cracks, and surface damage on the bottom surface, and the cracks on the bulge surface were observed, and their formation mechanisms were analyzed. Finer-grained material, a cleaner processing condition can be considered to eliminate the undesirable surface defects.

In summary, relative finer grains and a smaller punch-die clearance can promote the quality of the sheet-based bulk parts and avoid material loss, but the ratio of punch-die clearance to grain size should be selected properly to avoid higher ultimate shear stress and worse burr formation.

Chapter 5 Constitutive modeling of meso/microforming considering metallic anisotropy and structures

5.1 Introduction

With the increasing demand for meso-/micro-scaled parts and structures due to product miniaturization, the development of meso-/micro-manufacturing technologies for fabricating precision meso/microparts has become a technological bottleneck that needs to be critically addressed [57]. Meso/microforming is one of the promising meso-/micro-manufacturing technologies with the advantages of high productivity, good quality of net- and near-net-shape products, and low production costs [10]. The process employs the plastic deformation of metallic materials to change the geometrical shape of billets to the final geometries of the parts. With the scaling down of workpiece sizes from the macroscale to the meso/microscale, the information developed at the macroscale may not be directly leveraged at downscaled scenarios, and thus, decision-making and solution generation in meso/microforming may not be directly supported by traditional theories and the knowledge developed for the macroscale. The main reason such knowledge cannot be directly translated to the meso/microscale is the existence of so-called size effects, which affect meso-/micro-scaled deformation behaviors, process performance, and the quality and properties of fabricated meso-/micro-scaled parts and structures [47]. In addition, the size-related deviations of behaviors and performances comprise another difficult issue that needs to be addressed.

Although the mechanism and modeling of size effect have been studied and developed, the developed surface layer model and composite model ignore the different properties of individual grains and grain boundary structures in polycrystalline materials, and CPFEM is a time-/resource-consuming approach that is not very promising and efficient in solving engineering problems. Therefore, there is still a lack of suitable modeling methods considering grain textures and structures, which limits the application of finite elements method (FEM) simulations for meso-/micro-scaled forming issues. In tandem with this, this research proposed a modeling method with a portion-split approach for realizing material anisotropy and inhomogeneity. For this modeling, the workpiece was split into a grain boundary portion and a grain interior portion, where the grain boundary portion was considered to be the homogeneous and isotropic material, and the properties within one-grain interior were isotropic and orientation-dependent but different from other grains. The feasibility of the proposed model was validated and discussed through experimental and numerical studies in terms of flow stress, strain distribution, and cylindrical surface variation. Combined with GTN criterion, the proposed model was applied to investigate ductile fracture in 2D and 3D simulations, and its abilities to predict deformation and crack generation were verified through meso-heading experiments and simulations. This study aims to develop an effective simulation method with a good trade-off between accuracy and efficiency to solve the meso- and micro-scaled forming issues of polycrystalline metallic materials and to provide an in-depth understanding of size effects in meso- and micro-scaled deformation.

5.2 Constitutive model development

The modeling procedure is illustrated in **Fig. 5.1**. First, three groups of tensile tests with differently grained materials were conducted, and their flow stress and the average grain sizes of each group were obtained. The fractions of grain boundaries and grain interiors of each group were calculated based on a simplified hexagonal geometrical model. To quantitively describe the flow stress, the Voce model [35] was introduced as $\frac{\sigma_s-\sigma}{\sigma_s-\sigma_0} = \exp\left(-\frac{\varepsilon}{\varepsilon_c}\right)$, where three parameters σ_s, σ_0, and ε_c need to be identified. According to the fraction values and the fitted models, the flow stress of grain boundaries and average grain interiors were obtained, respectively. Considering the distribution of Schmid factors and the Sachs model [114], the upper and lower bounds of the flow stress of grain interiors were also determined, where the flow stress of each grain interior is located in-between. Based on the geometrical and mechanical properties, the tessellations and constitutive models of grain boundaries and interiors were developed for simulations.

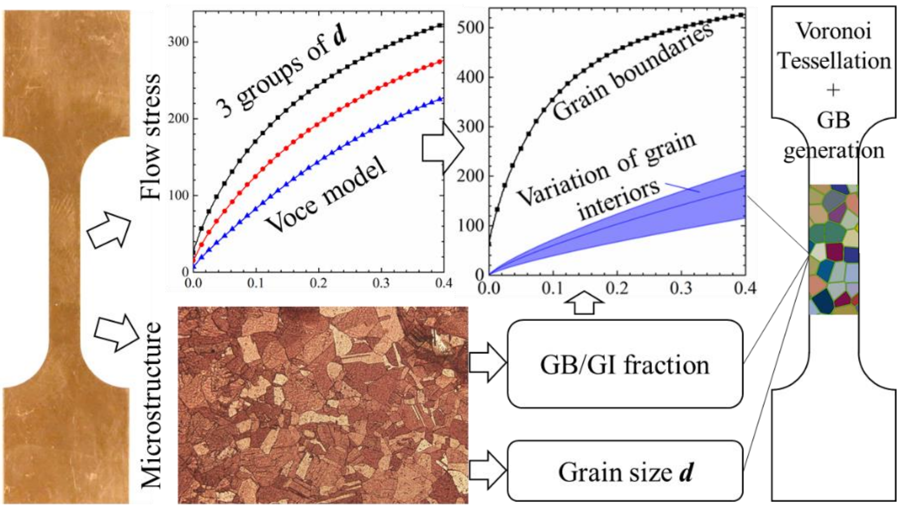

Fig. 5.1 Development of the constitutive model.

5.2.1 Tensile test

Uniaxial tensile tests were conducted to obtain the original flow stress data of pure copper with different grain sizes. The pure copper specimens were annealed under different heat treatment conditions to obtain different microstructures. The dog-bone-shaped specimens with a thickness of 1 mm and different grain sizes, as shown in **Fig. 5.2**, were used in the tests. The strain rate was 0.01 s^{-1} to eliminate the effect of velocity. The flow stress curves of the specimens with the grain sizes of 20, 60, and 225 μm are shown in **Fig. 5.2**. It is revealed that the flow stress is clearly decreased with increasing grain size.

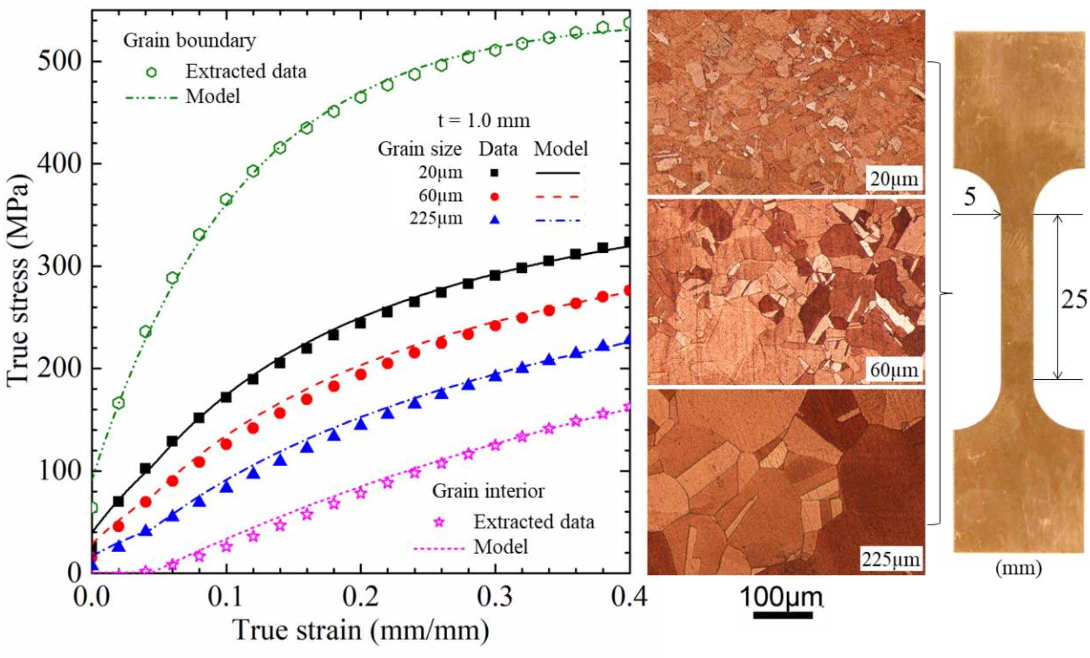

Fig. 5.2 Flow stress determined based on the experimental data and the fitted models with different grain sizes; the extracted data and the constitutive models of grain boundaries and average grain interiors; the tensile test specimen with various microstructures.

5.2.2 *Fractions of grain boundaries and interiors*

The size effects existing in metallic materials include microstructural and geometrical size effects, which are both considered in this research. The surface layer model is a well-known constitutive model that represents both size effects and the different deformation behaviors of surface and inner grains [40, 84]. The surface grains have less constraints from adjacent grains in contrast to the internal grains, so they have lower flow stress. For the coarse-grained materials, the reduction of flow stress is attributed to the increased volume fraction of surface grains. The flow stress can thus be determined by the fraction and properties of both the surface and internal grains and can be designated in the following:

$$\sigma(\varepsilon) = f_s\sigma_s(\varepsilon) + f_i\sigma_i(\varepsilon) \tag{5.1}$$

where $\sigma_s(\varepsilon)$ and $\sigma_i(\varepsilon)$ are the flow stress of the surface and internal grains, respectively. f_s and f_i are the corresponding volume fractions of surface and internal grains. At a macroscale with fine-grained materials, the volume fraction of surface grains can be ignored. When a workpiece size is decreased to the mesoscale or microscale, there are only a few grains comprising the specimen and the fraction of surface grains increases greatly, which results in a decrease of flow stress.

The composite model represents the polycrystalline metallic material as a composite material with a continuous network of work-hardened grain boundaries and discontinuous grain interiors [41, 78]. In this research, the flow stress of the inner material includes grain boundaries and grain interiors, which is expressed as follows:

$$\sigma_i(\varepsilon) = f_{GI}\sigma_{GI}(\varepsilon) + f_{GB}\sigma_{GB}(\varepsilon) \tag{5.2}$$

where $\sigma_{GI}(\varepsilon)$ and $\sigma_{GB}(\varepsilon)$ are the average flow stress located at grain interiors and grain boundaries, respectively. f_{GI} and f_{GB} are the volume fractions of grain interiors and grain boundaries, respectively.

According to the surface layer model and the composite model, material can be divided into three different parts, viz., surface grains, grain interiors, and grain boundaries [115]. It is expressed as $f_s + f_{GI} + f_{GB} = 1$. To obtain the fraction of grain boundaries, the thickness of grain boundary can be expressed in terms of grain size (in μm) as follows [78]:

$$t_G = kd^n (0 < n < 1) \tag{5.3}$$

where d is grain size (in μm), k and n are the constant for a given material. For copper and its alloys, the values are $k = 0.133$ and $n = 0.7$, respectively.

The fractions of surface grains, grain interiors, and grain boundaries are calculated based on the hexagon-structural assumption, as shown in **Fig. 5.3**. The fractions of different portions are shown in the following [116]:

$$\begin{cases} f_s = \dfrac{d}{t} \\ f_{GI} = (1 - f_s)\left(1 - \dfrac{2}{\sqrt{3}} \cdot \dfrac{2\bar{t_G}}{\bar{d}}\right)^2 \\ f_{GB} = (1 - f_s) \cdot \dfrac{4}{\sqrt{3}} \cdot \dfrac{2\bar{t_G}}{\bar{d}}\left(1 - \dfrac{2}{\sqrt{3}} \cdot \dfrac{2\bar{t_G}}{\bar{d}}\right) \\ \bar{d} = \dfrac{\pi}{4} d \\ \bar{t_G} = 1.57 t_G \end{cases} \tag{5.4}$$

where t_G and $\bar{t_G}$ respectively represent the thickness of the grain boundary and its mean value, and d and $\bar{d}$ respectively represent the grain size and its mean value [41].

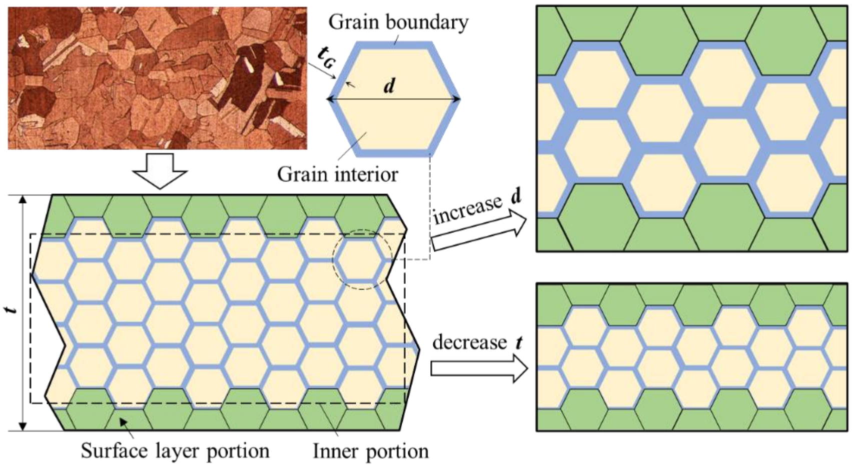

Fig. 5.3 The composition of a microstructure and its size effect in cross-section, which

consists of a surface layer portion (f_{surf}), grain boundaries (f_{GB}), and grain interiors (f_{GI}).

Since the surface grains have less hardening effect and constraint compared with internal grains, they are thus regarded without a grain boundary strengthening effect, viz., $\sigma_{surf} = \sigma_{GI}$ to simplify the model [116]. The flow stress of polycrystalline material is thus considered through the combination of two portions, given in the following:

$$\sigma(\varepsilon) = (f_s + f_{GI})\sigma_{GI}(\varepsilon) + f_{GB}\sigma_{GB}(\varepsilon) \tag{5.5}$$

When incorporating Eq. (5.3) into Eq. (5.4), the fractions of each portion are obtained as follows:

$$\begin{cases} f_s + f_{GI} = \dfrac{1}{t}(1.228d^{0.7} - 0.377d^{0.4}) + (1 + 0.377d^{-0.6} - 1.228d^{-0.3}) \\ f_{GB} = 1 - f_{GI} - f_s = \dfrac{1}{t}(0.377d^{0.4} - 1.228d^{0.7}) + (1.228d^{-0.3} - 0.377d^{-0.6}) \end{cases} \tag{5.6}$$

Therefore, once the thickness and the average grain size of specimens are obtained, the fractions of each portion can be determined. For the tensile test specimen in this study, the fraction values of each portion for different grain sizes are illustrated in **Table 5.1**.

Table 5.1 Flow stress and fraction factors of different grain sizes with a thickness (t) of 1 mm in Eq. (5.5).

Grain size (μm)	Thickness (μm)	$\boldsymbol{f_s + f_{GI}}$	$\boldsymbol{f_{GB}}$
20		0.571	0.429
60	1000	0.692	0.308
225		0.824	0.176

For the proposed model, the polycrystalline material is treated as an aggregate of surface grains, grain interiors, and grain boundaries. Their contributions to material properties are weighted according to their fractions. Size effects take effect in this model by changing the values of the fractions of the three portions. As illustrated in **Fig. 5.3**, the macro-scaled specimen with the fine-grained material is homogeneous due to the even distribution of grains. When the specimen is scaled down to the microscale, there are only a few grains existing along the thickness direction. The fraction of surface grains is increased, which induces a decreased in the strength of the material. By contrast, when the grains are coarsened, the thickness of the grain boundary is increased, but the total fraction of grain boundaries is thus decreased due to the decrease of grain number. In addition, since the number of grains in the specimen is decreased, the collective material performs with greater uncertainty since each grain shows a random orientation and irregular properties, which is discussed in Section 5.2.4.

5.2.3 Properties of grain boundaries and interiors

The grain boundary portion has been revealed to be mostly amorphous in many atomic simulations [117, 118]. Thus, in this research, it is presented by a homogeneous plastic flow model implemented to describe its mechanical behaviors. However, the flow stress of the grain interior is affected by its grain orientation, so only the average model is obtained.

The flow stress data of grain boundaries and average grain interiors can be obtained through a coefficient elimination method using the flow stress of differently grained materials, represented by the green and pink dots in **Fig. 5.2**. The constitutive models of $\bar{\sigma}_{GI}$ and σ_{GB} are fitted into the Voce equation [35] designated in the following:

$$\begin{cases} \dfrac{\sigma_s^{GB} - \sigma_{GB}}{\sigma_s^{GB} - \sigma_0^{GB}} = \exp\left(-\dfrac{\varepsilon}{\varepsilon_c^{GB}}\right) \\ \dfrac{\sigma_s^{GI} - \bar{\sigma}_{GI}}{\sigma_s^{GI} - \sigma_0^{GI}} = \exp\left(-\dfrac{\varepsilon - \varepsilon_{off}}{\varepsilon_c^{GI}}\right) \end{cases} \tag{5.7}$$

where σ_0^{GI} and σ_0^{GB} are the initial yield stresses of grain interiors and grain boundaries, σ_s^{GI} and σ_s^{GB} are the saturation stresses of grain interiors and grain boundaries, ε_c^{GI} and ε_c^{GB} are the characteristic strains of grain interiors and grain boundaries, and ε_{off} is the strain offset in the flow stress of grain interiors, which is related to the grain orientation. The initial yield stress of grain interiors σ_0^{GI} is very small in experimental data and is assumed 1 MPa. The parameters in this model are shown in **Table 5.2**. The flow stress equations for GB and GI of pure copper are:

$$\begin{cases} \dfrac{543 - \sigma_{GB}}{452} = \exp\left(-\dfrac{\varepsilon}{0.11}\right) \\ \dfrac{315 - \bar{\sigma}_{GI}}{314} = \exp\left(-\dfrac{\varepsilon - 0.042}{0.5}\right) \end{cases} \tag{5.8}$$

The constitutive model determines the flow stress of the grain interior and grain boundary of pure copper. The experimental data and the constitutive models with different grain sizes, as well as the extracted data and the constitutive models of grain boundaries and average grain interiors are illustrated in **Fig. 5.2**. The constitutive models are consistent with experimental data. The flow stress curve of the grain boundary is generally consistent with the prior research [78, 116], as shown in **Fig. 5.4** (a).

Table 5.2 Parameters of the constitutive model for grain boundaries and interiors.

σ_0^{GI}	σ_s^{GI}	ε_c^{GI}	σ_0^{GB}	σ_s^{GB}	ε_c^{GB}
1 MPa	315 MPa	0.5	91 MPa	543 MPa	0.11

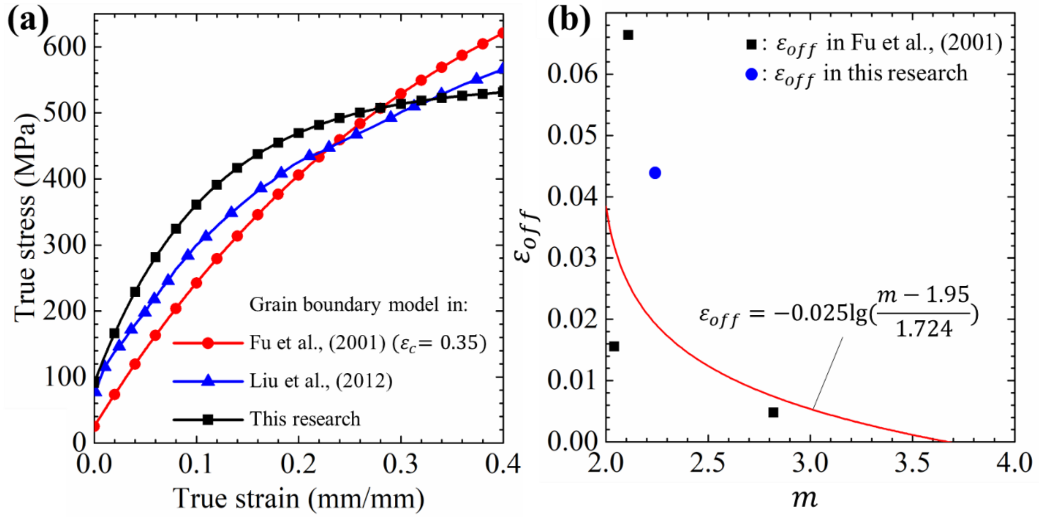

Fig. 5.4 (a) The constitutive models of grain boundaries for copper in [78], [116], and this research. (b) The strain offset ε_{off} varies with the orientation factor m. The data are extracted from [78].

5.2.4 *Effect of grain orientation*

Considering the effect of grain orientation, the Schmid factor is introduced in the constitutive model. A slip system in crystalline material is composed of a set of symmetrically identical slip planes and an associated family of slip directions along the most possible direction where dislocation would occur with plastic deformation. Depending on the type of lattice, different slip systems are presented in the material. When force is applied to crystal material, the crystal lattices glide along a specific slip direction and on a specific slip plane. Slip always occurs on the close-packed planes that have the greatest density of atoms and along with the close-packed directions where there are the most atoms in a certain length. A slip plane and a slip direction constitute a slip system, where the critical resolved shear stress (CRSS), τ_R, is required to describe the slip system, as shown in the following:

$$\tau_R = cos\varphi cos\lambda \cdot \sigma = \beta \cdot \sigma \tag{5.9}$$

where β is the Schmid factor [87] related to the grain orientation and $0 < \beta \leq \frac{1}{2}$; σ is the applied stress, φ is the angle between the normal stress and the normal direction of the slip plane, and λ is the angle between the slip direction and the normal stress. The reciprocal value $m = \sigma/\tau_R$ is the well-known Schmid factor for single slip systems, which presents the effect of grain orientation. In the Sachs model [119], the average m-factor is 2.23, which describes the mean properties of grain interiors, and varies between 2 and 3.674 [114].

The strain offset ε_{off} in Eq. (5.7) was also observed in prior research [78]. It can be assumed in an empirical logarithmic function with m since it varies with the grain orientations. It is expressed as follows:

$$\varepsilon_{off} = -0.025 \lg\left(\frac{m - 1.95}{1.724}\right) \tag{5.10}$$

In this function, ε_{off} is zero when m is 3.674, which is in <111> orientation, and reach the maximum value of 0.038 when m is 2. The relation between ε_{off} and m is shown in **Fig. 5.4** (b).

The grain orientation and distribution of the pure copper specimens with two grain sizes were detected using the EBSD process, and the results are illustrated in **Fig. 5.5**. In the orientation image maps, different colors represent the random initial orientation of each grain. The Schmid factor was calculated from the Euler angles of a single grain. Since the FCC crystal has 12 slip systems, the minimum one is calculated as m factor, which is the easiest deforming slip system, generally presenting the strengthening coefficient along the close-packed grain orientation. A larger Schmid factor implies that this grain is harder to deform. Their mean values for the grain sizes of 60 and 225 μm are 2.19 and 2.22, respectively, which are close to the orientation factor (2.23) in the Sachs model [114].

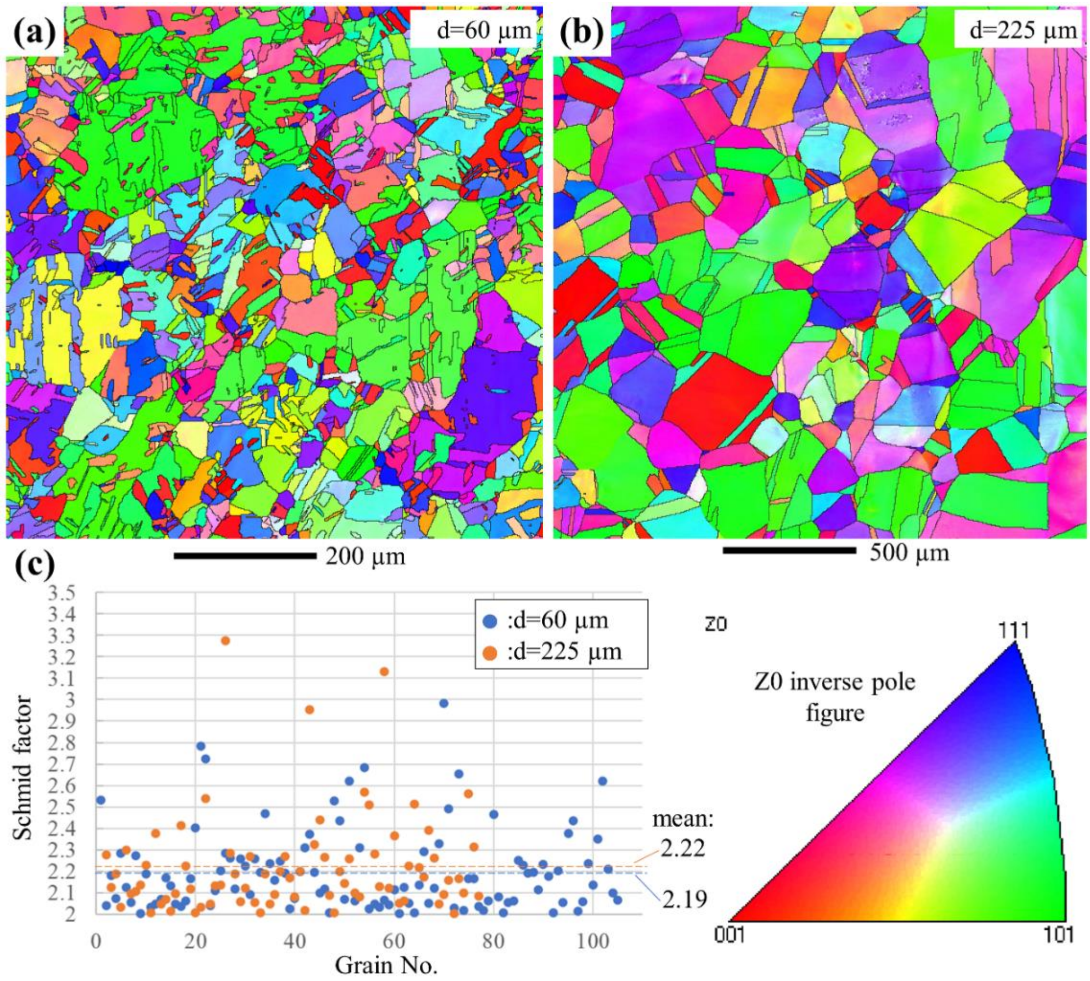

Fig. 5.5 Grain orientation maps of copper specimens with grain sizes of (a) 60 and (b) 225 μm, and (c) the Schmid factor distribution of each case, where the average values of the Schmid factor are 2.19 and 2.22, respectively.

The individual grain of grain interiors is described as single crystal considering the strengthening coefficient according to grain orientation, whose flow stress is expressed by m and τ_R as follows:

$$\begin{cases} \sigma_i(\varepsilon) = m_i \tau_R(\varepsilon), \qquad i = 1,2,\dots, number\ of\ grains \\ \qquad\qquad m_i \in [2, 3.674], \qquad \bar{m} = 2.23 \end{cases} \tag{5.11}$$

The upper and lower bounds of the flow stress of grain interiors are obtained, as illustrated in **Fig. 5.6** (a). It can be seen the upper and lower bounds of the flow stress of grain interiors almost cover the data from prior research [78, 116]. **Fig. 5.6** (b) illustrates that the grain orientation distribution of the specimen is random. **Fig. 5.6** (c) presents the *m*-values in the range among the three typical grain orientations of [111], [100], and [110].

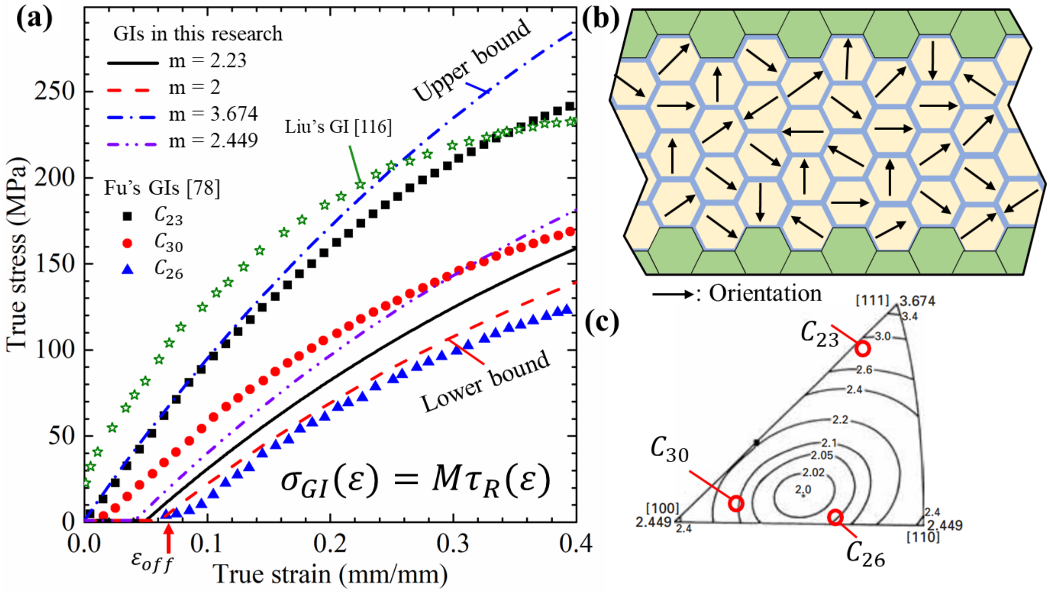

Fig. 5.6 (a) Flow stress curves of the grain interior with different *m*-factors, compared with grain interior data extracted from Fu's [78] and Liu's [116] models. (b) Illustration of grain orientation distribution on the cross-section. (c) *m*-factors as a function of orientation in the Sachs model [114].

By introducing the ratio M_i, which presents the *m*-factor of the *i*-th grain divided by $\bar{m}$ of 2.23, the constitutive model is finally described as follows:

$$\begin{cases} \sigma(\varepsilon) = \sum_{i}^{N} f_i M_i \bar{\sigma}_{GI}(\varepsilon_i) + f_{GB}\sigma_{GB}(\varepsilon_{GB}) \\ M_i \in [0.897, 1.648], \qquad \bar{M} \approx 1 \end{cases} \tag{5.12}$$

where f_i and ε_i are the fraction and the strain of the *i*-th grain, respectively, N is the total number of grains in the specimen, and M_i is the strengthening coefficient of the *i*-th grain for the whole grain interiors.

5.3 Model validation

5.3.1 Model validation by experiments

To verify this constitutive model, tests considering size effects were performed, which were the uniaxial tensile tests of the sheet specimen with grain sizes of 15 and 20 μm and thickness of 0.5 mm, uniaxial tensile tests of the sheet specimen with grain sizes of 25 and 40 μm and thickness of 1.5 mm, and uniaxial compressive tests of the cylindrical specimen with a 2 mm height and a 1.2 mm diameter as well as grain size of 17 μm. The fractions of each portion for the above cases are summarized in **Table 5.3**. For the cylindrical specimen, the equivalent thickness was calculated using $t_{cyl} = \frac{1}{2}(2\pi r^2 + 2\pi rh)/\pi r^2 h$, where r and h are the radius and height of cylindrical specimens, respectively.

The obtained flow stress curves compared with the constitutive model are shown in **Fig. 5.7**. It can be seen that the constitutive model is consistent with the experimental results of these study cases. The size effect is mainly caused by the variation of the fraction of grain boundary and interior portions, which changes with change in thickness and grain size. Since the grain boundaries demonstrate higher strain hardening than grain interiors, the larger fraction of grain boundaries induces higher flow stress.

Table 5.3 The fraction of each portion of different study cases.

Thickness (mm)	Grain size (μm)	Fraction	
		$f_s + f_{GI}$	f_{GB}
0.5	15	0.543	0.457
	20	0.580	0.420

1.5	25	0.594	0.406
	40	0.645	0.355
0.462 (cylinder)	17	0.561	0.439

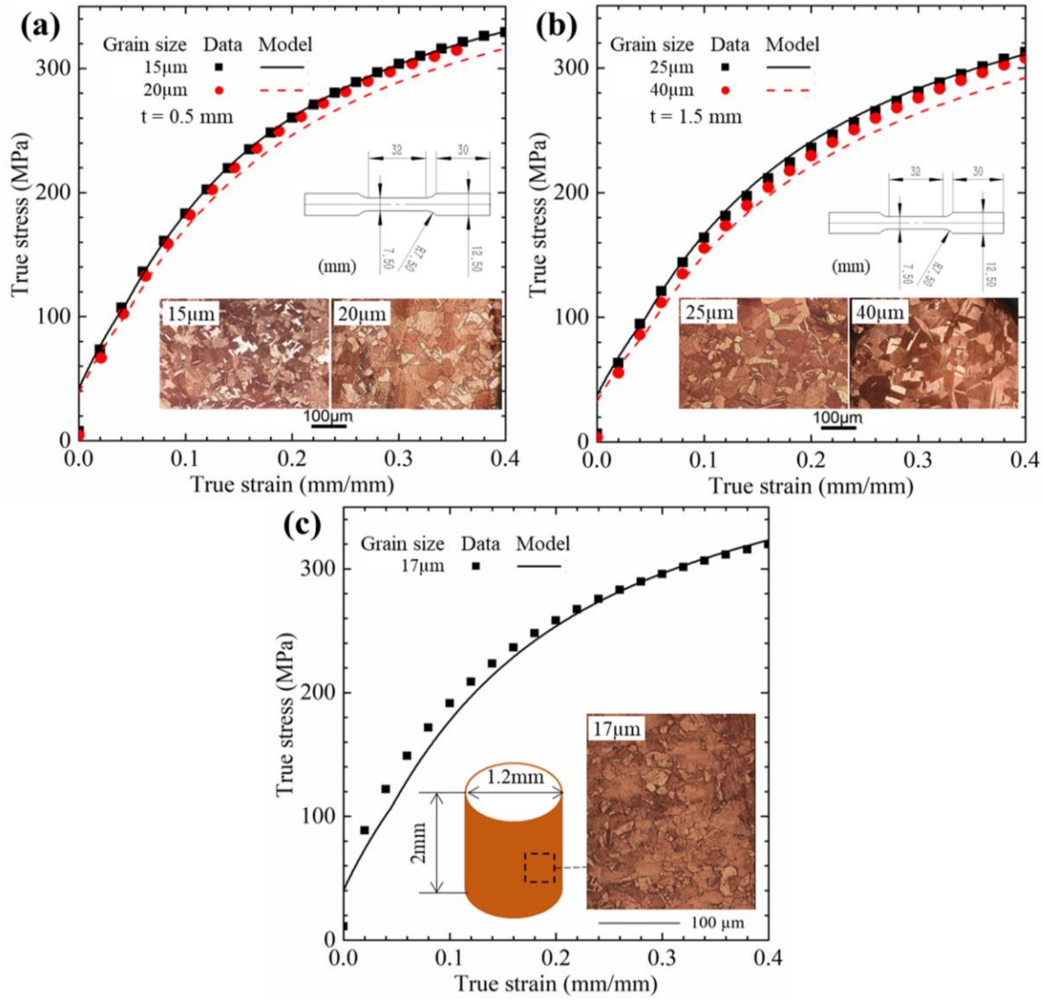

Fig. 5.7 Model validated by (a) tensile tests with grain sizes of 15 and 20 μm and a thickness of 0.5 mm; (b) tensile tests with grain sizes of 25 and 40 μm and a thickness of 1.5 mm; and (c) compressive tests with a grain size of 17 μm and specimens 2 mm in height and 1.2 mm in diameter.

5.3.2 Model validation by FEM

Geometrical model development

The developed grain boundary-grain interiors (GBGI) model was applied in FEM simulations for validation and further studies. Representative volume elements (RVEs) containing numbers of grains in 2D and 3D were employed in different tessellations and mesh methods, as shown in **Fig. 5.8**. The grain and grain boundary tessellations were generated based on a controlled Voronoi method using Abaqus script. For the 3D RVE, as shown in **Fig. 5.8** (a), the cubic geometry was first meshed in hex elements, and elements were then grouped in a set within each grain. The elements located at the interfaces of neighboring grains were extracted and recreated as grain boundaries. In this method, the cube is hex-meshed first. The RVE was divided into many little cubes with the number of grains. (For example, if there are 64 grains in an RVE, the RVE will be divided by 4*4*4.) Grain seeds are then dispersed on the little cube randomly. Each element must have the nearest seed. Thus, the elements that has the same nearest seed are grouped as a grain. Secondly, all the elements are swept one by one to check the neighboring elements (up, down, front, behind, left, and right). If the element and its neighboring elements are not in the same grain, this element is identified as grain boundary. Finally, all the grain boundary elements are selected and regrouped as grain boundary portion. In addition, to precisely obtain the volume fraction of grain boundaries, the average size of elements in the RVE was set as $\sqrt{2}t_G$. For the 2D RVE, as shown in **Fig. 5.8** (b), the tessellation was closer to physical structures. Voronoi polygons were first drawn and generated and then contracted by the value of half grain boundary thickness. and the geometries were then meshed in quad-dominated elements. The 2D model has a more desirable structure similar to the natural polycrystalline microstructures.

In numerical models, each grain had a unique plastic deformation response based on a randomly generated M with the same $\bar{\sigma}_{GI}$. The M-values were generated using a triangular method ranging between 0.897 and 1.648 and had a mean value of 1.

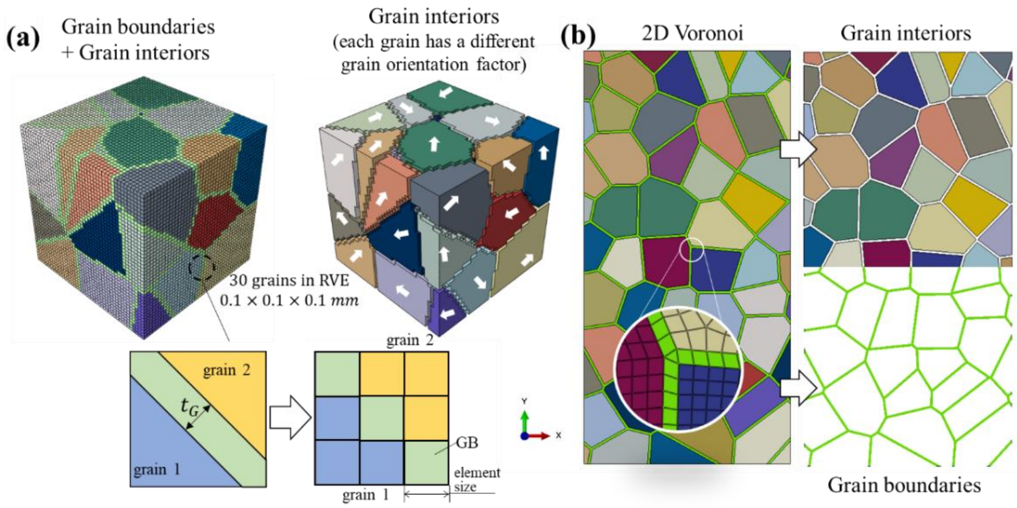

Fig. 5.8 (a) The 3D FEM model considering the portions of grain boundary (light green) and grain interior (other colors) with hex mesh. Each grain has a unique orientation factor, and the grain boundaries are homogeneous. (b) The 2D FEM model with natural microstructures with quad-dominated mesh.

Flow stress responses of RVEs

Study case 1 consisted of a 0.1×0.1×0.1 mm RVE containing 30 grains, where the average grain size was around 58 µm. Study case 2 consisted of a 0.3×0.3×0.3 mm RVE containing 15 grains, where the average grain size is around 221 µm. A uniaxial tensile force was applied on their X-plane. The flow stresses of simulations compared with experimental data are presented in **Fig. 5.9**. The figure shows that the stress-strain responses of RVEs are consistent with the experimental data, and the strengthening effect of fine-grained material is also reflected properly.

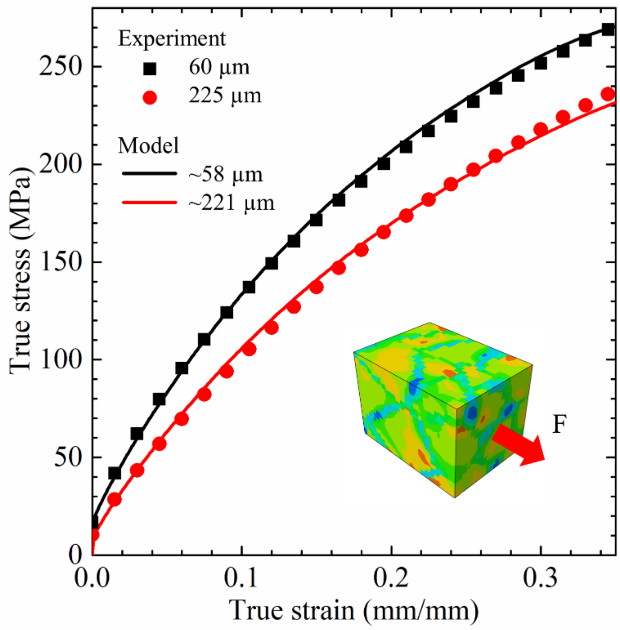

Fig. 5.9 Flow stress curves of the constitutive model in RVE compared with experimental data. Each group has a similar grain size.

5.3.3 Prediction of deformation behaviors compared with CPFEM and experiments

CPFEM considers the texture and grain distribution to study the deformation behaviors of crystal, which can present the inhomogeneous properties for coarse-grained materials at a microscale. The constitutive model of the CPFEM is shown in Section 2.3.4, and the simulation results are compared with the GBGI model. The parameters for pure copper applied in the CPFEM are summarized in **Table 5.4**.

Table 5.4 Parameters in the CPFEM model [90, 120].

C_{11}	C_{12}	C_{44}	$\dot{\gamma}_0$	h_0	τ_0	τ_s	m	a	q
168.4 GPa	121.4 GPa	75.4 GPa	0.001 s^{-1}	180 MPa	16 MPa	148 MPa	0.05	2.25	1.4

In this study, a quarter of meso-cylinder from the cylindrical specimen was generated, as shown in **Fig. 5.10** (a). The meso-cylinders are 2 mm in height and 1.2 mm in diameter, and their average grain size is about 300 μm. They were compressed in the Z direction by 50% and the X- and Y-planes were fixed as symmetrical planes in Abaqus. The models were hexagonally meshed. The tessellation was generated based on a controlled Voronoi method in Neper [109]. With the tessellation, the CPFE model and GBGI model were employed. The CPFE simulation applying the parameters listed in **Table 5.4** was conducted through the subroutine. The GBGI model extracted the elements located on the grain boundary region, and the properties of grain boundaries and grain interiors were created according to the constitutive model in Section 2. The stress-strain curves obtained from the simulation are shown in **Fig. 5.10** (b). The figure shows that the yield stress of the GBGI model is smaller than that of the CPFE model, but their flow stresses become closer with increase in strain. Both simulation results are slightly less than the experimental result, which may be due to external influences such as friction. However, the consumption of resources between the two models is enormously different, as shown in **Fig. 5.10** (c), where the CPFE model is shown to consume a hundredfold times the resource compared to the GBGI model. Therefore, the GBGI model is a more efficient method with acceptable precision.

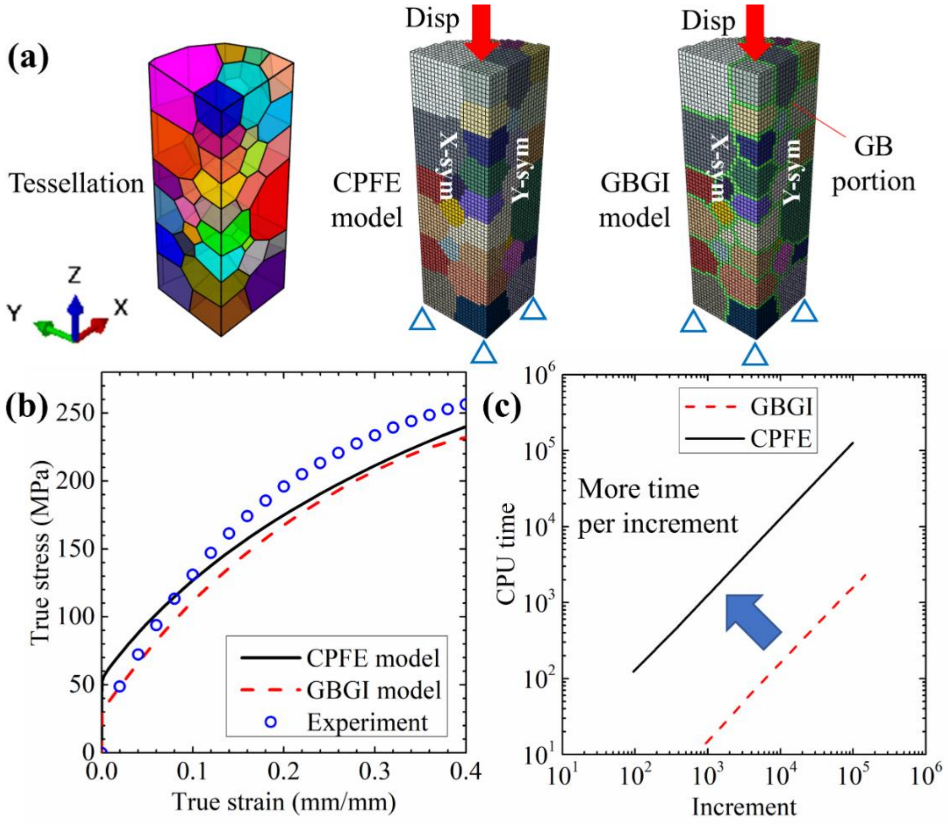

Fig. 5.10 (a) The Neper tessellation and FE models based on different constitutive models. (b) Stress-strain curves of the CPFE and GBGI models and the experiment. (c) A comparison of models according to the calculation time and increment for one case.

The effective strain distribution at the end of the simulation of these two models is shown in **Fig. 5.11**. The plastic equivalent strain in the CPFE model is calculated as $\varepsilon = \frac{\gamma}{\sqrt{3}}$, where γ is accumulated shear strain [121]. The strain in the GBGI model is more discontinuous due to the emphasized barrier-like property of grain boundaries. The maxi-min difference in the CPFE is greater. The deformation of the CPFE model is more irregular but continuous, with several largely deformed regions. From the orthogonal views, the shear bands (white dash) between the two end planes on the cylindrical surface in the GBGI model are more incoherent, since the GBGI model predicts that less deformation happens in the grain boundaries region and the CPFE model predicts the continuous shear band along the slip direction among grains. The side views reveal that the CPFE model predicts a large variation in the radius along the height direction. Its prediction of internal shear bands is similar to the GBGI model.

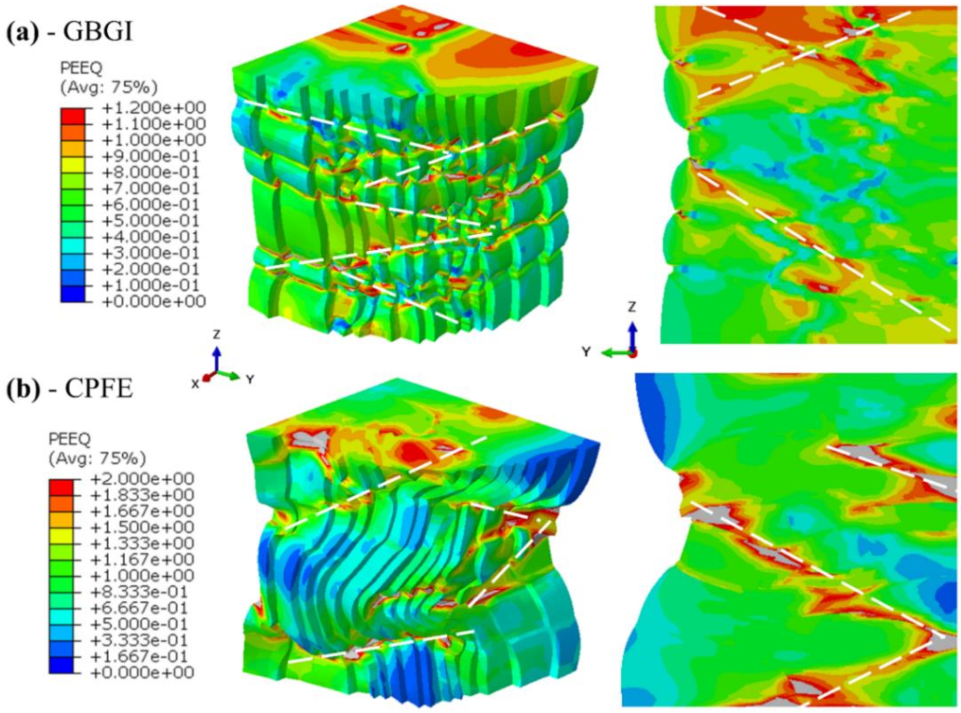

Fig. 5.11 Plastic strain distribution of (a) the GBGI model and (b) the CPFE model. White dash lines illustrate the shear bands.

To quantitively analyze the predictive precision of the inhomogeneous deformation in the meso-upsetting processes of these two models, the radius changes measured by the nodes on the cylindrical surface of FE models were obtained, as shown in **Fig. 5.12**. The nodes for measurement are shown in **Fig. 5.12** (a). They are selected as the outermost nodes at a certain height, and their distances to the central axis are radiuses. The radius variations of the GBGI model, the CPFE models, and the experiments are shown in **Fig. 5.12** (d-f), respectively. It is shown that there is more radius variation in the CPFE model, which is obvious with respect to both height and circumference. Conversely, the radius variation in the GBGI model is smooth, especially with respect to the circumference. Compared to experimental measurements, the CPFE model matches the significant tendency in radius and circumference variation. The deviations in radius counted along the circumference are summarized in **Fig. 5.12** (b). The figure illustrates the variation of radius for certain heights. The CPFE result shows a deviation that is more than double than that given by the GBGI simulation, and the former is closer to experiments, but it differs from experimental results regarding the end surfaces at height of 0.5 mm, since the interfacial friction of the tooling-material surfaces induces more uncertain deformation and a large deviation in radiuses. The deviation along heights at certain degrees is shown in **Fig. 5.12** (c). The experimental results are distributed between the CPFE and GBGI results. In summary, the CPFE model overstates deviation in radiuses, while the GBGI minimizes this effect.

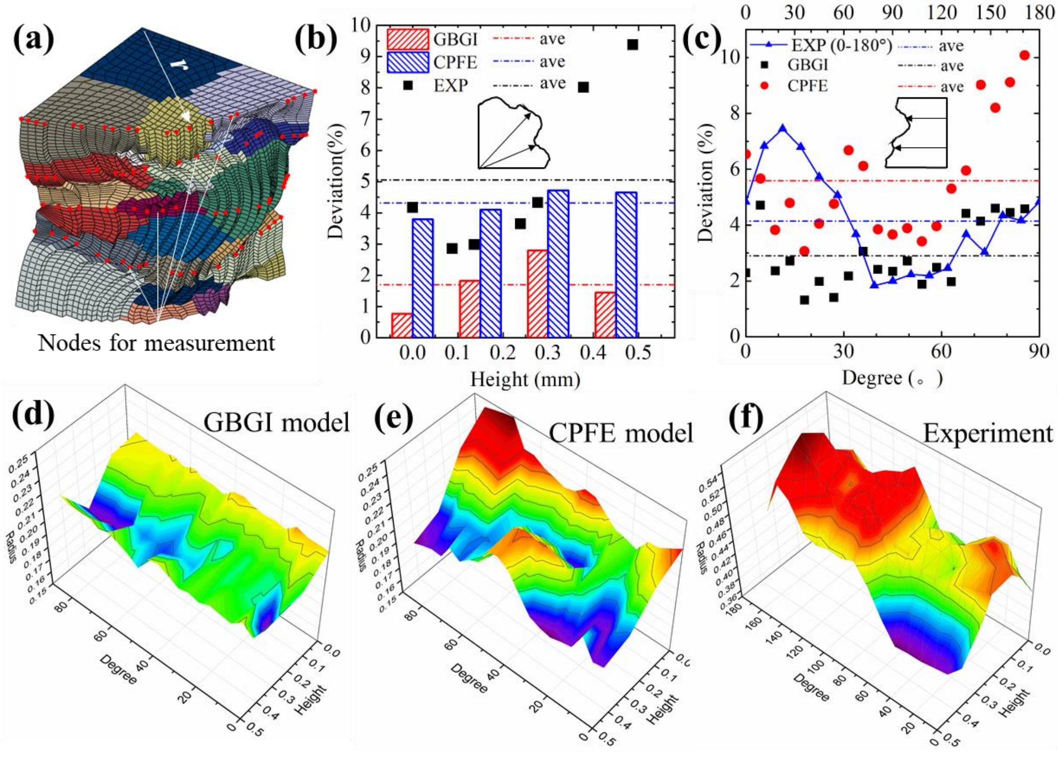

Fig. 5.12 (a) Nodes for measuring radius variation on the cylindrical surface. The radius deviation measured in two models (b) along the circumferential direction at the location with different heights and (c) along the height direction at the location with different angles. The radius variation on the cylindrical surface of (d) the GBGI model, (e) the CPFE model, and (f) the experiment.

The results concerning the compressed specimens with grain sizes of 90 and 300 μm observed using a scanning electron microscope (SEM) and their plastic effective strain in the GBGI 2D simulations are shown in **Fig. 5.13** to investigate the meso-/micro-scaled deformation affected by grain size using the GBGI model. The fine-grained specimen in **Fig. 5.13** (a) keeps its cylindrical shape after compression, and a continuous and straight shear band was generated, which is consistent with the GBGI simulation. By contrast, the coarse-grained specimen in **Fig. 5.13** (b) loses its cylindrical shape and shows an irregular deformation, and discontinuous shear bands were generated in a zig-zag distribution. The GBGI simulation predicted the irregular geometry and shear bands for the coarse-grained material in accordance with experimental observations.

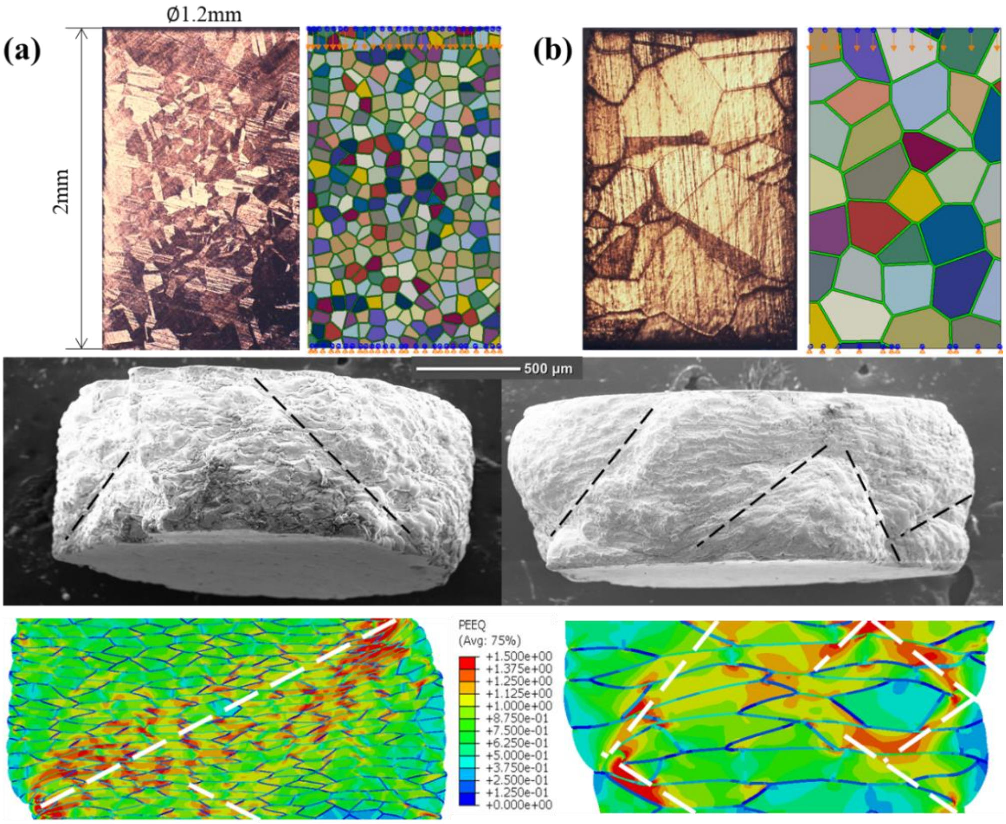

Fig. 5.13 Compressived specimens (initial 2-mm height and 1.2-mm diameter, compressed by 60%) with grain sizes of (a) 90 μm and (b) 300 μm, from the aspects of specimens, SEM observations, and 2D simulations.

In summary, the GBGI model can reflect the inhomogeneous distribution of strain and the random deformation of grains just like the CPFE simulation. The GBGI model sufficiently predicts shear band formation and flow stress and has the capability to detect the dangerous area, but it is limited in predicting the continuous variation of the freeform surface. In the 2D simulations, the GBGI model reflected grain size effect as well as experimental observations. However, the GBGI model is much more efficient than the CPFE model, entailing it is more suitable for engineering issues.

5.4 Model application

5.4.1 Ductile fracture prediction combined with the GTN model

The GTN model was employed in an FEM simulation combined with the GBGI model to predict the ductile fracture behaviors in the plastic deformation of the RVE and 2D-plane tensile tests. The theoretical basis of the GTN model is illustrated in Section 2.3.5. The required parameters in simulations are summarized in **Table 5.5**.

Table 5.5 Parameters in the GTN model [81, 122].

$\bar{\varepsilon}_N$	S_N	f_c	f_f	f_0	f_N
0.3	0.1	0.028	0.135	0.002	0.032

The GTN model was employed in FEM simulations combined with the GBGI model to predict the ductile fracture behaviors in the plastic deformation of the RVE and 2D-plane tensile tests. The results are shown in **Fig. 5.14**. In **Fig. 5.14** (a), cracks mainly occur near the grain boundary region and elongate along the grain boundary direction, but there are still individual grains being crossed. In the GTN model, ductile fractures occur due to the initiation, growth, and coalescence of microvoids, which appear at the regions of grain boundaries and inclusions. That means that ductile fractures tend to occur at or near the location of grain boundaries. The simulation result with the combined model coincides with this knowledge. Furthermore, the result in **Fig. 5.14** (b) and (c) presents the inhomogeneous distribution of stress and strain. This result reveals that the grain boundaries carry larger stress compared with the grain interiors. The stress on the grain boundary region does not change considerably, but the stress in grain interiors varies widely among different grains.

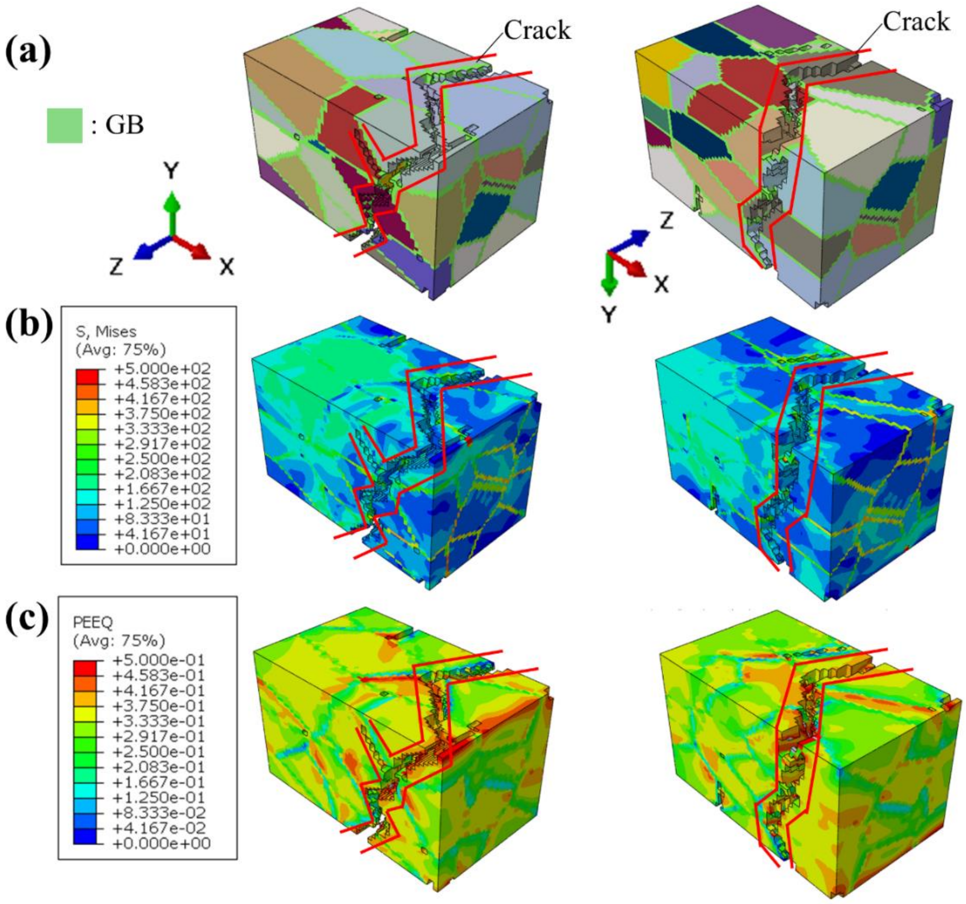

Fig. 5.14 Fracture of the RVE simulated using FEM. (a) Cracked model in the top and bottom views. (b) Mises stress and (c) equivalent plastic strain distributions when a fracture occurs.

The 2D simulations with different grain sizes were conducted to study fracture generation, as shown in **Fig. 5.15**. In a fine-grained material, as shown in **Fig. 5.15** (a), the crack grows inclinedly and tends to grow along the direction of grain boundaries. In a coarse-grained material, as shown in **Fig. 5.15** (b), the crack initiates at the grain boundary and extends laterally, and ultimately, a nearly horizontal crack is generated. As with the predicted deformation from the simulation, grain boundaries carry greater stress and less strain compared with the grain interiors. Once a crack initiates, the local stress at the same horizontal position drops, but the local strain at the fracture time remains. With the elongation of the crack, the overall response of stress is decreased until a fracture occurs.

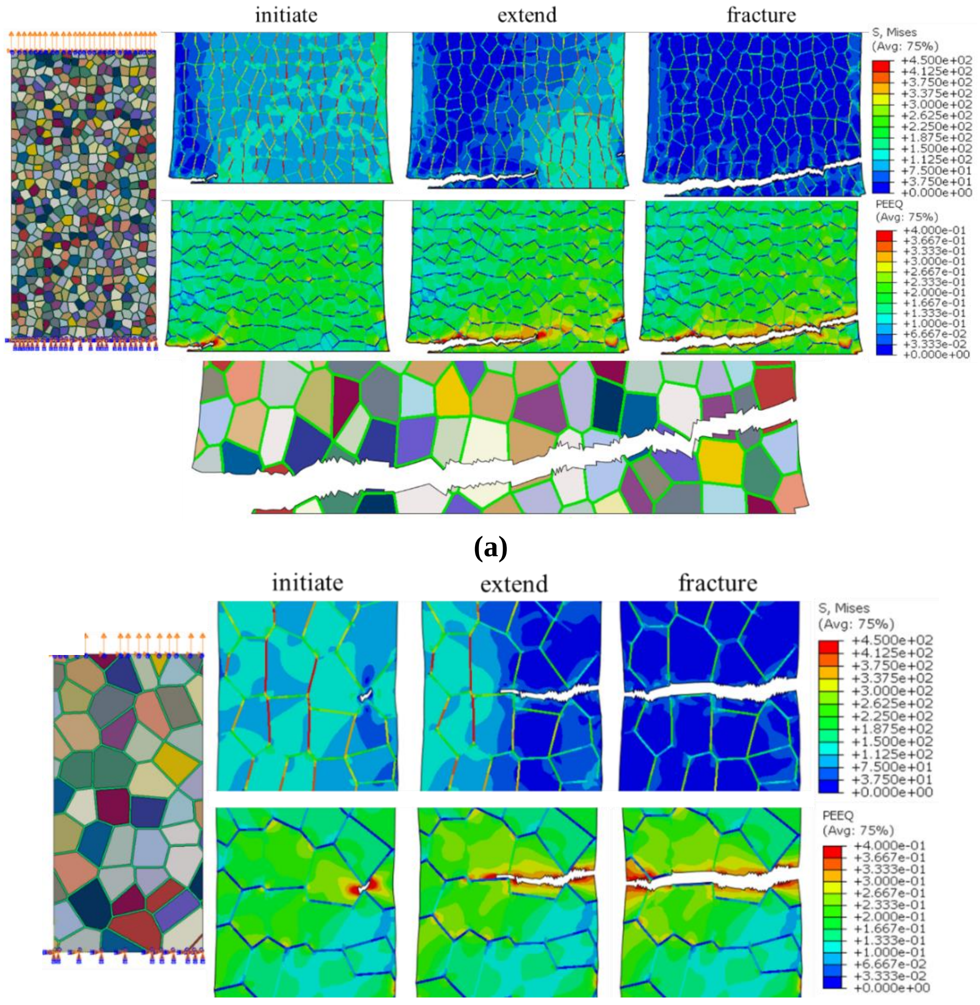

Fig. 5.15 Simulation of a ductile fracture generation in a material with grain sizes of (a) 60 µm and (b) 225 µm, illustrated by stress and strain distribution.

5.4.2 Application in meso-heading

In order to further explore the industrial application of the proposed GBGI model, a meso-heading process was established to compare with FEM simulations. The illustration of the specimens, experiment, and simulation of meso-heading is shown in **Fig. 5.16**. In the meso-heading, a pure-copper EDM-cut meso-cylinder was inserted into a cylindrical hole, and a 0.45-mm tall countersunk head was formed finally. The average grain sizes were about 90 and 300 μm in two scenarios. A quasi-static displacement of 0.01 mm/s was applied on the top surface to 0.9 mm. Machine oil was applied to reduce the friction, and for simulation, a friction coefficient of 0.1 was applied. The quarter with grains was constructed based on the 3D Voronoi method using Abaqus script. The symmetrical boundary conditions were applied on the X- and Y-planes. The GBGI model was combined with the GTN model to predict surface fractures.

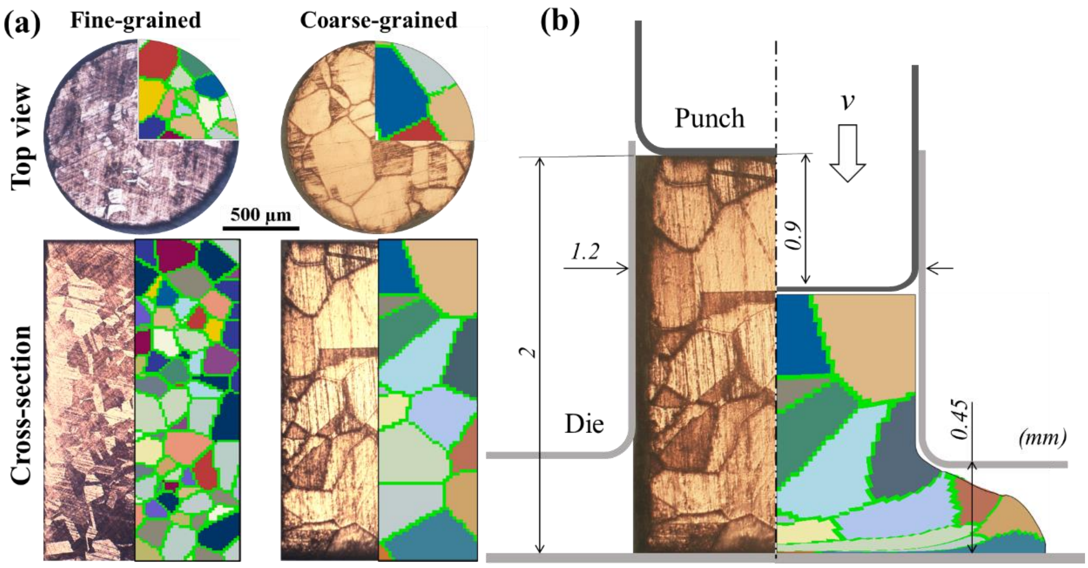

Fig. 5.16 (a) The pure copper specimens and (b) the illustration and tooling dimensions of the meso-heading process.

The FE results for the fine- and coarse-grained materials are illustrated in **Fig. 5.17**. It predicts that cracks prefer to generate at the bulge surface of the heading feature with an inclined shape connecting the top and bottom surface. The top surface of the heading feature shows uneven characteristics with coarse grains. Moreover, the strain distribution on the meso-headed part is non-uniform. From the cross-section view, the high strain initiated at the central-bottom area and elongated to the top surface of the heading feature with an inhomogeneous material flow. The high-strain area in fine-grained material was larger than it in coarse-grained material. On the other hand, the cracks in the fine-grained material were more numerous and slighter, while the cracks in the coarse-grained material were fewer and more pronounced. As the GBGI model predicts that crack will generate along the grain boundary, coarse-grained material should be less likely to crack, but the fracture deformation should accumulate along several cracks.

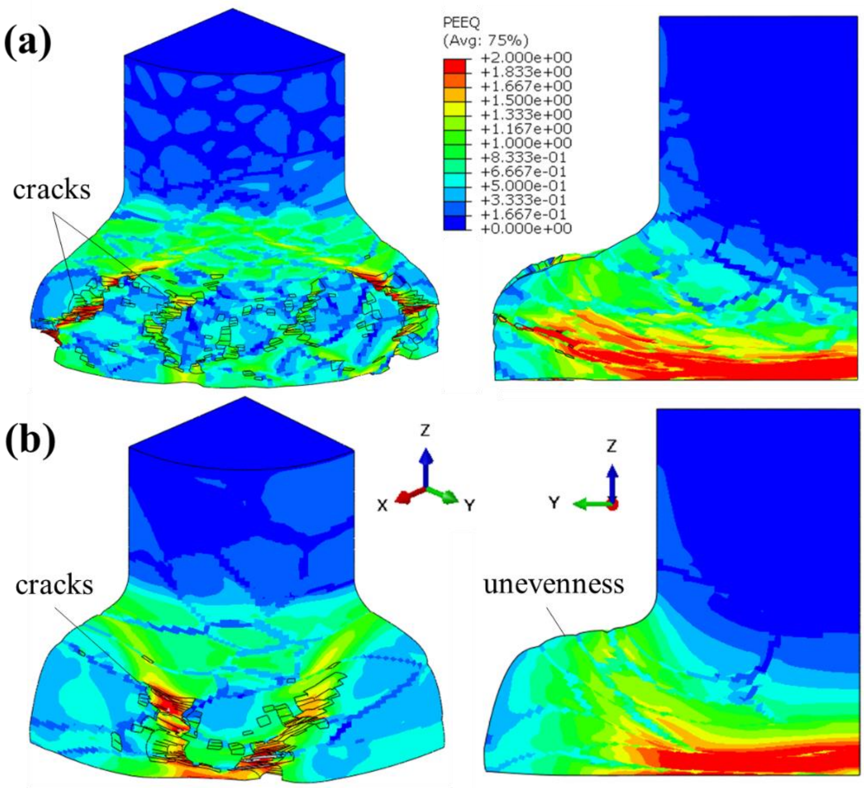

Fig. 5.17 Plastic strain distribution of the GBGI simulation and the crack generation: (a) fine-grained material; (b) coarse-grained material.

The surface morphologies of the meso-heading-formed parts with the fine-grained material were captured using a SEM, as shown in **Fig. 5.18**. Cracks are the major defects on the freeform surface and most of them were slight and short, but long deep cracks still manifested. These observations are consistent with the results of the GBGI simulation. By contrast, for the coarse-grained material, several different defects appear, as shown in **Fig. 5.19**. The crack on the bulge surface of the heading feature is wide and long, which generally corresponds with the simulation. There are also defects near the bottom edge, on the top surface of the heading feature, and the corner, which were not predicted by the simulation. The defects show different morphologies induced by various ductile fracture mechanisms. The proposed constitutive model is limited in that only one fracture model is included. This model can be improved with further investigation

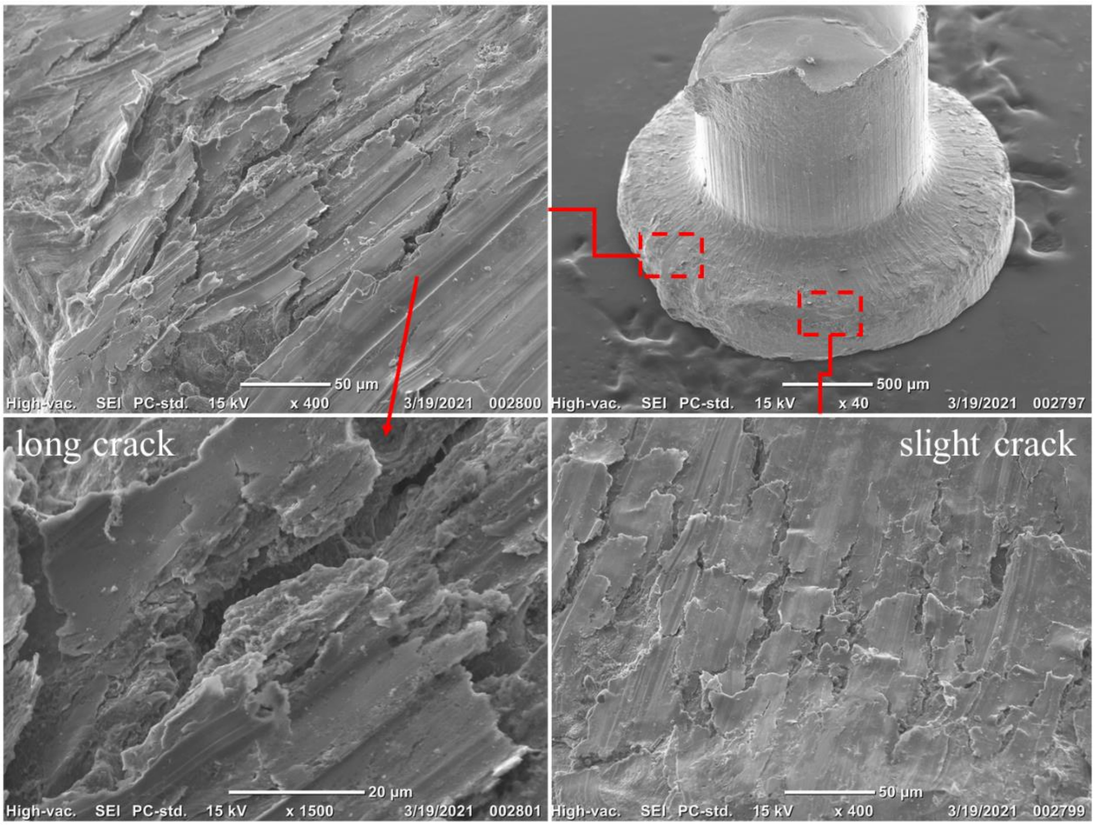

Fig. 5.18 SEM observation of the meso-heading-formed part with the fine-grained material.

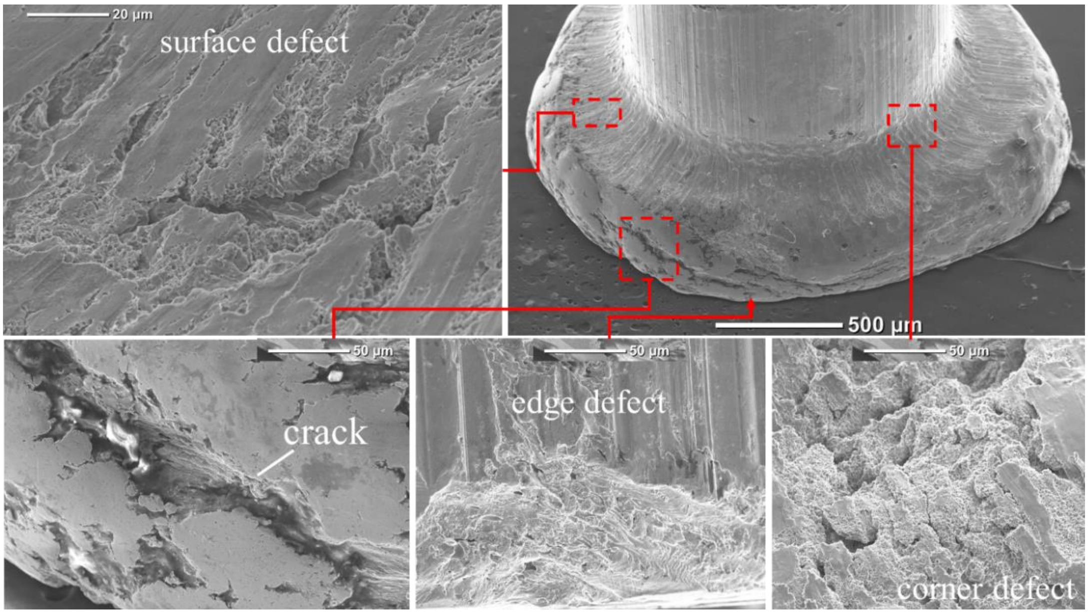

Fig. 5.19 SEM observation of the meso-heading-formed part with the coarse-graind material.

5.5 Summary

In this research, a constitutive model combining the surface layer model and the composite model considering the effect of initial grain orientations was proposed. Based on this model, a polycrystalline specimen is split into two portions, viz., grain boundary and grain interior portions. The grain boundary portion has isotropic properties, while the grain interior portion has different properties and thus inhomogeneous due to different orientations. FEM models based on the controlled Voronoi tessellation were developed to validate the proposed GBGI model through uniaxial tensile and compressive experiments. Meso-heading tests were conducted to study the proposed model's ability to predict ductile fractures. The following conclusions are drawn from this research:

1) The flow stress of polycrystalline metal is in part produced by the GB and GI portions through their fraction values. The fraction values of each portion are determined using a hexagonal structural model with the specimen thickness, grain

size, and the related grain boundary thickness. The average flow stresses of grain boundaries and grain interiors are evaluated by experimental data fitting methods. The flow stress of each grain interior is assessed using a randomly generated grain orientation factor in a value range. This proposed GBGI model shows it is consistent with experimental stress-strain curves of uniaxial tensile and compressive tests with different grain sizes and specimen thicknesses.

2) The proposed GBGI model is generally as capable as the CPFE model in predicting flow stress and inhomogeneous deformation but with much greater efficiency. The shapes of deformed cylinders predicted by the two models are different. However, the GBGI model is limited in predicting variation of freeform surface in meso-scaled compressed cylinders.

3) The GBGI model predicts well the formation of shear bands of compressed specimens with the grain size effect, where fine-grained material promotes a continuous and straight shear band, while coarse-grained material induces discontinuous short shear bands. Moreover, irregular shapes and random bulges occur on the coarse-grained compressed specimens, which is consistent with experimental observations.

4) The GBGI model combined with the GTN model can feasibly predict ductile fractures in micro-scaled uniaxial tensile tests and meso-heading processes via FE simulations. The cracks initiate at grain boundaries and gradually elongate along grain boundaries in an inclined direction. In meso-heading processes, cracks on the heading feature for fine-grained material are more numerous and slighter, while for coarse-grained material they are fewer and more pronounced with appearance of other defects.

Chapter 6 Simulation-assisted prediction and avoidance of folding defects in multi-scaled forming

6.1 Introduction

Ductile-metal bulk forming is a desirable manufacturing technology used to produce components based on metallic plastic deformation since it has many attractive advantages, such as high productivity, efficient material utilization, acceptable part quality, the ability to form complex shapes, and low production costs [123]. Bulk-formed metallic parts generally require high dimensional precision and a defect-free surface to be assembled with other components directly. However, due to the severe plastic deformation and complex material flows during forming processes and imperfect tooling, forming defects are common in bulk forming processes and include cracks, surface defects, form defects, shear defects, structural defects, and folding [44].

In metal forming, folding is one of the most serious flow-induced defects that can greatly influence the quality of parts and can be hardly eliminated by subsequent processes. However, folding can be adequately avoided by controlling the material flows and optimizing the design of tooling and processes. Investigating the formation and mechanism of folding is important for predicting and avoiding it, which will improve the quality of final parts made through bulk metal forming.

With product miniaturization, metal-forming technologies are transferred and applied in scaled-down production. However, the knowledge and experience from the macroscale are not directly applicable at the meso/microscale due to size effects. Research on the mechanisms of flow-induced defects in meso/microforming is limited. This study investigated the mechanism of folding defects based on material flow behaviors, and four improved forming processes were proposed following numerical simulations that avoid the formation of folding defects in an axisymmetric multi-stage flanged part. Following an analysis of material flows and the distribution of stress and strain and a comparison of the load-stroke curves of the proposed cases, the best design was selected and studied via physical experiments in relation to the one-stroke forming, and the experimental results were consistent with the simulation results.

6.2 Folding defects in metal forming

6.2.1 Formation mechanism of folding defects

Common axisymmetric bulk parts can be classified into hollow and solid types according to whether they have a central hole or not. **Fig. 6.1** illustrates the formation of two types of folding in hollow and solid parts. Folding is a typical defect in compressive deformation in forming of axisymmetric hollow bulk parts, as shown in **Fig. 6.1** (a). During ring compression, material generally flows in multi-directions and outward against the central axis. But due to the constraints, viz., friction and die cavity, the material flow near the contact surface with punch is usually hysteretic. There are thus uneven material flows that easily induce the flow turbulence and undesirable flow merging to form the folding on the inner surface. This type of folding is named as flow-induced folding. To avoid this folding in hollow parts, the laterally constrained material flow is needed. However, a diameter-flexible constraint on the lateral surface of axisymmetric parts is impossible. By contrast, for forming of solid parts, flow-induced folding is uncommon, but another folding type remains, which is named as structure-induced folding, as shown in **Fig. 6.1** (b). If a bulk part has a concave lateral profile, such as conner, groove, and stepped feature on the material cylindrical surface, the concave feature will have a chance to be closed via the merging of material flows from top down and bottom up in upsetting process. By analyzing the forming mechanisms of folding, an efficient and economical way for folding avoidance is to improve the tooling and process design to tailor and control the material flows in deformation process.

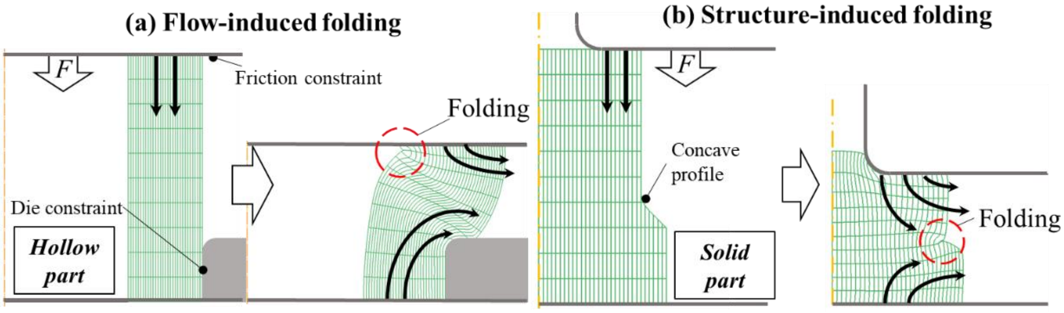

Fig. 6.1 Folding defects in axisymmetric metal forming: (a) Flow-induced folding caused by the uneven lateral material flows; (b) Structure-induced folding induced by the concave profile on the preform.

The incoordinate lateral material flow during upsetting is the major cause of the localized material flows in hollow axisymmetric parts. To investigate this effect, ring upsetting simulations with different interfacial friction were established, as shown in **Fig. 6.2**. When the interfaces are both frictionless, as shown in **Fig. 6.2** (a), the billet deforms evenly, and no folding or curved surface occurs. When the friction factor is 0.1 as a well lubricated condition, as shown in **Fig. 6.2** (b), the inner surface is slightly curved but no folding occurs. However, in dry conditions with a friction factor of 0.7, as shown in **Fig. 6.2** (c), the inner surface is fluctuant, and the middle area is thus potential to be folded. Moreover, when the lubrication on the two interfaces is different, as shown in **Fig. 6.2** (d), folding more easily occurs near the lubricated die. Therefore, in hollow part upsetting process, poor and different interfacial lubrication of top and bottom dies should be avoided.

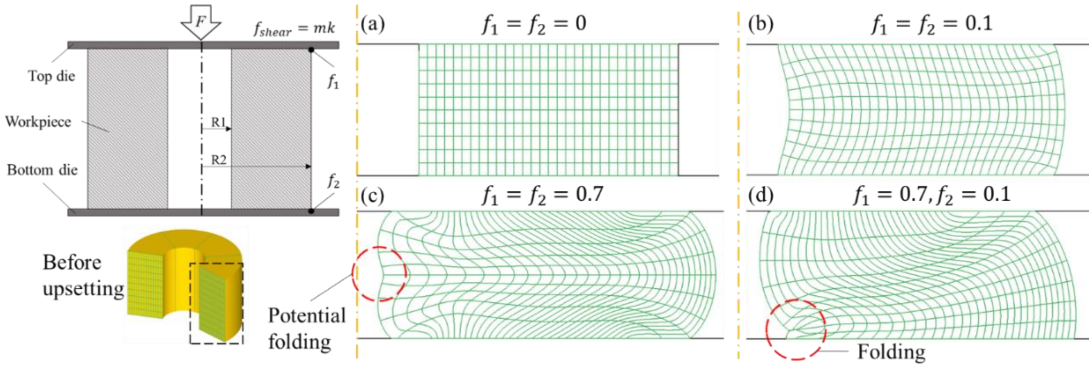

Fig. 6.2 The influence of friction on folding defects of ring upsetting with different friction factors on the interface of top die and bottom die.

6.2.2 Folding formation in axisymmetric flanged forming

Multi-stage flanged parts at three different scales were studied using cold metal-forming processes to investigate the formation of folding defects and how to avoid them. The formed parts are shown in **Fig. 6.3** (a). The design of parts is illustrated in **Fig. 6.3** (b), and it is identified by three features based on the geometrical shape, where feature A is the peak outer ring formed by backward extrusion, feature B is the shouldered plate forged and extruded from cylindrical billets, and feature C is the central hole feature formed by punch extrusion. The detailed dimensions of the flanged part at the three scales are shown in **Table 6.1**. The three scales are identified by the "scale factor" to show their multiplied relationship. According to their dimensional ranges, "1" represents the microscale, "2" represents the mesoscale, and "4" represents the macroscale.

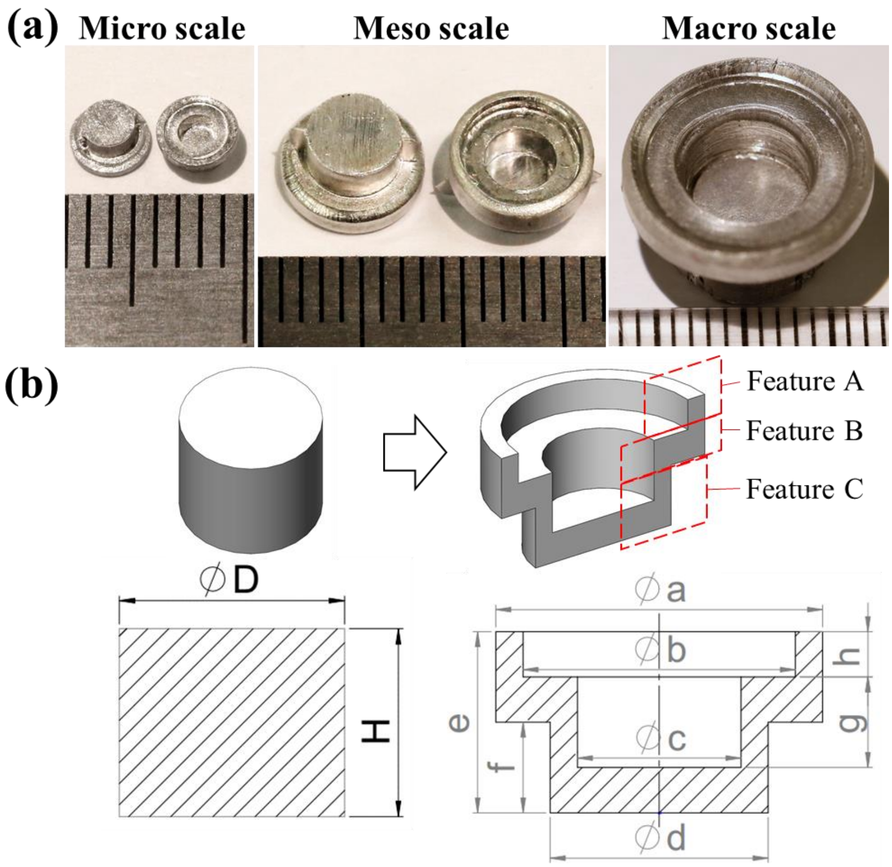

Fig. 6.3 (a) The multi-stage flanged parts at different scales and (b) the design of specimens and parts with three features.

Table 6.1 Dimensions of parts at three scales.

	Dimensions (mm)									
Scale factor	**D**	**H**	**a**	**b**	**c**	**d**	**e**	**f**	**g**	**h**
1 (Micro)	2.4	1.8	3.6	3	1.8	2.4	2	1	1	0.35
2 (Meso)	4.8	3.6	7.2	6	3.6	4.8	4	2	2	0.7
4 (Macro)	9.6	7.2	14.4	12	7.2	9.6	8	4	4	1.4

In conventional one-stroke forming processes, folding is one of the common flow-induced defects of axisymmetric parts and is especially due to the multi-extrusion caused by stepped punches and dies. **Fig. 6.2** presents a conventional forming process for the multi-stage flanged parts. Generally, the punch and die used in this process are designed based on the shape of the inner and outer profiles of the part to form it in one stroke. As shown in **Fig. 6.4** (a), one-stroke forming is divided into backward extrusion and forging stages, and folding appears at the forging stage. **Fig. 6.4** (b) presents the material flow chart at the stage of forging. At this stage, the moving punch has two regions pushing the material so that it flows, and they are on the tip and the shoulder of the punch. The first contact is where the punch pin pushes the material so that it flows backward along the die surface. The flow lines are separated into two directions near the die edge. The major flow direction is still backward, and the minor direction is lateral. By contrast, the second contact is located at the position where the punch shoulder pushes the backward-flowing material in two directions as it is sufficiently extruded. The two nearly opposite inward flows contact and form a serious folding defect, as shown in **Fig. 6.4** (a). The two outward material flows merge from different directions, but no folding happens at the joint.

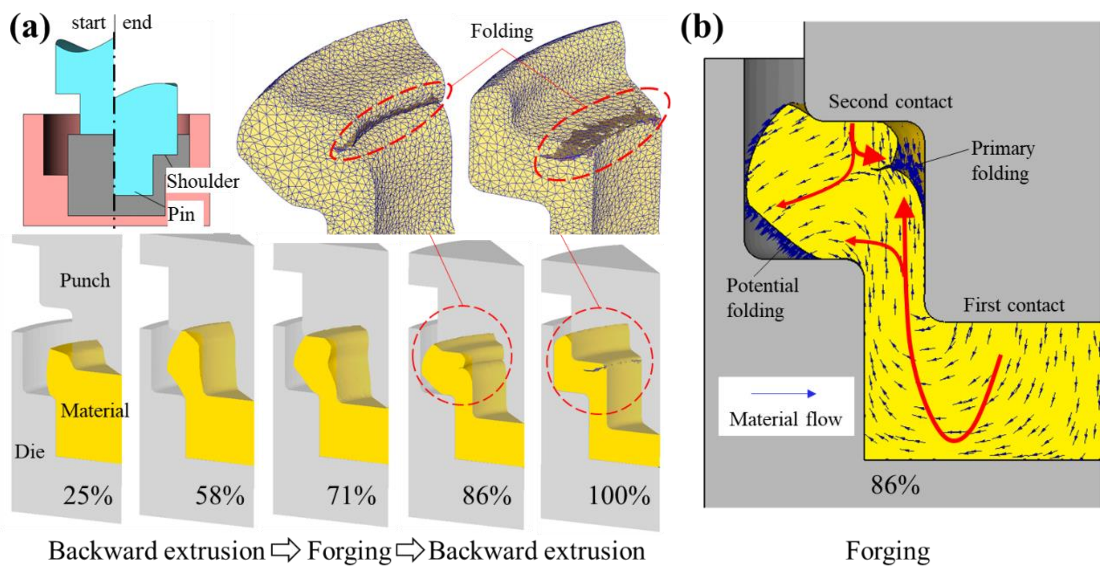

Fig. 6.4 (a) The folding formation process in one-stroke flanged forming. (b) The material flow chart at the 80% stroke.

The flow-induced folding defects are easily observed in the one-stroke formed parts at all three scales, as shown in **Fig. 6.5**. The figure shows that the location of the folding defect is near the edge of the inner surface of feature B in experiments, which is consistent with the simulations shown in **Fig. 6.4**.

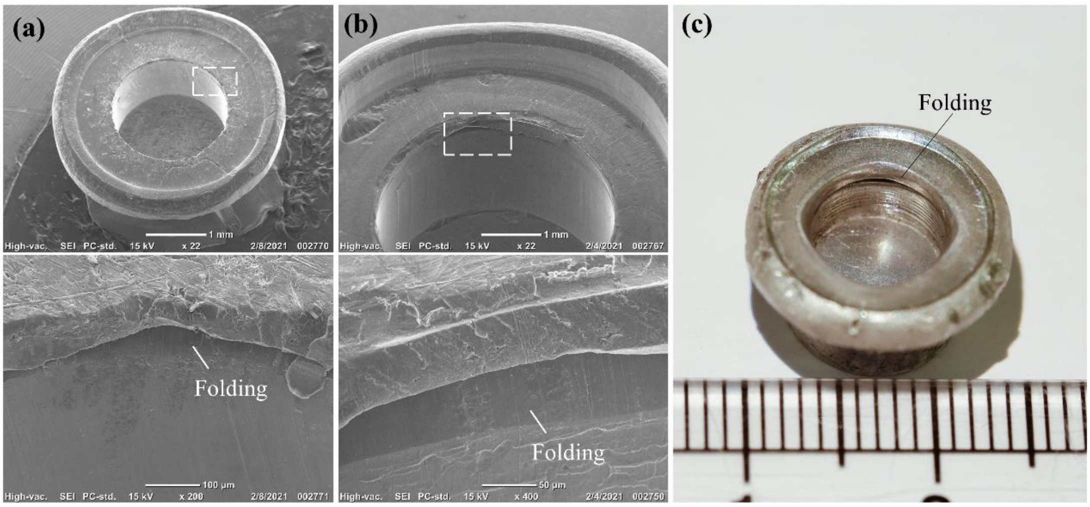

Fig. 6.5 Folding defects in the flanged (a) micro-, (b) meso- and (c) macro-scaled parts caused by the one-stroke forming process.

6.3 Folding-free designs

The numerical and experimental studies on one-stroke flanged forming reveal that the folding defects are primarily caused by the intersection of material flows from opposite directions during the forming processes. Thus, one feasible approach for avoiding folding is to avoid opposite material flows. This section will list some tooling and process designs for improving the material flows during flanged forming. Their illustrations are shown in **Fig. 6.4**.

6.3.1 Case 1

This case used a stepped punch with a shortened pin to avoid folding. With the punch stroking, a part of feature C and the whole of feature B were formed. After this forming, the punch was replaced by a hollow holder with a movable insert. By moving the insert, feature A and the left feature of C were formed.

6.3.2 Case 2

This case first used a flat punch to forge the cylindrical specimen into a plug shape. Feature B was partially formed. Then, the plat punch was replaced by a fixed punch with a movable insert, and the insert punched downward for extrusion. Feature A and C were formed simultaneously.

6.3.3 Case 3

This case employed a flat punch and a flat movable die inserted in a hollow die. The movable die was fixed first and the flat punch compressed the cylindrical billet. Features A and B were formed after forging and backward extrusion deformations. Thereafter, the flat punch was replaced by a hollow holder with a movable insert. The movable insert punches downward and the flat movable die moved down at a relative speed with the insert. Feature C was formed after the metal drawing operation.

6.3.4 Case 4

This case applied a die with a spring-supported sliding insert. The sliding insert raised the position of material separation to avoid the folding of the bulk material. When the punch shoulder contacted the material, the sliding insert was pushed down to the designed strokes. Features A and B were mixed as one bulk of the shoulder of part. Thereafter, the punch was replaced by a punch with a thinner shoulder. With the punch moving, features A and B were formed from one bulk.

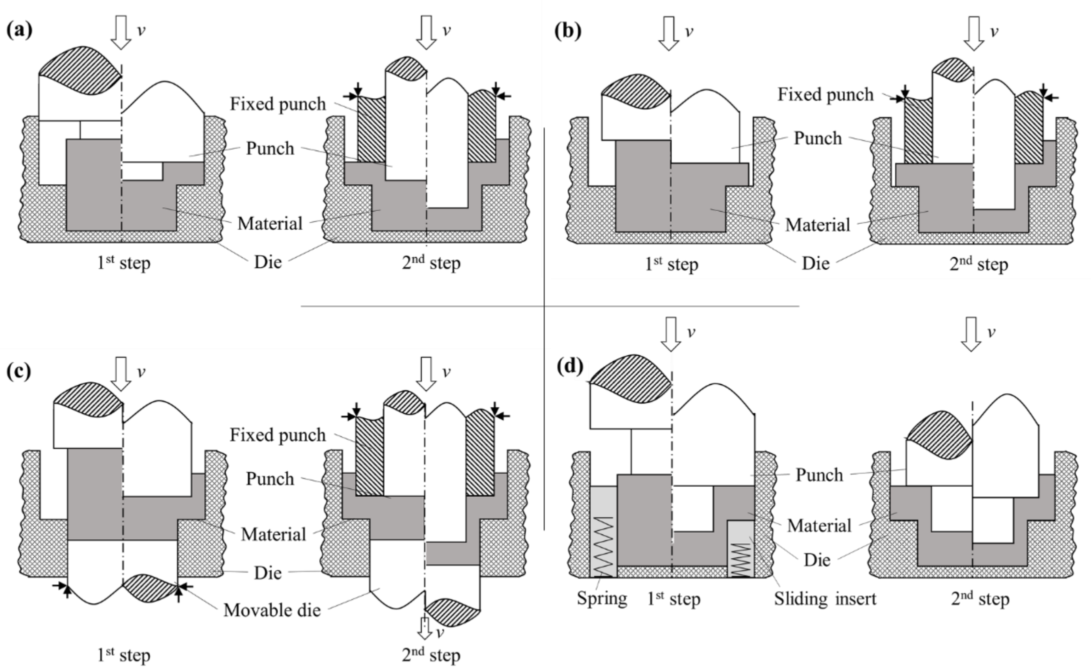

Fig. 6.6 Improved two-step multi-flanged forming processes: (a) Case 1: shorten-pin design; (b) Case 2: flat-punch design; (c) Case 3: movable-die design; (d) Case 4: sliding-insert design.

6.4 Experimental and numerical evaluations

6.4.1 Experimental material and its properties

Aluminum alloy AL1060 (Al ≥ 99.60%) was used as the experimental material in this study due to its excellent ductility and homogeneous textures. The material was annealed at 400 ℃ for 1 hour under an argon-filled furnace to release the work hardening and then gradually cooled down to room temperature. To obtain the mechanical properties of AL1060, uniaxial tensile tests were conducted at room temperature using an MTS testing machine with a 10-kN capacity load cell. Dog-bone-shaped tensile specimens were used and repeated four times. The strain rate was 0.01 s^{-1}. Thus, the rat effect could be ignored. The dimensions of specimens and the flow stress curves are shown in **Fig. 6.7**.

The Swift model [34] is a well-known empirical model used to describe the flow stress of materials and is generalized in a power-law shape as follows:

$$\sigma = C(m + \varepsilon)^n \tag{6.1}$$

where σ is flow stress, ε is plastic strain, and C, m, and n are empirical constants fitted from experimental data. The parameters and mechanical properties are summarized in **Table 6.2**. The model is employed in simulations to describe the mechanical responses of material.

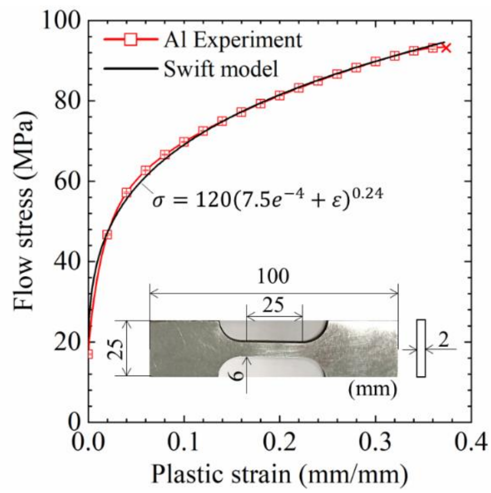

Fig. 6.7 Flow stress of the tested aluminum alloy.

Table 6.2 Mechanical properties of the annealed aluminum alloy AL1060.

AL1060 properties			Swift model		
Young's modulus	Poisson's ratio	Yield stress	***C***	***m***	***n***
69 GPa	0.33	17 MPa	120 MPa	7.5×10^{-4}	0.24

6.4.2 Development of multi-scaled forming systems

To comprehensively evaluate the feasibility of the four proposed designs in Section 2.2, simulation-enabled studies of the four forming processes were conducted on the DEFORM platform. According to the simulation results, the tooling sets that could realize both the conventional one-stroke forming and the two-step forming of Case 2 were designed and developed, as shown in **Fig. 6.8** (a). The punch contains a sleeve and a pin, and the gasket was used to shift its relative position to realize the required process. Regarding the one-stroke forming, the punch pin bottomed out of the sleeve to create a stepped punch, as shown in **Fig. 6.8** (b). In the first step of the two-step forming process, the gasket was used to make the pin, and the sleeve created a flat punch. Then, the gasket was taken out, the sleeve was fixed, and the pin punched as in the second step, as shown in **Fig. 6.8** (c). Regarding the simulation, the one-eighth billet with the 40,000 tetra mesh was used with symmetrical boundary conditions. The shear friction model with a coefficient of 0.4 was applied to describe the friction between aluminum and steel tooling. **Fig. 6.8** (d) presents the simulation setting of Case 2.

The manufactured tooling sets are shown in **Fig. 6.9**. The multi-scaled flanged forming experiments were conducted to investigate the geometrical size effect on the formation and avoidance of folding defects. An MTS test machine with a load cell of 50 kN was used. The stroke velocity of the crosshead was 0.01 mm/s to avoid the influence of the strain rate. Separated dies and die holders were applied for easier demolding. The separated dies and punch guider were inserted into the die holder and fixed by the platform. Considering the material loss due to the gaps between tooling, the billets with the dimensions of $\emptyset 2.4 \times 2$, $\emptyset 4.8 \times 4$, and $\emptyset 9.6 \times 8$ mm were prepared. All the interfaces were lubricated using machine oil to reduce friction.

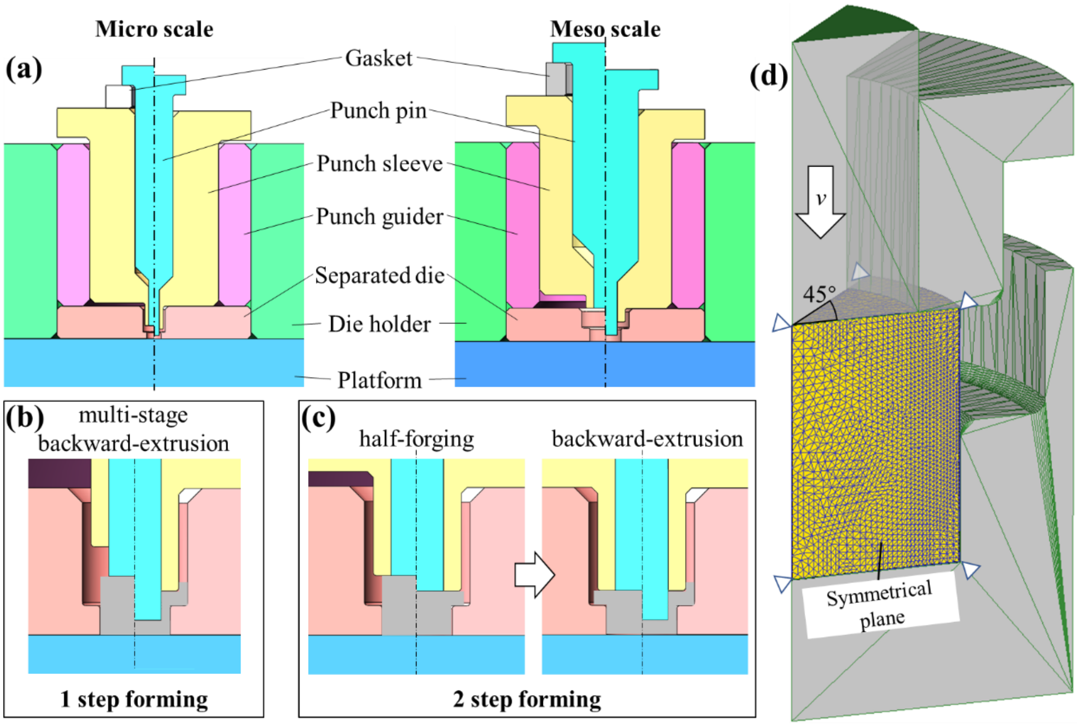

Fig. 6.8 (a) The tooling structures of the multi-scaled forming system. (b) The forming illustration of the original one-stroke process. (c) The forming illustration of the two-step process of Case 2. (d) The simulation setting of Case 2.

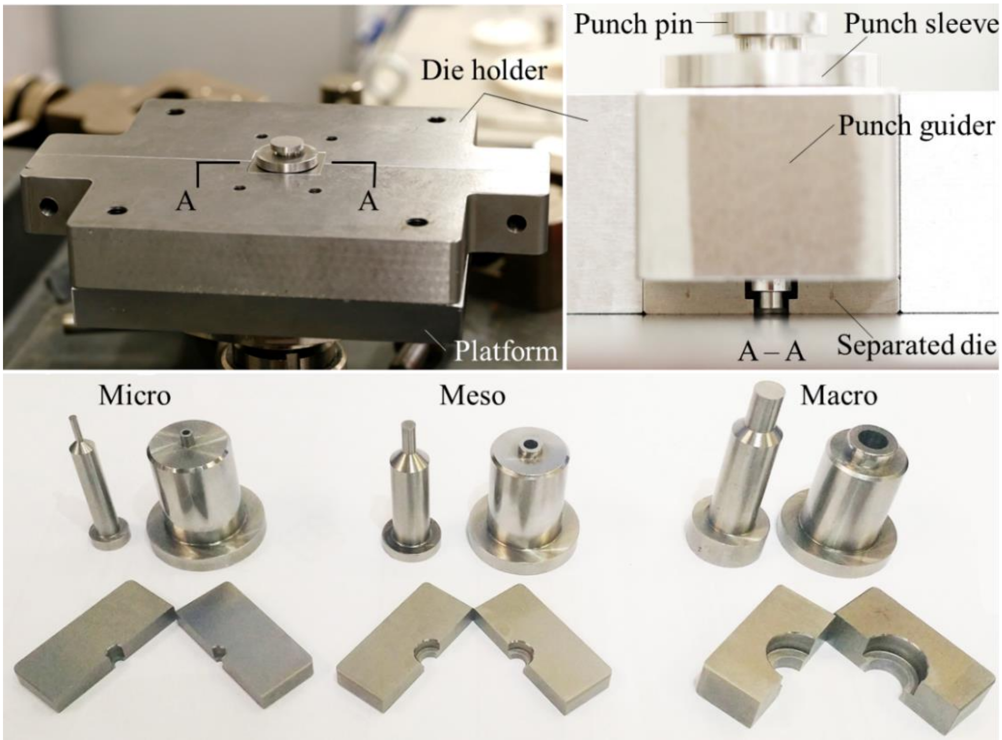

Fig. 6.9 The tooling of the multi-scaled forming system.

6.5 Results and discussion

6.5.1 Forming process analysis

The normalized load-stroke curves at the three scales for the one-stroke multi-stage flanged forming are presented in **Fig. 6.10**. Among different size-scaled forming processes, the normalized load is defined as the current load divided by the square of their relative scale factor, and the normalized stroke is defined as the current stroke divided by the relative scale factor:

$$Normalized\ load = \frac{Load}{Scale\ factor^2},\quad Normalized\ stroke = \frac{Stroke}{Scale\ factor} \quad (6.2)$$

Fig. 6.10 shows that the entire forming process can be divided into three stages. In the first stage, the punch pin pressed the upper surface of the billet, and the upper half of billet began to be extruded backward without lateral constraints. When the extruded material contacted the punch shoulder, the second stage began. The material was continuously extruded backward by the punch pin and then forged laterally by the punch shoulder. The flow-induced folding was formed during this stage due to the bending of the extrudate. Since the contact area between the punch and the material increased, the normalized force rose rapidly. When the forged material reached the inner cylindrical surface of the die, the third stage started. The material was extruded by both the pin and the shoulder of the punch and flowed backward to form feature A. The third stage ended with the punch reaching the designed stroke.

The normalized load-stroke curves showed similar trends at different scales, but the meso-scaled curve has the maximum load. The curves for the microscale and macroscale are close to the mesoscale curve until the third stage. According to surface grain theory [40], the grains located on the surface of the billet show lower strength, so the flow stress of a specimen decreases with a decrease in specimen size. By contrast, due to the effects of open and closed pockets [20] on the lubricated interfaces, a larger surface area induces a better lubrication condition and a lower forming load. From their mathematic relationship, the fraction of surface grain is related to the scale factor, while the surface area is related to the square of the scale factor. Therefore, from the mesoscale to the macroscale, the lubrication condition takes the larger part of the forming load, and the forming load decreases.

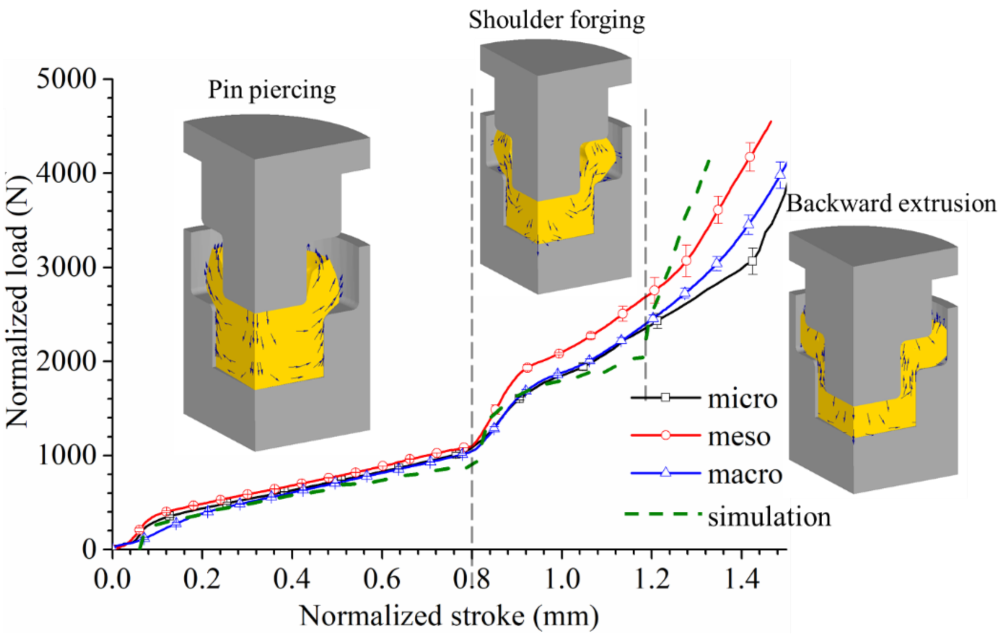

Fig. 6.10 Normalized load-stroke curves of the three scaled forming processes and simulations.

The load-stroke relationship in the deformation process of Case 1 is shown in **Fig. 6.11**. The total stroke is 1.3 mm, where the first step is 0.87 mm and the second one is 0.43 mm. For the first step, the punch pin was shortened from 1 mm to 0.57 mm following the volume constant principle. The material was pushed to flow upward and then laterally once the material contacted the shoulder of the punch. Thus, the forming load suddenly increased. When the material contacted the inner surface of the die, the material reflowed to fill the unfilled space between the punch and the die, which resulted in a sharply increased forming load. Then, the second forming step began. The punch was replaced by a holder with a gap between the die surface and an insert punch. The insert punch pushed the material to flow backward to form feature A until the punch reached the designed position, and the maximum forming load of 4,430 N was obtained.

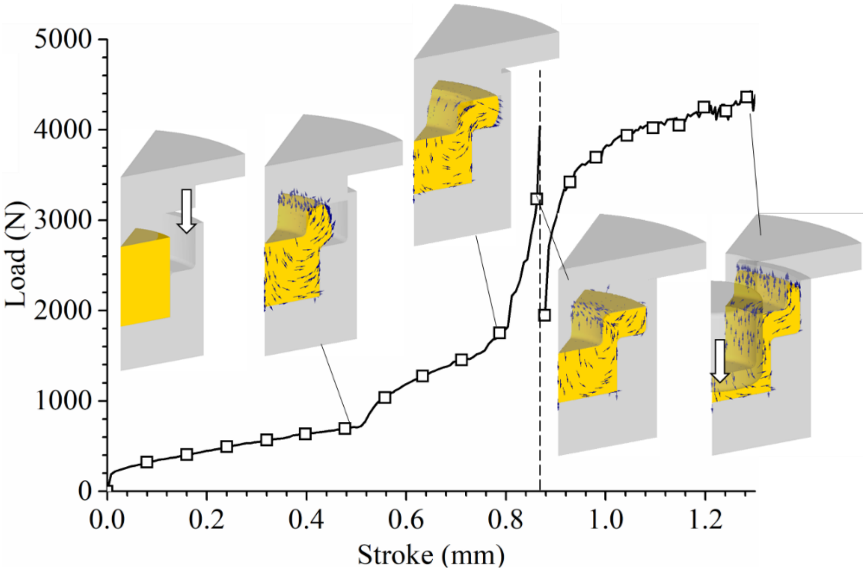

Fig. 6.11 Load-stroke curves of the simulation of Case 1.

The normalized load and stroke curves of the two-step deformation process of Case 2 in experiments and simulations are presented in **Fig. 6.12**. The entire stroke is 1.3 mm, with 0.3 mm for forging and 1 mm for backward extrusion. The punch is comprised of a holder and an insert. For the first step, the holder and the insert moved synchronously to compress the upper half of the billet. Once the first step finished, the holder was fixed and the insert continuously pressed the material for extrusion. The material first flowed laterally and then flows upward along the gap between the holder and the die. At the stage of upward flow, the simulation results were clearly different than the experimental results. Since there were only several grains in the microfeature, an increasing fraction of surface grains should induce a decrease in material strength according to the surface grains theory, which further results in the reduction of the deformation load. However, the size effect was not reflected in the simulation, which caused the difference from simulations to experiments. With an increase in the work hardening, the experimental results increased and reached the simulation curve.

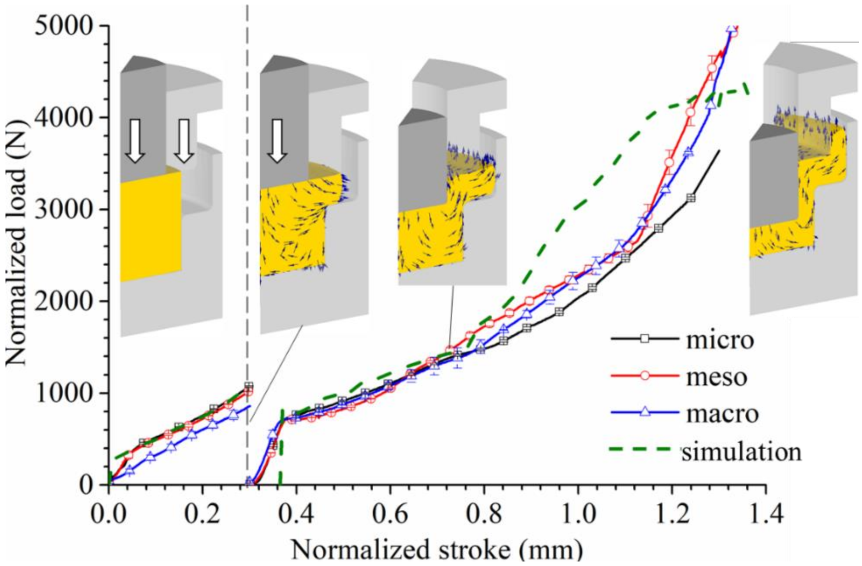

Fig. 6.12 Normalized load-stroke curves of experiments and the simulation of Case 2

The load-stroke curves of the deformation process in the simulation of Case 3 are illustrated in **Fig. 6.13**. The whole stroke is 1.8625 mm and divided into two steps, with the first step being a forging-backward extrusion step with a stroke of 0.8625 mm and the other step being a drawing step with a stroke of 1 mm. In the first step, the load was first increased gradually with punch stroking. A small part of the specimen was fixed using the hollow die, and the other part was forged and bulged by the flat punch. Once the material contacted the die surface, the material flowed backward along the gap between the punch and the die, which resulted in a suddenly increasing load. When the punch reached the designed position, the maximum load was obtained, which was 3,114 N. In the second step, the flat punch was replaced by a holder and a punch insert. The second step was a metal drawing process, where the die insert was no longer fixed but moved with the movement of the punch insert. The deformation load in this step was steady until the desired feature was formed.

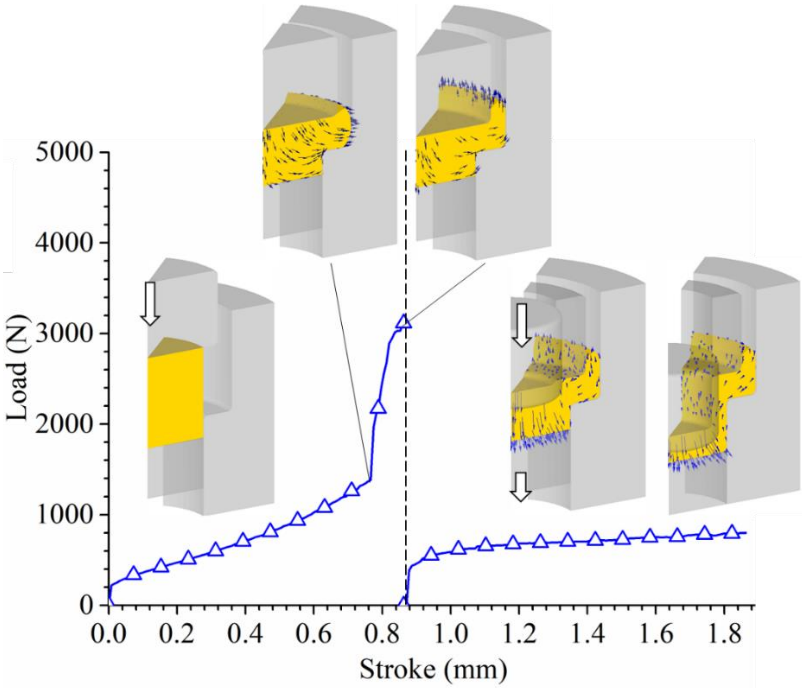

Fig. 6.13 Load-stroke curves of the simulation of Case 3.

The load-stroke curves and the stroke of the slider during the forming process in the simulation of Case 4 are shown in **Fig. 6.14**. The stroke was 1.3 mm in total, with 1.16 mm for slider-assisted extrusion and 0.14 mm for backward extrusion. Initially, the specimen was compressed by the punch pin and flowed upward. When the material contacted the shoulder of the punch, the gap between the slider and the shoulder of the punch was approximately equal to or slightly smaller than the thickness of the extrudate to avoid the occurrence of folding defects. The extrudate was then extruded into the gap, and the load was rapidly increased due to the increased contact area. Meanwhile, the slider moved down gradually with the extrusion. The gap was filled by the material, and then the filler of the gap expanded until its thickness reached the designated value. Thereafter, the punch was changed to a thinner stepped punch, which pushed the material to form feature A, and the slider reached the maximum stroke. The maximum load was 4,940 N.

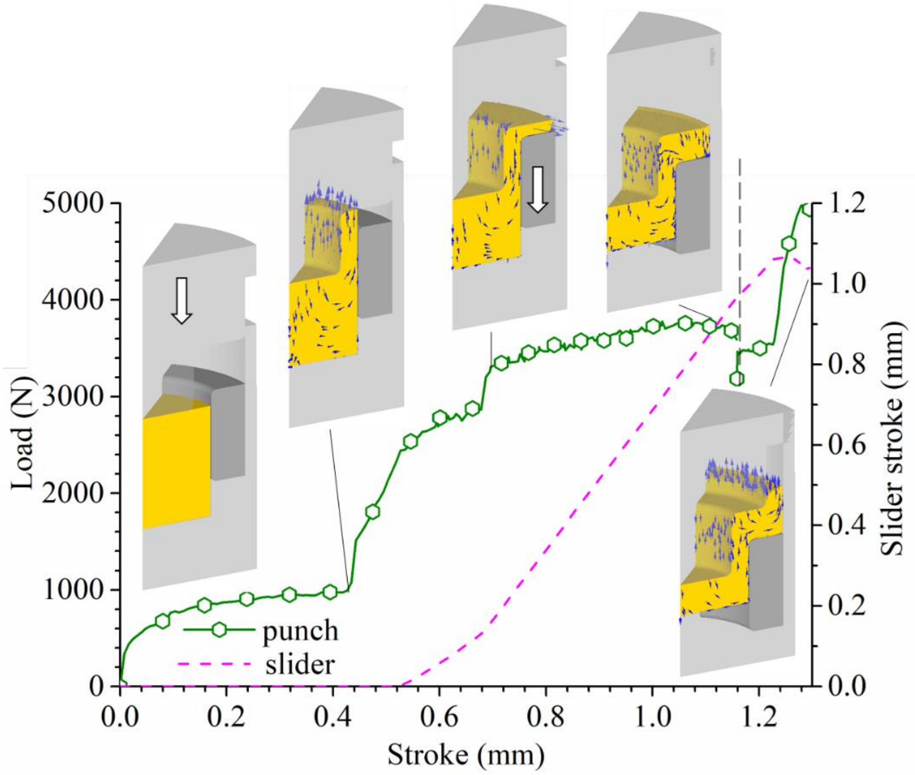

Fig. 6.14 Load-stroke curves and the slider stroke of the simulation of Case 4.

To quantitively evaluate the efficiency and energy consumption of the four cases, the comparison of energy, maximum load, and total stroke during the forming processes are illustrated in **Fig. 6.15**. **Fig. 6.15** (a) reveals that Case 3 had the lowest consumed energy and maximum load, which means it is economic and requires less equipment. Meanwhile, Case 1 and Case 2 had similar energy consumption and maximum load values due to their similar deformation processes. Case 4 had the largest energy consumption and maximum load, which is due to the application of the sliding die. The spring of the sliding die stores amounts of energy as elastic potential energy and increases the punching load. Case 3 had the longest total stroke, as shown in **Fig. 6.15** (b). This means that Case 3 required more time to form a final part with the same forming rate, which resulted in lower efficiency.

In summary, Case 2 and Case 3 are both desirable processes for the two-step forming of the multi-stage flanged part. With respect to energy consumption and equipment requirements, Case 3 is more desirable. With respect to production efficiency, Case 2 is more desirable.

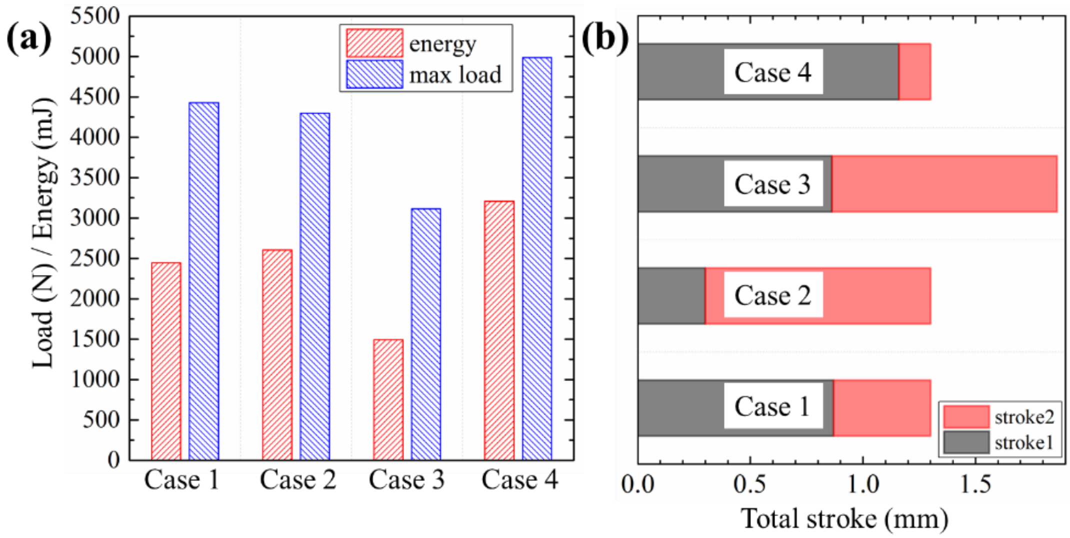

Fig. 6.15 (a) The consumed energy and maximum load during the forming process of Cases 1 through 4. (b) The total and separated strokes of Cases 1 through 4.

6.5.2 Forming quality of final parts

In this section, the qualities of the final parts in the simulations of the different cases are evaluated according to stress and strain distributions and freeform dimensions. A desirable design should consider many aspects, such as lower forming load and stroke, desirable geometry of formed part, and no much strain concentration.

The effective strain distributions of the final parts in the four cases are illustrated in **Fig. 6.16**. The figure shows that the large strain area is generally concentrated on the inner hole. In Case 1, however, a large strain band appears on the upper half of the inner hole, and in Case 4, shear bands appear on the upper half of the inner hole and the inner surface of feature A. High strain generally means severe deformation, which increases the possibility of fracture. In addition, Case 1 cannot fully avoid folding defects, as shown in **Fig. 6.16** (a). When at the 65% stroke, the material was pushed to flow back, causing the intersection of material flow, and then the folding defect was formed. By contrast, the bottom edge of the parts in Case 3 shows a different geometry from the bottom edge in other cases, as shown in **Fig. 6.16** (e). The part in Case 3 shows a curve edge induced by the metal drawing process. In the other cases, the material was pushed to fill the cavity of the die to form a square edge, and the strain was concentrated on it.

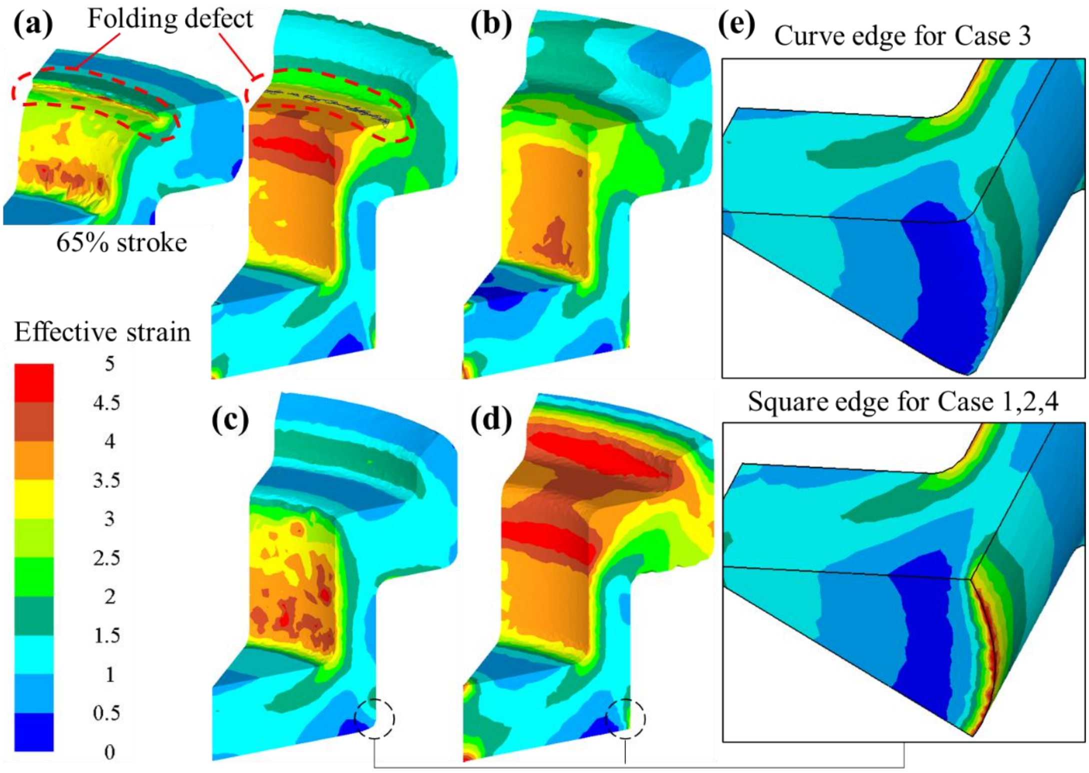

Fig. 6.16 Effective strain distribution in the simulation results of (a–d) Cases 1 through 4; (e) different shapes of the bottom edge.

To investigate the forming mechanism of folding defects in Case 1, the punches with variable pin lengths were used to conduct simulations. The results are shown in **Fig. 6.17**. The flow pattern illustrates the material flow behaviors when the first stroke nearly finished. The figure shows that the material was pushed by a punch pin to flow into lateral and upward directions to fill the cavities, and the material compressed by the punch shoulder tended to flow laterally. The cavity of the die was first filled, and then the material was pushed to fill the cavity of the corner of the punch pin and the shoulder. The folding defect occurred while the material filled the punch cavity. Changing the length of pin changed the geometries of the material during filling. The cavity of the punch was in a right triangular shape, and the hypotenuse is generally curved. Due to the interfacial friction between the material and the punch, the material at the punch shoulder had a tendency to stick. However, the material near the punch pin tended to flow inward, while the material near the punch shoulder tended to flow laterally. The dip angle θ decreased as the length of the punch pin increased. The two flow tendencies were separated gradually, which increases the likelihood of a folding defect when *m/n* is over a critical point. When *m/n* was larger than 55%, the folding defects appeared.

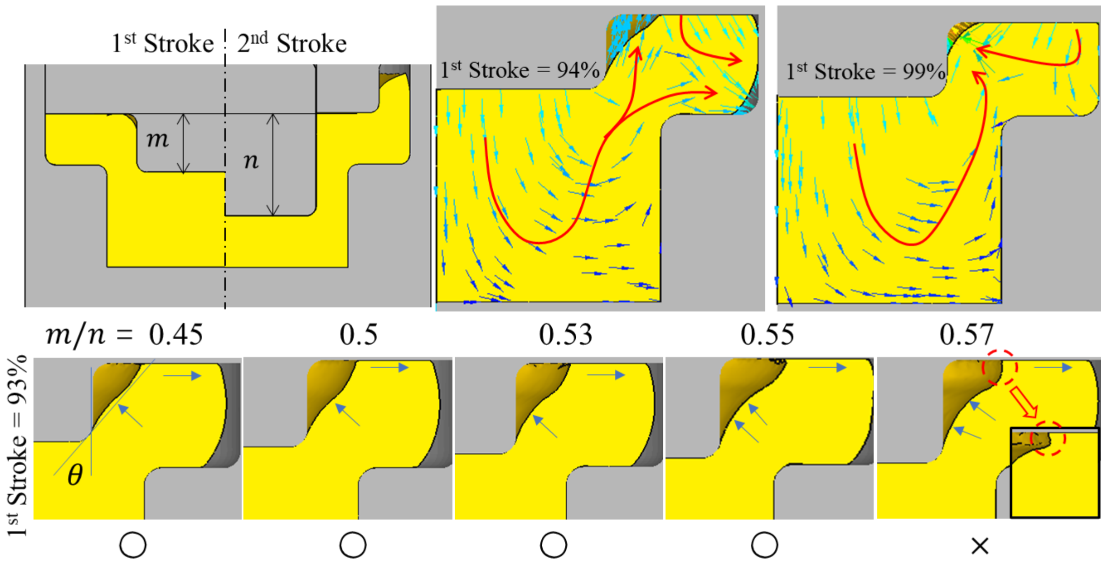

Fig. 6.17 The formation of the folding defect in Case 1.

The distributions of effective stress after the first and second strokes of the different cases are shown in **Fig. 6.18**. The figure shows that Case 4 has a large area of high stress due to the reactive force of the sliding die. Case 1 had the second-highest amount of stress. Cases 2 and 3 have relatively desirable stress distributions. In Case 3, since the sliding insert is unfixed after the first stroke, the stress on features A and B is released, so the stress on these features of the final parts is very low.

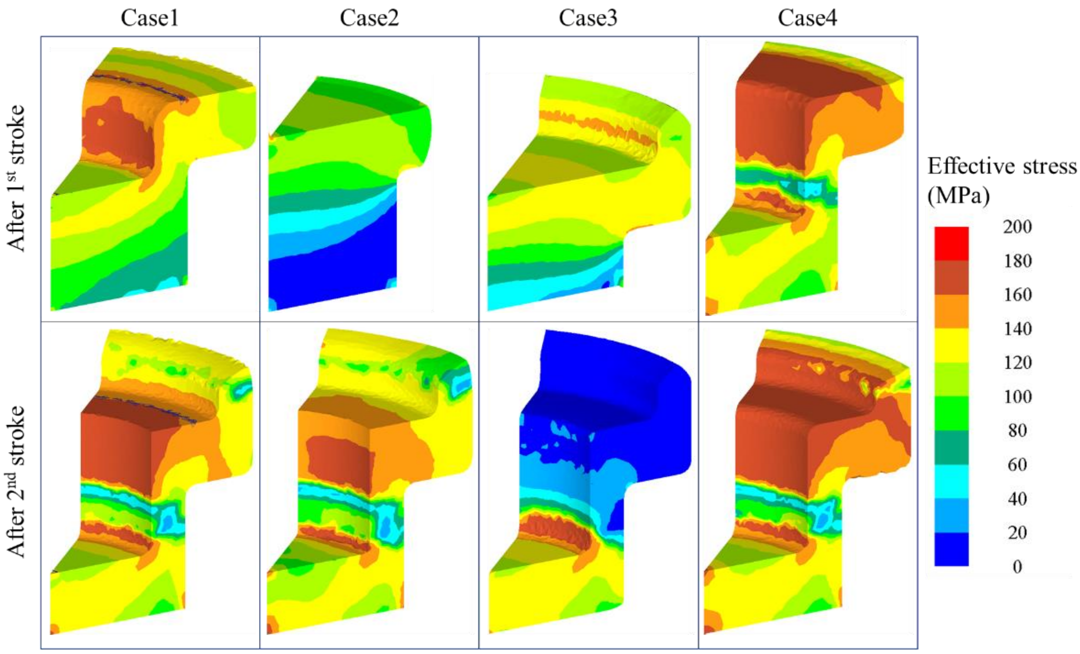

Fig. 6.18 Effective stress distribution after each stroke in the simulations of Cases 1–4.

The top surface of feature A is a freeform surface that has no constraint from the punch or die. The shape of the freeform surface is formed based on the interactive effect between internal deformation and friction, and it is therefore important to decide the subsequent process. The shapes and dimensions of feature A are shown in **Fig. 6.19**, where H1 represents the height of feature A, and H2 represents the height of the flat feature. As shown in **Fig. 6.19** (b), Case 3 had the highest H1 and H2, which represents the maximum allowance for subsequent processes. Since the material in this case flowed to form feature A first, there was less deformation accumulation so the material could flow upward more. The comparison of the strain distribution shown in **Fig. 6.16** (c) reveals that the accumulated strain on feature A of Case 3 is less than in the other cases. Moreover, the other cases similar H2 values, and Case 4 had the lowest H1. Overall, Case 3 had the best performance in the freeform geometries.

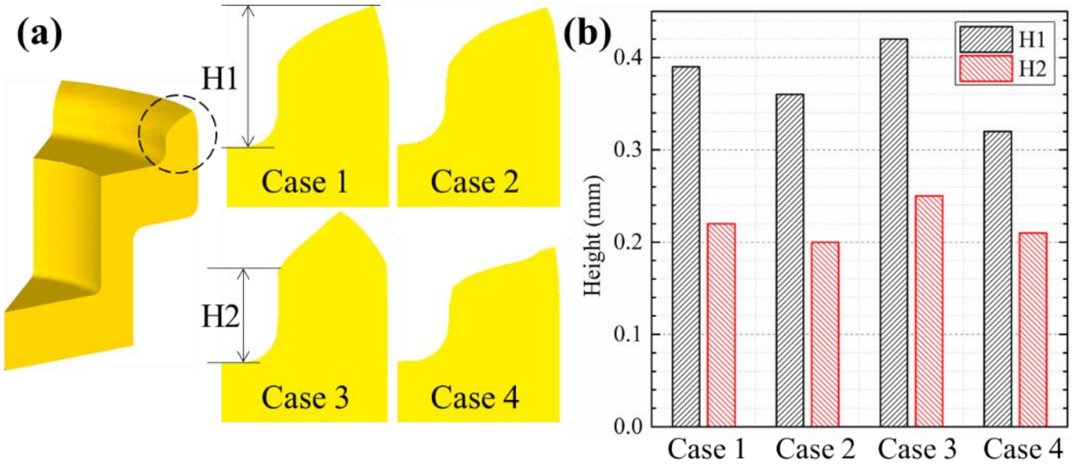

Fig. 6.19 (a) Geometries of feature A for the different cases. (b) Heights of feature A.

Based on the simulation results, the advantages and disadvantages of the proposed design cases are summarized in **Table 6.3**. Case 1 has the limitation of head length for folding avoidance. Case 3 requires complicated forming fixations. Case 4 needs complicated die structures. Thus, the conventional one-stroke flange forming is changed to the upsetting-extrusion forming of Case 2 for experiments, which has moderate forming load and energy consumption.

Table 6.3 Advantages and disadvantages of different designs.

Improved designs	Advantages	Disadvantages
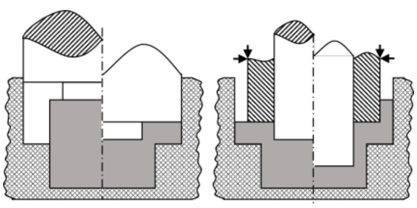 Case 1: Shortened-head design	• Simple punch and die; • Moderate forming load and energy	• Limit in folding avoidance; • Accurate volume-constant calculation; • Punch fixation

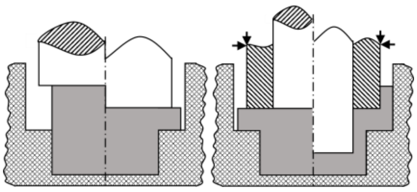 Case 2: Flat-punch design	• Simple punch and die; • Moderate forming load and energy	• Accurate volume-constant calculation; • Punch fixation
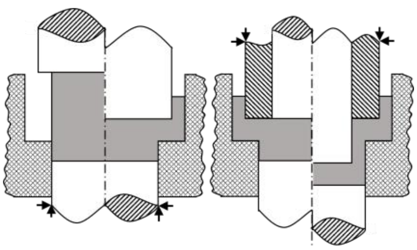 Case 3: Movable-die design	• Lower forming load; • Consume less energy; • Longer freeform	• Lower production efficiency; • Forming machine requirement; • Complicated forming fixation
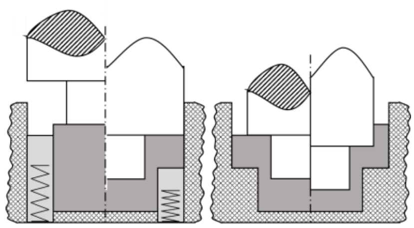 Case 4: Sliding-insert design	• Need not fix any die during forming	• Complicated die; • Higher forming load; • Consume more energy; • Shorter freeform

6.5.3 Morphologies of the experimentally formed parts

To validate the reliability of the simulation results, the experimental tests of the conventional one-stroke forming and the two-step forming of Case 2 were conducted, and the morphologies of final parts were observed using an SEM and a micro-lens, as shown in **Figs. 6.18–6.20**. These figures show that the design of Case 2 can feasibly avoid folding defects, which is consistent with the simulation results. Moreover, for the micro- and meso-scaled parts, the folding defects show irregularity around different locations, where some regions exhibit large defects, some exhibit small defects, and some show no defects. This phenomenon is caused by the increased inhomogeneous deformation of material in the micro-/meso-scaled forming processes. Regarding the macro-scaled part in **Fig. 6.22**, the folding defect was serious and occurred regularly around the cylindrical surface.

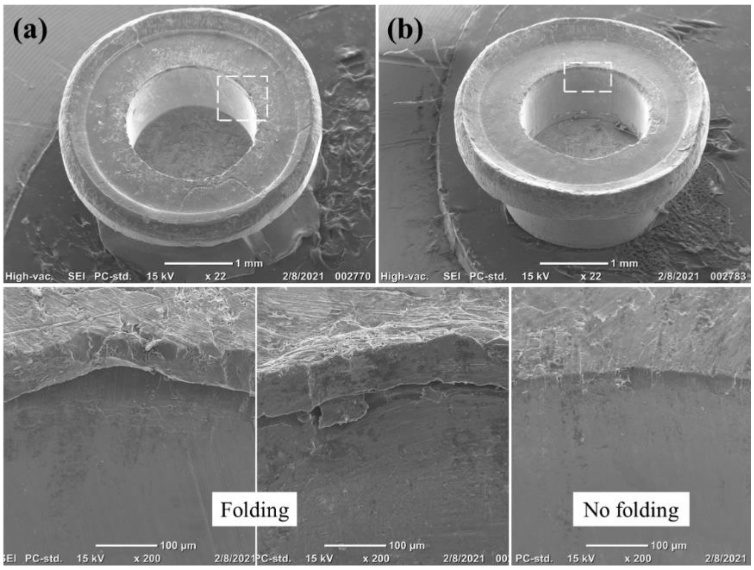

Fig. 6.20 The micro-scaled flanged parts formed by (a) one-stroke forming and (b) two-step forming in Case 2.

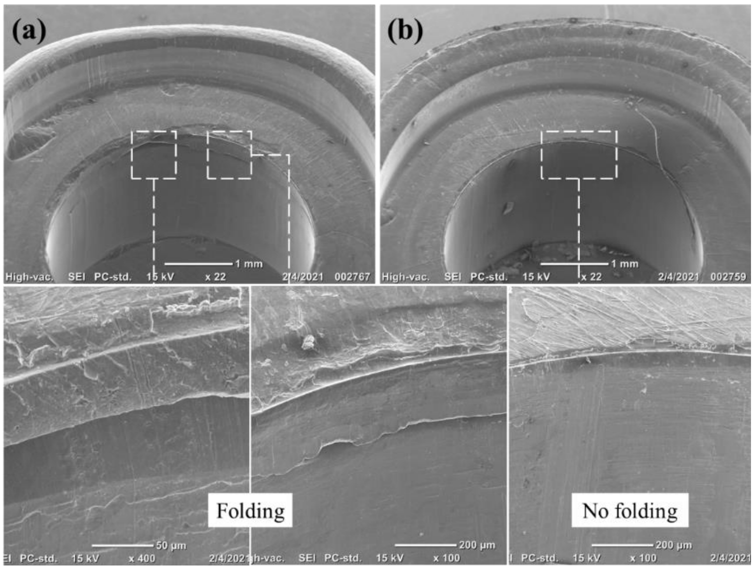

Fig. 6.21 The meso-scaled flanged parts formed by (a) one-stroke forming and (b) two-step forming in Case 2.

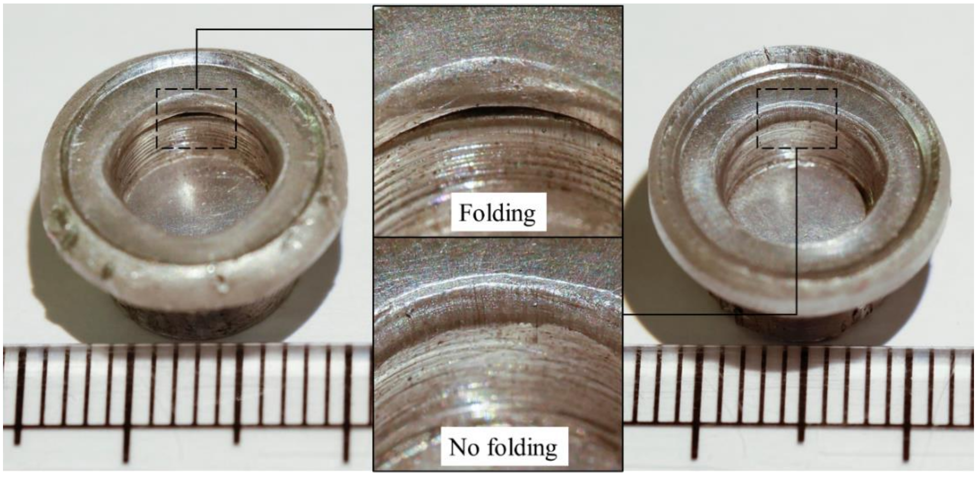

Fig. 6.22 The macro-scaled flanged parts formed by (a) one-stroke forming and (b) two-step forming in Case 2.

6.6 Summary

The flow-induced folding defect is important to address in metal forming, and its mechanism in relation to size effects is not well understood. In this research, a design-based approach was proposed to avoid folding defects, and this approach's feasibility and influence on the forming processes were comprehensively investigated. The three-scaled physical experiments were conducted to study and verify the geometrical size effect. The following conclusions can be drawn:

1) The folding defect in metal forming is the result of incoordinate material flows from multi-contact tooling. Folding-free tooling design is a way to avoid the initiation of incoordinate material flows.

2) Several design features of multi-stage flanged parts were individually considered. By changing the forming sequence of different features, the material flows were improved, and four improved designs were proposed. Cases 2 through 4 avoided the folding defects but Case 1 did not. The infeasibility of Case 1 is due to the

existence of incoordinate flows in the cavity-filling step. The formation of folding is related to the ratio of the length of the shorten pin to its full length. When the shorten pin is less than 55% of its full length, the folding defects can be avoided.

3) The forming curves of all cases were studied to analyze the material flow behaviors and their formability. Drawing-based forming with a movable die (Case 3) had the lowest forming load and consumed energy and the most desirable freeform geometries, but its stroke was longer, so its total efficiency was reduced. Therefore, forging-extrusion forming with nested punches (Case 2) was selected as the best overall design, given its consumption, geometries, and efficiency.

4) Three-scaled forming experiments were conducted for Case 2 and the original one-stroke forming, and whereafter it was found that meso-scaled forming produced the largest forming load. The forming load of the simulation was similar to that found in the experimental results. The folding-free morphology was realized from the observation of the formed parts of Case 2, which was consistent with the simulation results. Furthermore, the folding defect at the macroscale was serious and regular but this defect at the meso/microscale was irregular with variable deepness.

Chapter 7 Conclusions and future research

7.1 Conclusions

This research developed various progressive and compound forming systems for making different meso-/micro-scaled parts, and comprehensively explored the size-dependent performances of their forming processes and final parts from the perspectives of forming load, material flows, dimensional accuracy, and surface fracture through physical experiments and numerical simulations. To quantitively explore the size-dependent meso-/micro-scaled deformation behaviors in progressive and compound meso/microforming using numerical methods, a constitutive model considering grain orientations and the grain boundary-interior difference was proposed. The orientations and anisotropies of the individual grains became non-trivial issues in the prediction of the mechanical responses and deformation behaviors of the downscaled materials. Moreover, the grain boundary was generally considered to be isotropic and impeding deformation. The feasibility of this model was verified through experiments and FE simulations with the different specimens and grain sizes, and its application with respect to ductile fractures was also explored. A numerical design-based method was also employed to improve material flows using different tooling and processes to investigate the size-dependent mechanism of folding defects and how to avoid them. Four designs were proposed with different forming sequences for various features of the same flanged part, and the best of them was selected through an analysis of the material flows during each forming process and a comparison of their relative energy consumption, their feasibility in avoiding folding, and their geometrical precision in forming parts.

A progressive microforming system with blanking and extrusion operations was developed to make two types of pin-shaped plunger parts with brass sheets. The grain size effect was investigated according to deformation load, dimensional accuracy, microstructural evolution, and surface quality. This investigation revealed that the grain size effect resulted in the deviation of the punch stroke and variation in part dimensions. The formation and characteristics of shear bands and dead metal zones were related to the velocity gradient and strain accumulation. The forming defects, which include microcracks, micro pits, uneven surfaces, and longitudinal surface textures, occurred frequently on the body and tail features, and microvoids occurred in the coarse-grained material. The circular surface, however, showed the desired quality for each grain size. The dimensions for the progressively formed tail-designed pin-shaped microparts with fine-grained brass were sufficiently precise. Therefore, the tail-designed plunger micropart was ideally formed using progressive microforming with fine-grained materials.

As a case study, a compound microforming system for a blanking-heading process was developed to produce plug-shaped bulk parts by directly using copper sheets. Different punch-die clearances and grain sizes of specimens were employed to study the interactive effects of geometry and grain sizes on the microforming process and the micro-formed part. Through numerical simulations and experimental measurements of the final parts, the influences of the size effects on microstructural evolution, geometrical precision, and the surface defects of the meso-/micro-formed parts and the load-stroke relationship were comprehensively investigated. The results revealed that, when punch-die clearance equals grain size, the maximum ultimate shear stress of blanking and the highest burr are obtained. Larger grain size and punch-die clearance increase material loss and reduce the bulge diameter of the produced parts. Three shear bands and three dead metal zones were identified on the cross-section of parts, and various defects including sunken areas, pits, cracks, and surface damage were observed on the surface of the parts. Therefore, relatively finer grains and a smaller punch-die clearance can promote sheet-based bulk-part quality and avoid material loss, but the ratio of punch-die clearance to grain size should be properly selected to avoid higher ultimate shear stress and worse burr formation.

In meso-/micro-scaled deformation, the orientation and anisotropy of individual grains significantly affect the mechanical responses and deformation behaviors of polycrystalline metallic materials. Meanswhile, the grain boundary is generally considered to be a barrier to deformation. Thus, constitutive modeling considering the orientation and boundary-interior difference of grains was conducted, and the developed model was validated with SEs through experiments and simulations with different specimens and grain sizes. In compression, discontinuous shear bands were generated in a zig-zag distribution on a coarse-grained specimen, but a long and continuous shear band appeared on the fine-grained specimen, which is in accordance with experiments. By combining the GTN fracture criterion, the modeling revealed that microcracks initiate on grain boundary regions and grow along with grain boundaries. Numerous small microcracks appeared with the fine-grained material, while coarser grains facilitated the formation of larger and severe cracks in heading forming. In addition, compared with CPFEM, the GBGI model loses a little accuracy of the free surface formation in compression tests, but has advantages of efficiency in simulation.

The quality of manufactured parts and the efficiency of forming processes are crucial in deformation-based manufacturing, and size effects induce many unknowns in multi-scaled manufacturing. A simulation-based method was employed to design material flows by changing tooling and process routes in the making of a flanged part with three features. Following an analysis of the material flows, energy consumption, folding avoidance, and geometrical precision for each forming operation, a forging-extrusion forming method with nested punches was found to be most desirable. It was then implemented in the forming of parts at three scales. The experiment and simulation revealed that the macro-scaled folding defect was severe and regular, but the meso-/micro-scaled defect was irregular. These findings provide knowledge for folding-free forming of multi-stage flanged structures and other axisymmetric parts.

7.2 Suggestions for future research

7.2.1 Integrated product and process design of progressive and compound forming systems

Progressive and compound forming systems solve problems in the transporting of billets or preforms, the alignment for positioning, and the ejection of the deformed part from tooling structures. In this thesis, two progressive and compound microforming systems were established, as illustrated in Section 3.3 and Section 4.2, namely an extrusion-blanking system and a blanking-heading system. Zheng et al. [12] established a punching-extrusion-blanking system for flanged parts; Meng et al. [15] developed a punching-ironing-blanking system for flanged parts; Fu et al. [16] built a blanking-deep drawing system for metal cups. Prior research on progressive and compound microforming is focused on the forming process and the quality of parts. In contrast to laboratory measures, the production rate and costs are particularly important in mass production. The production rate and costs are closely related to the process sequence and material handling equipment. However, due to the increased surface-to-volume ratio of downscaled workpieces, the interfacial friction is increased, which induces difficulties in overcoming friction damage in ejection. Therefore, an integrated product and process design that also considers the production rate, costs, and ejection issues is necessary at the up-front design stage to reduce trial-and-error in workshops.

7.2.2 Size effects in multiphase alloys

Multi-phase alloys are composed of two or more elements, and have advantages over conventional industrial pure metal, including high flow strengths and enhanced fatigue strengths [124]. In industrial fields, multiphase alloys are widely applied. Dual-phase steels are the most widely used advanced high strength steels, whose microstructures are hard martensitic islands embedded in a soft ferrite matrix with a martensite volume fraction of 20%–30%. Complex phase steels contain bainite in addition to ferrite and martensitic, and have the potential to provide higher local ductility than dual-phase steels at the same strength level [125]. In addition, brass, as an alloy of copper and zinc, has the ability to achieve different mechanical, electrical, and chemical properties by varying volume fractions, and it can obtain multiphase microstructures at certain element proportions under a range of annealing temperatures [126-128]. For example, **Fig. 7.1** shows the dual-phase microstructures of CuZn35 under different heat treatment conditions, where the α-phase (yellow) is a face-centered cubic structure with good ductility, and the β-phase (black) is body-centered cubic structure with good strength. **Fig. 7.1** shows that the β-phase (black) is located in the grain boundary region and that annealing at low temperatures does not significantly change the microstructure. With an increase in the annealing temperature, the fraction of β-phase increases. In contrast to single-phase brass, the grain size is not significantly increased.

Prior research using multiphase alloys on various experimental studies were conducted. Gao et al. [129] investigated the effect of inclusion and microstructure on fatigue behavior of bainite/martensite multiphase steel and revealed that non-inclusion induced crack initiations for coarse microstructures. Sun et al. [130] established a computation fluid dynamic model for meso-scaled simulation of multiple material laser powder bed fusion, and the dual-phase powder beds were melting mixed. Basu et al. [131] used a multiphase high-entropy alloy comprising both fcc and bcc structured phases to investigate size-dependent plastic response using nanomechanical testing and high-resolution phase analysis, and revealed that dislocation hardening mechanisms arose. Zhang et al. [132] investigated the surface rough patterns in ultra-precision fly cutting related to size effect and phase properties of multiphase alloys.

With the development of microforming technologies, a greater number of billet materials are being considered for micropart fabrication. However, research on the size-dependent deformation behaviors of multiphase alloys is still limited, and correlated constitutive models considering size effects to describe multiphase alloys are still lacking. Based on these statements above, future research can focus on two points:

1) Future research should establish size-related isotropic or microstructure-based constitutive models to simulate and analyze micro-scaled deformation behaviors of multiphase alloys and validate these simulations through experiments.

2) Future research should also investigate the mechanical properties of some common multiphase alloys in relation to geometrical and grain size effects and phase proportions, and obtain universe mechanisms for the deformation of multiphase alloys considering size effects.

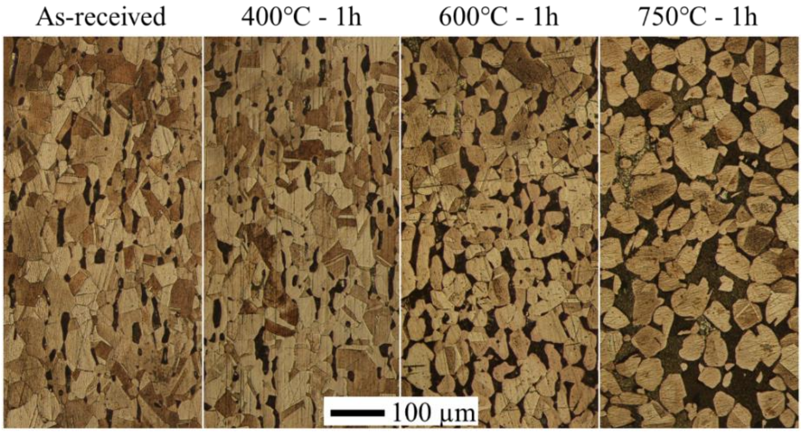

Fig. 7.1 Microstructures of CuZn35 alloy under different annealing conditions.

7.2.3 Size-related ductile fracture criteria

In micro-scaled deformation, ductile fracture behaviors are not only related to stress states but are also influenced by size effects, in contrast to macro-scaled deformation. With the development of microforming technologies, the size-related ductile fracture criteria for micro- and meso-scaled deformation must be established to improve the quality of parts and processes. The traditional ductile fracture criteria are divided into uncoupled fracture criteria, namely Freudenthal [133], C&L [134], Brozzo [135], Rice [136], Oyane [137], Ayada [138] criteria, and coupled fracture criteria, viz., GTN and continuum damage mechanics (CDM) models [139]. Furushima et al. [140] indicated that traditional uncoupled ductile fracture criteria were not applicable to predict the fracture of thin metal foil (t=0.05mm) in stretch forming with a large deviation, owing to the effect of free surface roughening that local deformation occurs on the concave region formed by surface roughening before the theoretical uniform elongation. Many studies were conducted to explore the universal mechanism in micro-scaled ductile fracture behaviors. Ran et al. [141] included the size-dependent surface layer model in the uncoupled fracture criteria to predict micro-scaled deformation and ductile fracture behaviors and succeeded in accurately predicting ductile fracture occuring in the upsetting process. Wang et al. [142] investigated the size-related deformation mechanism and ductile fracture behaviors through experimental tensile and compression tests. Shang et al. [143] extended the void growth model with the grain size effect and explained the different ductile fracture mechanisms related to grain size. Scherer and Hure [144] developed a size-dependent homogenized model for isotropic porous materials based on yield criteria considering the evolution laws of microvoids and the void shape effects. Gorji and Mohr [145] conducted in situ micro-tension and micro-shear tests with different micro-specimens to investigate the micro-scaled stress-state dependent ductile fracture. Wang et al. [81] extended GTN model with size-dependent factors and the size-effect model for fractures under a low stress triaxiality and revealed that shear-dominated fractures happen with coarse-grained material. Li et al. [146] modified the GTN-Thomason model to include shear factor and size effects and validated it under different stress states and grain sizes.

The above literature review regarding the development of micro-scaled ductile fracture criteria demonstrates that the extended coupled ductile fracture criteria were established, and experiments were conducted that mainly considered size effects and stress states in micro-scaled deformation. Future research could consider the following research directions:

1) Free surface roughening and its induced changes of stress states and deformation behaviors are important in micro-scaled fracture behaviors, as shown in **Fig. 7.2** (a). Extant models and theories have only considered the influence on whole isotropic workpieces, but localized changes of surface morphologies should be considered in theoretical and experimental investigations.

2) The evolution laws of microvoids are focused on where the microvoids located in

the grain boundary region induce ductile fractures at the microscale, as shown in **Fig. 7.2** (b). However, a comprehensive investigation considering the void shapes and grain boundary structures is still lacking. Thus, a geometrical model based on physical nature combined with microvoid evolution theories could be investigated.

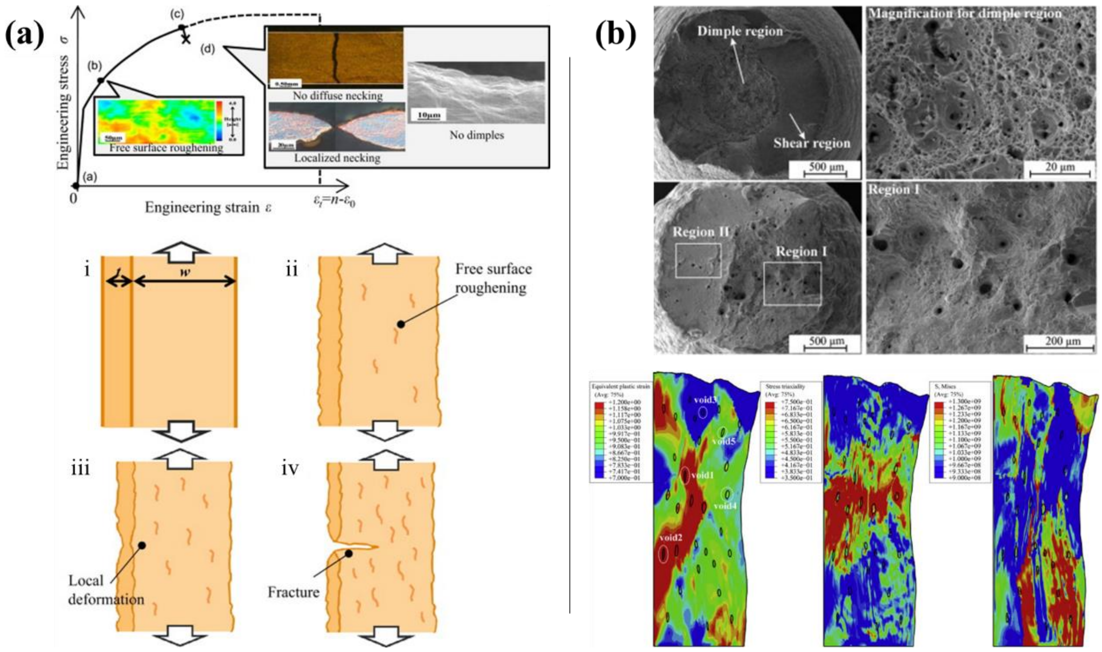

Fig. 7.2 (a) Illustration of the ductile fracture mechanism in micro metal foil affected by free surface roughening [140]. (b) Microvoids on the fracture surface of tensile bars and their evolution in a simulated tensile test [143].

References

[1] U. Engel, R. Eckstein, Microforming - from basic research to its realization, J Mater Process Tech 125 (2002) 35-44.

[2] M. Geiger, M. Kleiner, R. Eckstein, N. Tiesler, U. Engel, Microforming, Cirp Ann-Manuf Techn 50(2) (2001) 445-462.

[3] A.B.M.A. Asad, T. Masaki, M. Rahman, H.S. Lim, Y.S. Wong, Tool-based micro-machining, J Mater Process Tech 192 (2007) 204-211.

[4] T. Masuzawa, State of the art of micromachining, CIRP Ann 49(2) (2000) 473-488.

[5] A. Gillner, P. Gretzki, Chapter 5 - Laser Micro-structuring, in: Y. Qin (Ed.), Micromanufacturing Engineering and Technology (Second Edition), William Andrew Publishing, Boston, 2015, pp. 107-119.

[6] M.R.H. Knowles, G. Rutterford, D. Karnakis, A. Ferguson, Micro-machining of metals, ceramics and polymers using nanosecond lasers, Int J Adv Manuf Tech 33(1) (2007) 95-102.

[7] J. Giboz, T. Copponnex, P. Mélé, Microinjection molding of thermoplastic polymers: a review, J Micromech Microeng 17(6) (2007) R96.

[8] R. Ruprecht, T. Gietzelt, K. Müller, V. Piotter, J. Haußelt, Injection molding of microstructured components from plastics, metals and ceramics, Microsyst Technol 8(4-5) (2002) 351-358.

[9] J. Cecil, M.B. Bharathi Raj Kumar, Y. Lu, V. Basallali, A review of micro-devices assembly techniques and technology, Int J Adv Manuf Tech 83(9) (2016) 1569-1581.

[10] M.W. Fu, W.L. Chan, A review on the state-of-the-art microforming technologies, Int J Adv Manuf Tech 67(9-12) (2013) 2411-2437.

[11] M.W. Fu, J.L. Wang, A.M. Korsunsky, A review of geometrical and microstructural size effects in micro-scale deformation processing of metallic alloy

components, Int J Mach Tool Manu 109 (2016) 94-125.

[12] J.Y. Zheng, H.P. Yang, M.W. Fu, C. Ng, Study on size effect affected progressive microforming of conical flanged parts directly using sheet metals, J Mater Process Tech 272 (2019) 72-86.

[13] M.W. Fu, W.L. Chan, Micro-scaled progressive forming of bulk micropart via directly using sheet metals, Mater Design 49 (2013) 774-783.

[14] J.-Y. Zheng, S.Q. Shi, M.W. Fu, Progressive microforming of pin-shaped plunger parts and the grain size effect on its forming quality, Mater Design 187 (2020) 108386.

[15] B. Meng, M.W. Fu, S.Q. Shi, Deformation characteristic and geometrical size effect in continuous manufacturing of cylindrical and variable-thickness flanged microparts, J Mater Process Tech 252 (2018) 546-558.

[16] M.W. Fu, B. Yang, W.L. Chan, Experimental and simulation studies of micro blanking and deep drawing compound process using copper sheet, J Mater Process Tech 213(1) (2013) 101-110.

[17] W.L. Chan, M.W. Fu, J. Lu, Experimental and simulation study of deformation behavior in micro-compound extrusion process, Mater Design 32(2) (2011) 525-534.

[18] M. Hasan, J. Zhao, Z. Jiang, Micromanufacturing of composite materials: a review, Int J Extreme Manuf 1(1) (2019) 012004.

[19] W. Bauer, M. Müller, R. Knitter, P. Börsting, A. Albers, M. Deuchert, V. Schulze, Design and prototyping of a ceramic micro turbine: a case study, Microsyst Technol 16(4) (2010) 607-615.

[20] C. Pradeep Raja, T. Ramesh, Influence of size effects and its key issues during microforming and its associated processes – A review, Eng Sci Technol an Int J 24(2) (2021) 556-570.

[21] F. Vollertsen, D. Biermann, H.N. Hansen, I.S. Jawahir, K. Kuzman, Size effects in manufacturing of metallic components, Cirp Ann-Manuf Techn 58(2) (2009) 566-587.

[22] F. Vollertsen, Categories of size effects, Prod Eng 2(4) (2008) 377.

[23] W.L. Chan, M.W. Fu, B. Yang, Experimental studies of the size effect affected microscale plastic deformation in micro upsetting process, Mater Sci Eng A 534 (2012) 374-383.

[24] A. Rosochowski, W. Presz, L. Olejnik, M. Richert, Micro-extrusion of ultra-fine grained aluminium, Int J Adv Manuf Tech 33(1) (2007) 137-146.

[25] U. Engel, Tribology in microforming, Wear 260(3) (2006) 265-273.

[26] W.L. Chan, M.W. Fu, Meso-scaled progressive forming of bulk cylindrical and flanged parts using sheet metal, Mater Design 43 (2013) 249-257.

[27] E. Ghassemali, M.J. Tan, A.E.W. Jarfors, S.C.V. Lim, Progressive microforming process: towards the mass production of micro-parts using sheet metal, Int J Adv Manuf Tech 66(5-8) (2013) 611-621.

[28] B. Meng, M.W. Fu, C.M. Fu, K.S. Chen, Ductile fracture and deformation behavior in progressive microforming, Mater Design 83 (2015) 14-25.

[29] B. Meng, M.W. Fu, C.M. Fu, J.L. Wang, Multivariable analysis of micro shearing process customized for progressive forming of micro-parts, Int J Mech Sci 93 (2015) 191-203.

[30] J.Q. Ran, L. Xu, J.L. Wang, T. Xu, F. Gong, Influence of dead metal zone on dislocation strengthening effect during micro-progressive forming, Int J Adv Manuf Tech 105(1-4) (2019) 1129-1141.

[31] X.F. Tang, S.Q. Shi, M.W. Fu, Interactive effect of grain size and crystal structure on deformation behavior in progressive micro-scaled deformation of metallic materials, Int J Mach Tool Manu 148 (2020).

[32] K. Hirota, Fabrication of micro-billet by sheet extrusion, J Mater Process Tech 191(1-3) (2007) 283-287.

[33] P. Ludwik, Elemente der technologischen Mechanik, Springer1909.

[34] H.W. Swift, Plastic instability under plane stress, J Mech Phys Solids 1(1) (1952) 1-18.

[35] E. Voce, The Relationship between Stress and Strain for Homogeneous Deformation, J Inst Met 74 (1948) 537-562.

[36] W. Ramberg, W.R. Osgood, Description of stress-strain curves by three parameters, (1943).

[37] N. Hansen, Hall–Petch relation and boundary strengthening, Scripta Mater. 51(8) (2004) 801-806.

[38] G.I. Taylor, The mechanism of plastic deformation of crystals. Part I.—Theoretical, Proceedings of the Royal Society of London. Series A, Containing Papers of a Mathematical and Physical Character 145(855) (1934) 362-387.

[39] R.W. Armstrong, Engineering science aspects of the Hall–Petch relation, Acta Mech 225(4-5) (2014) 1013-1028.

[40] X. Lai, L. Peng, P. Hu, S. Lan, J. Ni, Material behavior modelling in micro/meso-scale forming process with considering size/scale effects, Comput Mater Sci 43(4) (2008) 1003-1009.

[41] M.A. Meyersm, E. Ashworth, A model for the effect of grain size on the yield stress of metals, Philosophical Magazine A 46(5) (1982) 737-759.

[42] R.J. Asaro, Crystal Plasticity, J Appl Mech 50(4b) (1983) 921-934.

[43] F. Roters, P. Eisenlohr, L. Hantcherli, D.D. Tjahjanto, T.R. Bieler, D. Raabe, Overview of constitutive laws, kinematics, homogenization and multiscale methods in crystal plasticity finite-element modeling: Theory, experiments, applications, Acta Mater 58(4) (2010) 1152-1211.

[44] M. Arentoft, T. Wanheim, The basis for a design support system to prevent defects in forging, J Mater Process Tech 69(1) (1997) 227-232.

[45] Y. Qin, Overview of Micro-manufacturing, in: Y. Qin (Ed.), Micromanufacturing Engineering and Technology, William Andrew Publishing, Boston, 2010, pp. 1-33.

[46] Y.e. Cheng, B. Shew, C. Lin, D. Wei, M. Chyu, Ultra-deep LIGA process, J Micromech Microeng 9(1) (1999) 58.

[47] M.W. Fu, J.L. Wang, Size effects in multi-scale materials processing and manufacturing, Int J Mach Tool Manu 167 (2021) 103755.

[48] B. Boswell, M.N. Islam, I.J. Davies, A review of micro-mechanical cutting, Int J Adv Manuf Tech 94(1) (2018) 789-806.

[49] R.C. Panda, A. Sharada, L.D. Samanta, A review on electrical discharge machining and its characterization, Mater Today Proc (2021).

[50] N. Faisal, D. Zindani, K. Kumar, S. Bhowmik, Laser Micromachining of Engineering Materials—A Review, in: K. Kumar, D. Zindani, N. Kumari, J.P. Davim (Eds.), Micro and Nano Machining of Engineering Materials: Recent Developments, Springer International Publishing, Cham, 2019, pp. 121-136.

[51] H.-E. Joe, E.-G. Kang, B. Martin, A Review of State of the Art of Electron Beam and Ion Beam Machining, J Korean Soc Precis Eng 35(3) (2018) 241-252.

[52] S. Sitaram Wangikar, P. Kumar Patowari, R. Dev Misra, Parametric Optimization for Photochemical Machining of Copper using Overall Evaluation Criteria, Mater Today Proc 5(2, Part 1) (2018) 4736-4742.

[53] S.Y. Liang, Mechanical machining and metrology at micro/nano scale, Third International Symposium on Precision Mechanical Measurements, International Society for Optics and Photonics, 2006, p. 628002.

[54] T.D. Ngo, A. Kashani, G. Imbalzano, K.T.Q. Nguyen, D. Hui, Additive manufacturing (3D printing): A review of materials, methods, applications and challenges, Compos B Eng 143 (2018) 172-196.

[55] M. Vaezi, H. Seitz, S. Yang, A review on 3D micro-additive manufacturing technologies, Int J Adv Manuf Tech 67(5) (2013) 1721-1754.

[56] J. Xu, X. Wang, C. Wang, L. Yuan, W. Chen, J. Bao, Q. Su, Z. Xu, C. Wang, Z. Wang, D. Shan, B. Guo, A Review on Micro/Nanoforming to Fabricate 3D Metallic Structures, Adv Mater 33(6) (2021) 2000893.

[57] J. Cao, E. Brinksmeier, M. Fu, R.X. Gao, B. Liang, M. Merklein, M. Schmidt, J. Yanagimoto, Manufacturing of advanced smart tooling for metal forming, CIRP Ann 68(2) (2019) 605-628.

[58] M.W. Fu, W.L. Chan, Micro-scaled products development via microforming, Springer, London, 2014.

[59] J.R. Greer, J.T.M. De Hosson, Plasticity in small-sized metallic systems: Intrinsic versus extrinsic size effect, Prog. Mater Sci. 56(6) (2011) 654-724.

[60] M.D. Uchic, P.A. Shade, D.M. Dimiduk, Plasticity of Micrometer-Scale Single Crystals in Compression, Annu Rev Mater Sci 39(1) (2009) 361-386.

[61] S. Mahabunphachai, M. Koç, Investigation of size effects on material behavior of thin sheet metals using hydraulic bulge testing at micro/meso-scales, Int J Mach Tool Manu 48(9) (2008) 1014-1029.

[62] W.L. Chan, M.W. Fu, J. Lu, The size effect on micro deformation behaviour in micro-scale plastic deformation, Mater Design 32(1) (2011) 198-206.

[63] O. Pawelski, Ways and limits of the theory of similarity in application to problems of physics and metal forming, J Mater Process Tech 34(1) (1992) 19-30.

[64] L. Peng, X. Lai, H.-J. Lee, J.-H. Song, J. Ni, Friction behavior modeling and analysis in micro/meso scale metal forming process, Mater Design 31(4) (2010) 1953-1961.

[65] J.H. Deng, M.W. Fu, W.L. Chan, Size effect on material surface deformation behavior in micro-forming process, Mat Sci Eng a-Struct 528(13-14) (2011) 4799-4806.

[66] T. Shimizu, M. Yang, K.-i. Manabe, Classification of mesoscopic tribological properties under dry sliding friction for microforming operation, Wear 330-331 (2015) 49-58.

[67] D.-K. Leu, Modeling of surface roughness effect on dry contact friction in metal forming, Int J Adv Manuf Tech 57(5-8) (2011) 575.

[68] J. Han, W. Zheng, G. Wang, M. Yu, Experimental study on size effect of dry friction in meso/micro-upsetting process, Int J Adv Manuf Tech 95(1) (2018) 1127-1133.

[69] W.T. Li, H. Li, M.W. Fu, Interactive effect of stress state and grain size on

fracture behaviours of copper in micro-scaled plastic deformation, Int J Plasticity 114 (2019) 126-143.

[70] W.T. Li, M.W. Fu, S.Q. Shi, Study of deformation and ductile fracture behaviors in micro-scale deformation using a combined surface layer and grain boundary strengthening model, Int J Mech Sci 131-132 (2017) 924-937.

[71] T. Nakamura, N. Bay, Z.-L. Zhang, FEM Simulation of Friction Testing Method Based on Combined Forward Rod-Backward Can Extrusion, J Tribol 119(3) (1997) 501-506.

[72] W.L. Chan, M.W. Fu, Experimental studies of plastic deformation behaviors in microheading process, J Mater Process Tech 212(7) (2012) 1501-1512.

[73] P.F. Gao, M.Y. Fei, X.G. Yan, S.B. Wang, Y.K. Li, L. Xing, K. Wei, M. Zhan, Z.T. Zhou, Z. Keyim, Prediction of the folding defect in die forging: A versatile approach for three typical types of folding defects, J Manuf Process 39 (2019) 181-191.

[74] E. Hall, The deformation and ageing of mild steel: III discussion of results, Proc Phys Soc London, Sect B 64(9) (1951) 747.

[75] N. Petch, The cleavage strength of polycrystals, J Iron Steel Res Int 174 (1953) 25-28.

[76] L. Peng, F. Liu, J. Ni, X. Lai, Size effects in thin sheet metal forming and its elastic–plastic constitutive model, Mater Design 28(5) (2007) 1731-1736.

[77] W.L. Chan, M.W. Fu, Experimental studies and numerical modeling of the specimen and grain size effects on the flow stress of sheet metal in microforming, Mater Sci Eng A 528(25) (2011) 7674-7683.

[78] H.H. Fu, D.J. Benson, M.A. Meyers, Analytical and computational description of effect of grain size on yield stress of metals, Acta Mater 49(13) (2001) 2567-2582.

[79] J. Zhou, Z. Li, R. Zhu, Y. Li, Z. Zhang, A mixtures-based model for the grain size dependent mechanical behavior of nanocrystalline materials, J Mater Process Tech 197(1) (2008) 325-336.

[80] F. Roters, P. Eisenlohr, T.R. Bieler, D. Raabe, Crystal plasticity finite element methods: in materials science and engineering, John Wiley & Sons2011.

[81] J. Wang, C. Li, Y. Wan, C. Zhang, J. Ran, M.W. Fu, Size effect on the shear damage under low stress triaxiality in micro-scaled plastic deformation of metallic materials, Mater Design 196 (2020) 109107.

[82] Z.T. Xu, L.F. Peng, M.W. Fu, X.M. Lai, Size effect affected formability of sheet metals in micro/meso scale plastic deformation: Experiment and modeling, Int J Plasticity 68 (2015) 34-54.

[83] R. Armstrong, I. Codd, R. Douthwaite, N. Petch, The plastic deformation of polycrystalline aggregates, Philos Mag 7(73) (1962) 45-58.

[84] S. Miyazaki, K. Shibata, H. Fujita, Effect of specimen thickness on mechanical properties of polycrystalline aggregates with various grain sizes, Acta Metallurgica 27(5) (1979) 855-862.

[85] W.L. Chan, M.W. Fu, Experimental studies and numerical modeling of the specimen and grain size effects on the flow stress of sheet metal in microforming, Mat Sci Eng a-Struct 528(25-26) (2011) 7674-7683.

[86] H.-H. Fu, D.J. Benson, M.A. Meyers, Analytical and computational description of effect of grain size on yield stress of metals, Acta Mater 49(13) (2001) 2567-2582.

[87] E. Schmid, W. Boas, Plasticity of Crystals, FA Hughes & Co, Ltd., London (1950) 55.

[88] F.R.N. Nabarro, Extended dislocations and the schmid law of resolved shear stress, Philos Mag 14(130) (1966) 861-866.

[89] J. Pan, J.R. Rice, Rate sensitivity of plastic flow and implications for yield-surface vertices, Int J Solids Struct 19(11) (1983) 973-987.

[90] S.R. Kalidindi, C.A. Bronkhorst, L. Anand, Crystallographic texture evolution in bulk deformation processing of FCC metals, J Mech Phys Solids 40(3) (1992) 537-569.

[91] A.L. Gurson, Continuum Theory of Ductile Rupture by Void Nucleation and

Growth: Part I—Yield Criteria and Flow Rules for Porous Ductile Media, J. Eng. Mater. Technol. 99(1) (1977) 2-15.

[92] V. Tvergaard, A. Needleman, Analysis of the cup-cone fracture in a round tensile bar, Acta Metall 32(1) (1984) 157-169.

[93] A.R. Razali, Y. Qin, A Review on Micro-manufacturing, Micro-forming and their Key Issues, Procedia Manuf 53 (2013) 665-672.

[94] B. Boswell, M.N. Islam, I.J. Davies, A review of micro-mechanical cutting, Int J Adv Manuf Tech 94(1-4) (2017) 789-806.

[95] L. Peng, X. Lai, H.-J. Lee, J.-H. Song, J. Ni, Analysis of micro/mesoscale sheet forming process with uniform size dependent material constitutive model, Mater Sci Eng A 526(1-2) (2009) 93-99.

[96] A.N.G. Kong, B.-K. Gong, G. Wang, H.-W. Cui, Influence of Surface Roughness of substrate on the Properties of Ni–Co–Fe electrodeposition coating on copper, Surf. Rev. Lett. 25(08) (2018).

[97] W.L. Chan, M.W. Fu, B. Yang, Study of size effect in micro-extrusion process of pure copper, Mater Design 32(7) (2011) 3772-3782.

[98] T.G. Murthy, C. Saldana, M. Hudspeth, R. M'Saoubi, Deformation field heterogeneity in punch indentation, Proc Math Phys Eng Sci 470(2166) (2014) 20130807.

[99] S.Z. Qamar, Shape Complexity, Metal Flow, and Dead Metal Zone in Cold Extrusion, Mater. Manuf. Processes 25(12) (2010) 1454-1461.

[100] N.K. Sundaram, Deformation field in deep flat punch indentation and the persistence of dead-metal zones, Philos Mag 98(25) (2018) 2326-2344.

[101] W. Zhou, J. Lin, T.A. Dean, L. Wang, Analysis and modelling of a novel process for extruding curved metal alloy profiles, Int J Mech Sci 138-139 (2018) 524-536.

[102] E. Ghassemali, A.E.W. Jarfors, M.J. Tan, S.C.V. Lim, On the microstructure of micro-pins manufactured by a novel progressive microforming process, Int J Mater Form 6(1) (2013) 65-74.

[103] E. Uhlmann, M. Röhner, M. Langmack, T.-M. Schimmelpfennig, Chapter 4 - Micro-electrical Discharge Machining, in: Y. Qin (Ed.), Micromanufacturing Engineering and Technology (Second Edition), William Andrew Publishing, Boston, 2015, pp. 81-105.

[104] A. Pimpin, W. Srituravanich, Review on micro-and nanolithography techniques and their applications, Eng J 16(1) (2012) 37-56.

[105] R. Armstrong, I. Codd, R.M. Douthwaite, N.J. Petch, The plastic deformation of polycrystalline aggregates, Philos Mag 7(73) (1962) 45-58.

[106] M. Kardan-Halvaei, M. Morovvati, B. Mollaei-Dariani, Crystal plasticity finite element simulation and experimental investigation of the micro-upsetting process of OFHC copper, J Micromech Microeng 30(7) (2020) 075005.

[107] Y. Huang, A user-material subroutine incorporating single crystal plasticity in the ABAQUS finite element program, Harvard Univ. Cambridge1991.

[108] J. Kysar, Addendum to a user-material subroutine incorporating single crystal plasticity in the ABAQUS finite element program, Mech report 178 (1997).

[109] R. Quey, P.R. Dawson, F. Barbe, Large-scale 3D random polycrystals for the finite element method: Generation, meshing and remeshing, Comput Methods Appl Mech Eng 200(17) (2011) 1729-1745.

[110] J. Xu, B. Guo, C. Wang, D. Shan, Blanking clearance and grain size effects on micro deformation behavior and fracture in micro-blanking of brass foil, Int J Mach Tool Manu 60 (2012) 27-34.

[111] S.K. Maiti, A.A. Ambekar, U.P. Singh, P.P. Date, K. Narasimhan, Assessment of influence of some process parameters on sheet metal blanking, J Mater Process Tech 102(1) (2000) 249-256.

[112] E. Taupin, J. Breitling, W.-t. Wu, T. Altan, Material fracture and burr formation in blanking results of FEM simulations and comparison with experiments, J Mater Process Tech 59(1) (1996) 68-78.

[113] J.-Y. Zheng, M.-W. Fu, Progressive and Compound Forming for Producing Plunger-Typed Microparts by Using Sheet Metal, J Micro Nanomanuf 8(2) (2020).

[114] B. Clausen, T. Lorentzen, T. Leffers, Self-consistent modelling of the plastic deformation of f.c.c. polycrystals and its implications for diffraction measurements of internal stresses, Acta Mater 46(9) (1998) 3087-3098.

[115] W.T. Li, H. Li, M.W. Fu, Interactive effect of stress state and grain size on fracture behaviours of copper in micro-scaled plastic deformation, Int J Plasticity (2018).

[116] J.G. Liu, M.W. Fu, W.L. Chan, A constitutive model for modeling of the deformation behavior in microforming with a consideration of grain boundary strengthening, Comput Mater Sci 55 (2012) 85-94.

[117] H. Gleiter, Nanostructured materials: basic concepts and microstructure, Acta Mater 48(1) (2000) 1-29.

[118] H. Van Swygenhoven, M. Spaczer, A. Caro, Microscopic description of plasticity in computer generated metallic nanophase samples: a comparison between Cu and Ni, Acta Mater 47(10) (1999) 3117-3126.

[119] G. Sachs, Plasticity problems in metals, Transactions of the Faraday Society 24 (1928) 84-92.

[120] L. Tabourot, M. Fivel, E. Rauch, Generalised constitutive laws for f.c.c. single crystals, Mater Sci Eng A 234-236 (1997) 639-642.

[121] S.C. Shrivastava, J.J. Jonas, G. Canova, Equivalent strain in large deformation torsion testing : Theoretical and practical considerations, J Mech Phys Solids 30(1) (1982) 75-90.

[122] T. Pardoen, I. Doghri, F. Delannay, Experimental and numerical comparison of void growth models and void coalescence criteria for the prediction of ductile fracture in copper bars, Acta Mater 46(2) (1998) 541-552.

[123] M. Merklein, J.M. Allwood, B.A. Behrens, A. Brosius, H. Hagenah, K. Kuzman, K. Mori, A.E. Tekkaya, A. Weckenmann, Bulk forming of sheet metal, CIRP Ann 61(2) (2012) 725-745.

[124] Y. Cui, N. Li, A. Misra, An overview of interface-dominated deformation mechanisms in metallic nanocomposites elucidated using in situ straining in a TEM, J

Mater Res 34(9) (2019) 1469-1478.

[125] B. Erice, C.C. Roth, D. Mohr, Stress-state and strain-rate dependent ductile fracture of dual and complex phase steel, Mech Mater 116 (2018) 11-32.

[126] E. Farabi, A. Zarei-Hanzaki, H.R. Abedi, High Temperature Formability Prediction of Dual Phase Brass Using Phenomenological and Physical Constitutive Models, J. Mater. Eng. Perform. 24(1) (2015) 209-220.

[127] S.E. Mousavi, M. Meratian, A. Rezaeian, Investigation of mechanical properties and fracture surfaces of dual-phase 60–40 brass alloy processed by warm equal-channel angular pressing, J Mater Sci 52(13) (2017) 8041-8051.

[128] R. Ramesh, I. Dinaharan, E.T. Akinlabi, N. Murugan, Microstructure and Mechanical Characterization of Friction-Stir-Welded Dual-Phase Brass, J. Mater. Eng. Perform. 27(4) (2018) 1544-1554.

[129] G. Gao, Q. Xu, H. Guo, X. Gui, B. Zhang, B. Bai, Effect of inclusion and microstructure on the very high cycle fatigue behaviors of high strength bainite/martensite multiphase steels, Mater Sci Eng A 739 (2019) 404-414.

[130] Z. Sun, Y.-H. Chueh, L. Li, Multiphase mesoscopic simulation of multiple and functionally gradient materials laser powder bed fusion additive manufacturing processes, Addit Manuf 35 (2020) 101448.

[131] I. Basu, V. Ocelík, J.T.M. De Hosson, Size dependent plasticity and damage response in multiphase body centered cubic high entropy alloys, Acta Mater 150 (2018) 104-116.

[132] G. Zhang, J. Ran, S. To, X. Wu, P. Huang, M.P. Kuz'min, Size effect on surface generation of multiphase alloys in ultra-precision fly cutting, J Manuf Process 60 (2020) 23-36.

[133] A.M. Freudenthal, The inelastic behavior of engineering materials and structures, Wiley1950.

[134] M.G. Cockcroft, Ductility and workability of metals, J. of Metals. 96 (1968) 2444.

[135] P. Brozzo, B. Deluca, R. Rendina, A new method for the prediction of formability limits in metal sheets, Proc. 7th biennal Conf. IDDR, 1972.

[136] J.R. Rice, D.M. Tracey, On the ductile enlargement of voids in triaxial stress fields*, J Mech Phys Solids 17(3) (1969) 201-217.

[137] M. Oyane, T. Sato, K. Okimoto, S. Shima, Criteria for ductile fracture and their applications, J Mech Work Technol 4(1) (1980) 65-81.

[138] M. Ayada, Central bursting in extrusion of inhomogeneous materials, Proceedings of 2nd International Conference on Technology for Plasticity, Stuttgart, 1987 1 (1987) 553-558.

[139] H. Li, M.W. Fu, J. Lu, H. Yang, Ductile fracture: Experiments and computations, Int J Plasticity 27(2) (2011) 147-180.

[140] T. Furushima, H. Tsunezaki, K.-i. Manabe, S. Alexsandrov, Ductile fracture and free surface roughening behaviors of pure copper foils for micro/meso-scale forming, Int J Mach Tool Manu 76 (2014) 34-48.

[141] J.Q. Ran, M.W. Fu, W.L. Chan, The influence of size effect on the ductile fracture in micro-scaled plastic deformation, Int J Plasticity 41 (2013) 65-81.

[142] J.L. Wang, M.W. Fu, S.Q. Shi, Influences of size effect and stress condition on ductile fracture behavior in micro-scaled plastic deformation, Mater Design 131 (2017) 69-80.

[143] X. Shang, H. Zhang, Z. Cui, M.W. Fu, J. Shao, A multiscale investigation into the effect of grain size on void evolution and ductile fracture: Experiments and crystal plasticity modeling, Int J Plasticity 125 (2020) 133-149.

[144] J.M. Scherer, J. Hure, A size-dependent ductile fracture model: Constitutive equations, numerical implementation and validation, Eur J Mech A Solids 76 (2019) 135-145.

[145] M.B. Gorji, D. Mohr, Micro-tension and micro-shear experiments to characterize stress-state dependent ductile fracture, Acta Mater 131 (2017) 65-76.

[146] W.T. Li, Z.Y. Cai, H. Li, L.F. Peng, X.M. Lai, M.W. Fu, The modified GTN-

Thomason criterion for modelling of ductile fracture considering shear factor and size effect in micro-scaled plastic deformation, Int J Mech Sci 204 (2021) 106540.